2022

Analysing the Structural Dynamics of Retinoid X Receptor Using Hydrogen Deuterium Exchange Mass Spectrometry

Nathalia Melo
University Of Alabama At Birmingham

ANALYZING THE STRUCTURAL DYNAMICS OF RETINOID X RECEPTOR USING HYDROGEN DEUTERIUM EXCHANGE MASS SPECTROMETRY

by

NATHALIA MELO

NATALIA KEDISHVILI, COMMITTEE CHAIR
SUZANNE LAPI
CHAD PETIT
PETER PREVELIGE
MATTHEW RENFROW

A DISSERTATION

Submitted to the graduate faculty of The University of Alabama at Birmingham,
in partial fulfillment of the requirements for the degree of
Doctor of Philosophy

BIRMINGHAM, ALABAMA

2022

ANALYZING THE STRUCTURAL DYNAMICS OF RETINOID X RECEPTOR USING HYDROGEN DEUTERIUM EXCHANGE MASS SPECTROMETRY

NATHALIA MELO

BIOCHEMISTRY AND STRUCTURAL BIOLOGY

ABSTRACT

Nuclear receptors (NR) are ligand-activated transcription factors that are targets for drug discovery due to their ability to directly modulate gene expression. There are 48 NRs and approximately half of them require heterodimerization with retinoid X receptor (RXR) to function. Targretin (bexarotene) is an FDA-approved RXR specific (rexinoid) currently used to treat Cutaneous T-cell Lymphoma (CTCL); however, it causes hyperlipidemia toxicities. A functionally similar rexinoid developed at UAB, 9-*cis*-UAB30 (UAB30), is non-toxic and weak agonist in the liver. While UAB30 shows promise as a low toxicity chemopreventative drug, the mechanism of UAB30 action at the molecular level is poorly understood. By modifying UAB30, we have been able to understand how structurally similar rexinoids dynamically alter RXR in different regions. The standard NR-targeted drug design involves the characterization of ligand- ligand-binding domain (LBD) structural interactions through X-ray crystallography. While crucial in the design process, crystallographic structures are static snapshots of ligand-bound proteins that exist in solution, having dynamic molecular motions. In this dissertation, I used hydrogen deuterium exchange mass spectrometry to analyze rexinoid and coactivator binding-associated structural dynamics. I investigated the response of binding of several rexinoids in complex with RXRα-LBD, which gave insight into two rexinoid responses of binding. The first response involved decreased deuterium

uptake (decreased dynamics) of helices 3 and 5. Decreased dynamics of these regions correlated with both potency and binding affinity of the rexinoid to RXRα-LBD. The second response was an increase in deuterium uptake (increase dynamics) of the C-terminal end of helix 3, helices 8 and 9, and the loop between helix 8 and 9. Part of the RXR homodimer interface displayed increased dynamics. We further investigated RXRα-LBD by incorporating a coactivator peptide. The ternary complexes of RXRα-LBD-rexinoid-coactivator displayed decreased dynamics in the ligand-binding pocket and coactivator binding sites. The accumulated profiles of various RXR complexes helped in understanding RXR's mechanism of action.

Keywords: Nuclear receptor, retinoid X receptor, rexinoid agonists, UAB30, hydrogen deuterium exchange mass spectrometry

DEDICATION

I would like to thank my parents, Liliana and Carlos for their continued love and support. I would also like to thank Mango who showed me that a dog can really be one's best friend.

ACKNOWLEDGMENTS

I would like to thank my thesis mentor, Dr. Matthew Renfrow for his guidance and dedication. I am also grateful to Dr. Peter Prevelige for his invaluable insights and patience when teaching me mass spectrometry.

TABLE OF CONTENTS

Page

LIST OF FIGURES

Figures *Page*

INTRODUCTION

CONNECTING LIGAND-INDUCED RETINOID X RECEPTOR STRUCTURAL DYNAMICS TO REXINOID AGONIST POTENCY

ANALYZING THE STRUCTURAL DYNAMICS OF RETINOID X RECEPTOR BOUND TO UAB30 METHYLATED DERIVATIVES

STABILITY OF THE RETINOID X RECEPTOR-α HOMODIMER IN THE PRESCENCE AND ABSENCE OF REXINOID AND COACTIVATOR PEPTIDE

DISCUSSION

LIST OF TABLES

Table *Page*

INTRODUCTION

CONNECTING LIGAND-INDUCED RETINOID X RECEPTOR STRUCTURAL DYNAMICS TO REXINOID AGONIST POTENCY

ANALYZING THE STRUCTURAL DYNAMICS OF RETINOID X RECEPTOR BOUND TO UAB30 METHYLATED DERIVATIVES

STABILITY OF RETINOID X RECEPTOR-A HOMODIMER IN THE PRESENCE AND ABSENCE OF REXINOID AND COACTIVATOR PEPTIDE

CHAPTER 1: INTRODUCTION TO NUCLEAR RECEPTOR STRUCTURE AND FUNCTION

Characterization of Nuclear Receptors

Nuclear Receptors (NR) are ligand-activated transcription factors that are key targets for drug discovery and development due to their ability to directly modulate gene expression. There are three classes of NRs, class I (steroid receptors), class II (RXR heterodimers), class III (orphan receptors) [1]. Class I NR are found anchored in the cytoplasm by chaperone proteins such as HSP90 [2]. Ligand binding to the receptor allows for entry into the nucleus by the exposure of the nuclear localization sequence, leading to entry into the nucleus. Ligands for class I NRs are derived from cholesterol. Upon entering the cell nucleus, the steroid receptor can homodimerize and bind to the hormone response element on the promoter of the target gene.

Class I NRs include androgen receptor, progesterone receptor, mineralocorticoid receptor, glucocorticoid receptor, and estrogen receptor. The androgen receptor (AR) is responsible for bone growth, male sexual differentiation, and muscle homeostasis [3]. α-dihydrotestosterone (DHT) can bind to the ligand-binding pocket (LBP) of AR and activate it by releasing the receptor from HSP70 and HSP90 [4]. Progesterone receptor (PR) is essential for the development of female mammary glands and female reproductive organs [5]. PR has two isoforms: progesterone receptor-A and progesterone receptor B. The ligand that activates PR is progesterone. Glucocorticoids are the ligands that bind to the glucocorticoid receptor (GR) and allow for the maintenance of basal and stress-related homeostasis [6]. The estrogen receptors play a role in female

reproduction and breast cancer [7]. There are two isoforms ERα and Erβ which are activated by estradiol. The two isoforms differ in the AF-1 and AF-2 regions. Erα has both structural regions and is more transcriptionally active. ERβ only has an AF-2 region indicating the importance of a coactivator binding site [8].

Class II NRs are receptors that heterodimerize with retinoid X receptor (RXR). RXR's role as a heterodimer partner was discovered through the addition of an unidentified protein in HeLa cell nuclear extracts which enhanced thyroid receptor (TR) and retinoic acid receptor (RAR) DNA binding affinity [9]. This unknown protein was then identified as RXRβ [10, 11]. Three types of heterodimerization can occur: permissive, non-permissive, and conditional permissive (Figure 1). Non-permissive NRs include thyroid receptor (TR) and vitamin D receptor (VDR) [12, 13]. These are activated only by ligands specific to the partner not by ligand binding to RXR [14]. Liver X receptor (LXR), peroxisome proliferator-activated receptor (PPAR), pregnane X receptor (PXR), and farnesoid X receptor (FXR) are permissive NRs and function by ligand binding to either heterodimeric partner [13]. Conditional permissive heterodimers are when the ligand-dependent transcriptional activity of RXR appears "subordinated" to the binding of the ligand to its partner [14-16].

Class III NR are orphan receptors meaning that no endogenous ligand has been identified for their activation [17, 18]. It is believed this class of NR does not need a ligand for activation. An example of a homodimeric orphan receptor is RevERbAα which oversees the regulation of the cyclic expression of *BMAL1* [19]. *BMAL1* is a gene important within the mammalian circadian clock [20]. An example of a monomeric orphan NR is steroidogenesis factor-1 (SF-1). SF-1 is

expressed in steroidogenic tissues and loss of SF-1 results in organ development failure during embryogenesis [21, 22].

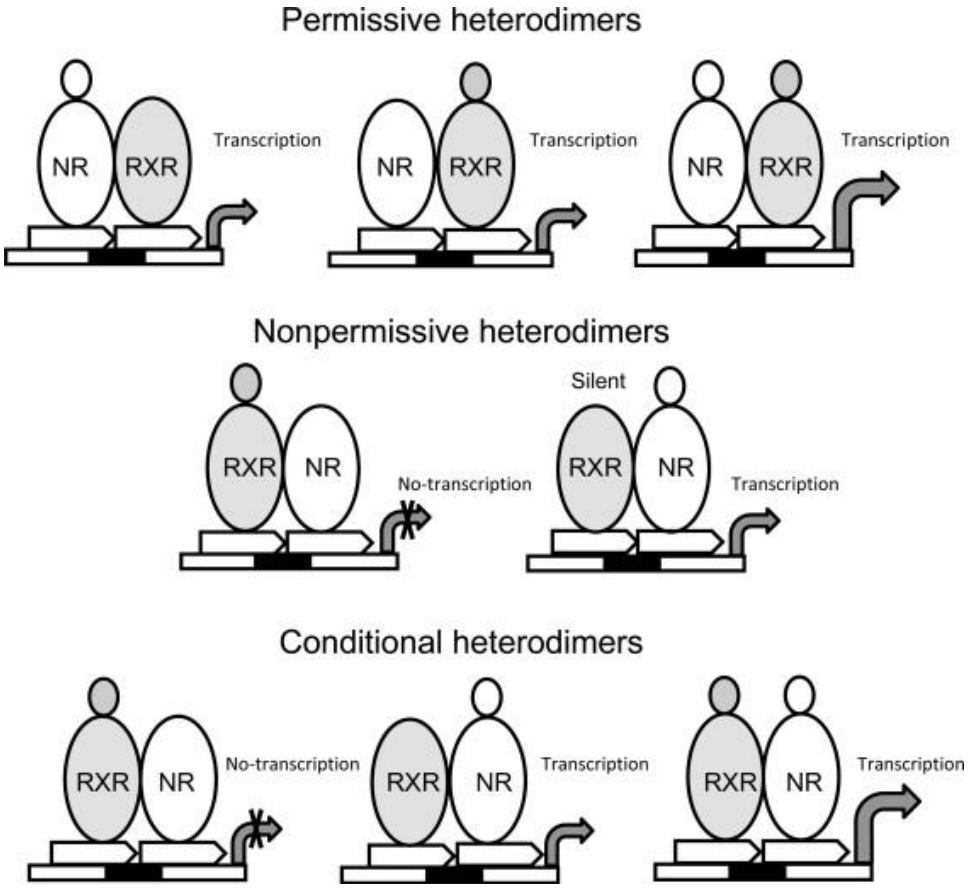

Note: From Brtko, J., and Z. Dvorak. "Triorganotin compounds-ligands for "rexinoid" inducible transcription factors: biological effects." *Toxicology letters* 234.1 (2015): 50-58. Copyright Elsevier 2015. Reprinted with permission.

Figure 1. Division of RXR – "Partner" nuclear receptor heterodimers into three groups: permissive, non-permissive, and conditional.

Nuclear Receptor FDA Approved Drugs

NR ligands are lipophilic small molecules that can be easily modified for drug design. For this work, we focused on two NRs: RXR and RAR. Ligands that

specifically bind to RXR are known as rexinoids and ligands that bind to RAR are called retinoids. Retinoids have been widely studied within the epidermis and dermis for skin concerns caused by ageing and for acne. All-*trans* retinoic acid (ATRA) is a Food and Drug Administration (FDA) approved retinoid. The drug's generic name is Tretinoin and its trade name is Vesanoid. ATRA has also been used as an oral treatment option for acute promyelocytic leukemia (APL) [23].

However, ATRA has been shown to impede carcinogenesis in numerous other cancer models by inhibiting the growth of abnormal cells and inducing apoptosis of these cells [24]. In pancreatic ductal adenocarcinoma (PDAC) ATRA was shown to reduce the over-activation of pancreatic stellate cells (PSCs) thus providing a treatment option for this aggressive malignancy [25]. ATRA induced apoptosis in liver cancer Hep3B cells when used in treatment with bisdemethoxycurcumin (BDMC) [26]. Lan et al. revealed ATRA treatment reduced the invasive potency of human thyroid carcinoma cell lines [27]. In human breast cancer, ATRA therapy inhibited cancer cells [28].

9-*cis* retinoic acid (9cRA) is a pan-agonist in that it can bind to both RXR and RAR. 9cRA's trade name is Alitretinoin and is used as a topical treatment for skin sores caused by Kaposi's sarcoma [29]. Although proven to have several beneficial effects, ATRA and 9cRA have grade 3 toxicities which include elevated serum calcium triglycerides, and cholesterol, noncardiogenic pulmonary edema, headaches, and various skin toxicities [30, 31].

Bexarotene (brand name Targretin) was the first FDA-approved rexinoid, used for the treatment of cutaneous T-cell lymphoma (CTCL) (Fig. 2) [32]. CTCL is a rare type of non-Hodgkin lymphoma where T-cells become abnormal and

begin to attack the skin [33]. Symptoms of CTCL include raised round patches of skin, rash-like skin redness, skin itchiness, and enlarged lymph nodes. Targretin has been shown to be highly selective for RXR [34-36]. The selectivity helps in reducing the toxic side effects that are normally seen with ATRA and 9cRA. Although Targretin is not as toxic as ATRA and 9cRA, oral usage significantly increases serum triglycerides in CTCL patients. To see if the dosage was the reason for the toxicity, a lower dosage of Targretin was tested and resulted in hyperlipidemia for 83% of patients. Targretin has also been tested for several other cancer models such as, colon cancer [37], breast cancer [38], and lung cancer [39]. Targretin showed promising results in a proof-of-concept (POC) clinical trial for non-small cell lung cancer [40, 41]. Although Targretin has been shown to have several positive effects within cancer, the mechanism of action is still not well understood. Here at the University of Alabama at Birmingham we saw this as a good drug target to synthesize a rexinoid with the beneficial effects of Targretin without the toxicities. To accomplish this we hypothesized that if we synthesize a ligand that only stimulates signaling through RXR-RAR we would reduce the toxicities. Why we hypothesizes this is because it has been shown that Targretin stimulates signaling through the RXR-LXR heterodimers in the liver [42, 43]. Which could potentially be why treatment of Targretin induces triglyceride levels since the RXR-LXR pathway modulates triglycerides.

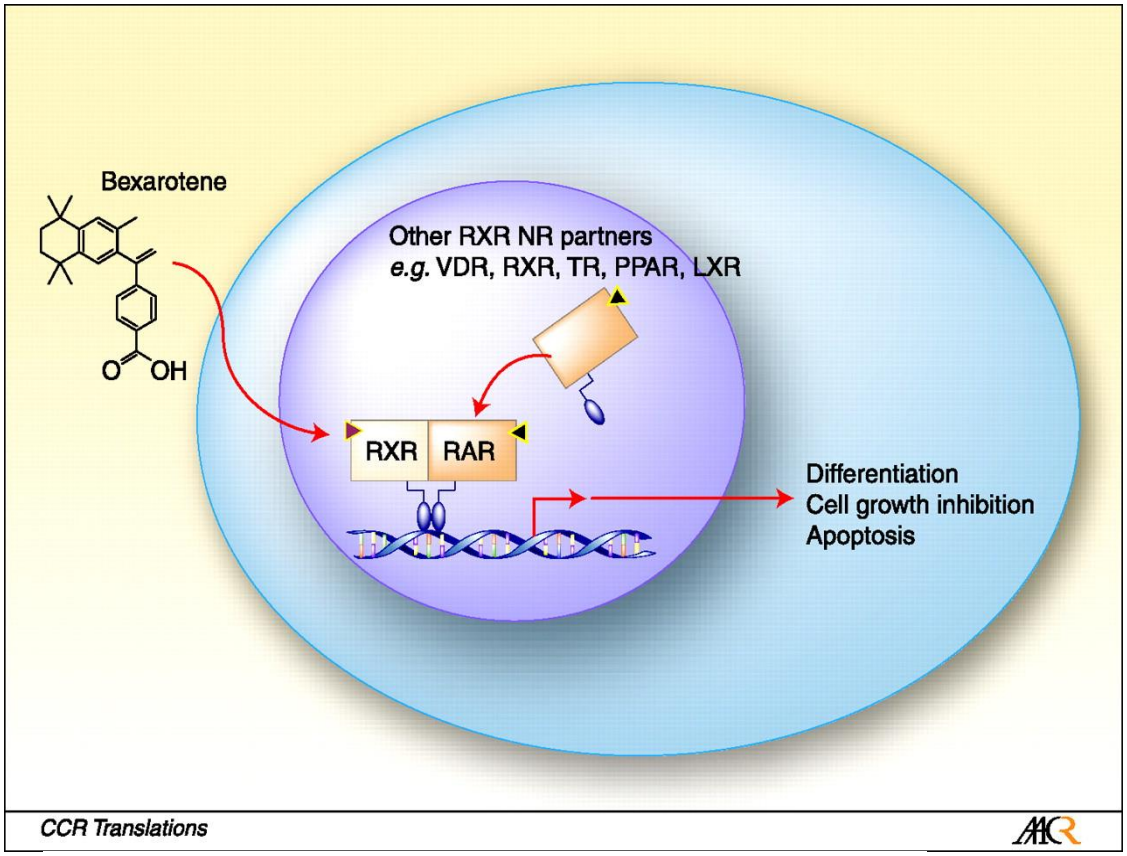

Note: From McNamara, Suzan, and Wilson H. Miller. "Expanding the use of retinoids in acute myeloid leukemia: Spotlight on bexarotene." *Clinical Cancer Research* 14.17 (2008): 5311-5313. Copyright Clinical Cancer Research 2008. Reprinted with permission.

Figure 2. The binding of bexarotene to RXR activates multiple pathways through heterodimerization with several nuclear receptors to regulate the expression of genes important in differentiation, apoptosis, and cell growth.

Characterization of RXRs

The family of RXR proteins is central to development and homeostasis. Three distinct genes encode three RXR isoforms, RXRα (NR2B1), RXRβ

(NR2B2), and RXRγ (NR2B3) with an X signifying that the endogenous ligand for RXR is unknown [44]. RXRα is the most prominent isoform expressed in the skin and is also expressed in the liver, epidermis, kidney, and intestine. Mice that have had RXRα knockout were embryonic lethal with hypoplasia of the myocardium and cardiac failure occurring around E14.5 [45]. RXRβ expression can be found in all tissues and RXRγ is predominantly expressed in the brain, skeletal and muscle tissue. Embryos with RXRα knockout displayed birth defects that mimic vitamin A deficiency [46]. RXRβ null mice had a lethality rate of 50% and male mice were sterile. RXRγ had a decrease in food intake correlating with an increased metabolic rate [47]. Overall studies using gene silencing in mice showed that RXRα null has the greatest developmental impact. For our work we focused on RXRα due to it being the isoform with the greatest expression in the skin.

Stephan Wainwright once said, “Structure without function is a corpse… function without structure is a ghost”. In order to better understand a proteins mechanism of action it is equally as important to investigate both functional and structural components of RXR. RXR can exist in three main states: homotetramer, dimer, and as a monomer. At physiologically relevant concentrations, RXR has the ability to form stable tetramers that dissociate into dimers and monomers upon ligand binding however the mechanism is still elusive [48-51]. In 2000 the first X-ray crystal structure of the apo-RXRα-ligand binding domain (LBD) homotetramer was resolved. The homotetramer interface involves helices 3, 11, and 12. The coactivator binding site involves helices 3 and 12 and due to the homotetramer interface involving both of these regions, it inhibits coactivator interactions (Fig. 3)

[52]. Given that RXR homotetramers bury the coactivator binding site it makes senses why they are transcriptionally silent.

The function of the RXR homodimer is still not well understood. However, there have been studies done by Jpenberg, Annemieke et al. using chromatin immunoprecipitation that showed RXR homodimers selectively bound to functionally peroxisome proliferator-activator receptor response elements (PPREs) and induced transcription [53]. RXR LBD homodimers were shown to form with relatively low affinity when compared to RXR heterodimerizing with RAR [48]. Given the lack of understanding of the RXR homodimer, our work aimed to understand how various rexinoids binding to RXR induced structural and dynamic differences

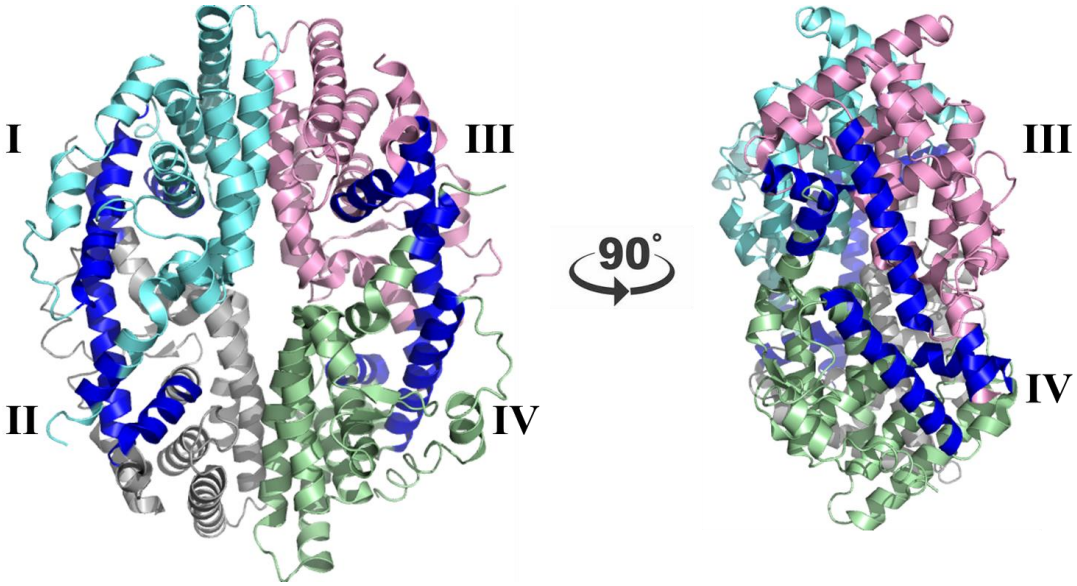

Figure 3. RXR homotetramer displays the four RXR monomers bound together (I-IV). Each monomer is labeled in different colors (I) cyan, (II) grey, (III) pink, and (IV) green. The coactivator binding site is labeled in blue for each monomer. The structure was then turned 90 degrees to display two monomers, III and IV. The side profile of the homotetramer allows for the visualizing of the occupied coactivator binding site.

RXR Structural Domains and Heterodimer Partners

NRs are modular in structure and contain either five or six domains. The DNA binding domain (DBD) is a highly conserved domain containing two zinc finger motifs, a COOH-terminal extension, and a pair of α helices. The two zinc finger motifs are known as the P-box and the D-box. The P-box consists of C1 to C4 and the D-box is from C5 to C8. The P-box is responsible for receptor response element sequence specificity and the C-box is involved in receptor dimerization and half-site spacing. The structural DNA recognition site is formed when the zinc finger motifs chelate to a Zn (II) ion. DNA sequence specificity is confirmed through the binding of HREs, hexameric half-sites configured as palindromes, inverted palindromes or direct repeats located in the control regions of the target genes. Giguiere et al. crystallized the first NR DBDs which were the GR and ER DBD homodimers bound to DNA [54].

The RXR ligand-binding domain (LBD) is the primary focus of these studies because this is the site of ligand binding, coregulatory protein interaction, dimerization, and where the ligand-dependent activation function-2 (AF-2) is located [55]. The transcriptional activities of RXR are modulated by ligand binding which induces conformational changes that reposition helix 12 into an active conformation, creating a shaping preference for coactivator recruitment. RXR homodimers bind to the asymmetric direct repeat (DR1) with preferential binding to the 3' half-site. The LBD is connected to the DBD by a flexible linker region. The LBD is arranged in a three-layer alpha-helical sandwich (Fig. 4A). The first layers are helices 1 and 3. The middle layer consists of helices 4, 5, 8, 9, and the β-sheet. The last secondary elements involve helices 6, 7, 10, and 11. The ligand-

binding pocket (LBP) is located in residues of helices 3, 5, 7, and 11 (Fig. 4B). The size of the LBP varies amongst NRs and reflects the ability to accommodate

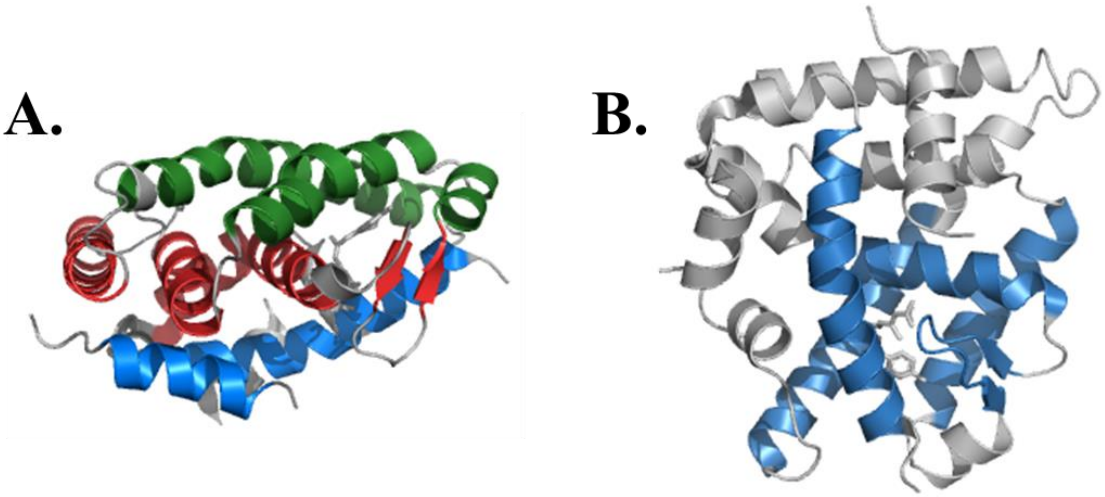

Figure 4. RXR structural features. (A) Regions of RXR associated with the alpha helical sandwich. Top layer of the sandwich is labeled in green. Middle section is mapped in red and bottom portion is colored in blue. (B) Regions involved in the ligand binding pocket of RXR shaded in blue.

differently sized ligands. For example, PPARγ can bind differently sized ligands due to its large LBP [56]. RXR has a smaller binding pocket of about 400- 500 A [57]. Once a ligand binds to the LBD a structural conformation occurs allowing a co-activator to now come in and bind to the AF-2 site. The binding also causes the conformation of helix 12 to go from an extended position to be closer to the ligand-binding pocket.

There is no common quaternary architecture of NR complexes, each NR complex has distinct variations. The architecture of NR complexes has been studied by Chandra et al. who compared the full-length X-ray crystal structures of RXRα heterodimerized with RARβ, PPARγ, and LXRβ. Figure 3 displays the full-length structure of numerous heterodimerization complexes. The LBDs of RXR

and RAR are parallel to one another. For RAR the DBD is directly under the LBD but for RXR the DBD does not interact with the LBD and is instead interacting with the other side of the DNA. In the structure of RXR-LXR both of their LBD's interact with one another but the DBDs are located beneath the others partners (Figure 3d). The full structures create an "x" shaped conformation. Further investigation into commonalities within each of the crystal structures revealed the positioning of helices 9 and 10 of RXR's partners form similar domain-domain interfaces between the LBDs and DBS (Figure 5e-h). Overall, RXR's domains are not consistently in the same conformation within these structures possibly due to RXR's flexible hinge region and lack of domain-domain interactions.

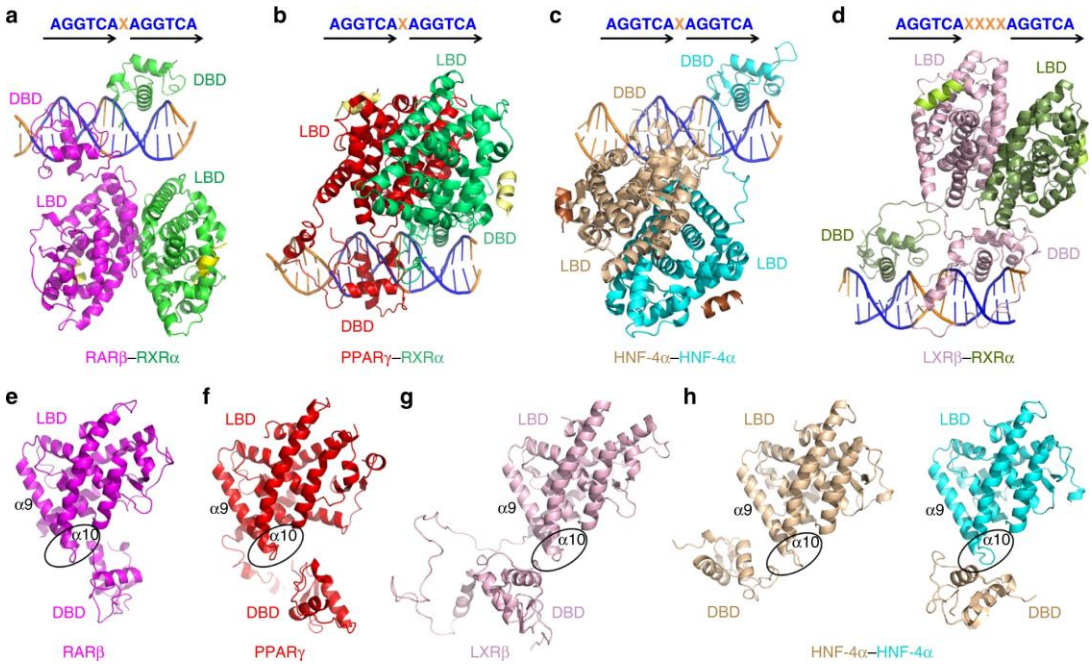

Note: From Chandra, Vikas et al. “The quaternary architecture of RARβ–RXRα heterodimer facilitates domain–domain signal transmission." *Nature communications*. 8, 868 (2017). Copyright Nature communications 2017. Reprinted with permission.

Figure 5. The different architectures of multi-domain NRs on DNA.

RXR Dimerization Interfaces

RXR homodimers have two dimerization interfaces: DBD and LBD interfaces. The DBD of RXR homodimers buries 400 $A^{\circ 2}$ of the solvent-exposed area [58]. The dimerization interface of LBD is 1,830 $A^{\circ 2}$ making it much larger than the DBD interface. The RXR LBD homodimer dimerization interface consists of helices 7, 8, 9, and 10 and the loops between helix 8 and helix 9 and helix 9 to helix 10. We investigated the differences of the homodimer interfaces of (RXR)2 with UAB30 bound (RXR-UAB30) and (RXR)2 with Targretin bound (RXR-Targretin).

The Proteins, Interfaces, Structures, and Assemblies (PISA) server was used to analyze the dimerization interface of two RXR homodimer X-ray crystal structures: Targretin (PDBid: 4K6I) and UAB30 (PDBid: 4K4J) (Table 1). The dimerization interface hydrogen bonds and salt bridges for both involved helices 7, 9, 10, 11, and loops 8 and 10. Targretin had an additional interaction: (H9) Lys^{405} - Glu^{401} (H9) (Table 1). The extra interaction in the interface caused by Targretin binding to RXR could indicate that Targretin stabilizes the RXR homodimer more than UAB30. The other interactions were identical except for UAB30 which had (H7) Lys^{356} - Asp^{379} (L8) and Targretin had (L8) Lys^{417} - Glu^{394} (H9) (Table 1). These results indicate that Targretin binding to RXR homodimer induces more interactions in helix 9 compared to UAB30. Given these observations, I predict that the dynamics of RXR-UAB30 and RXR-Targretin will differ in helix 9.

RXRα-RARβ heterodimerization LBD interface involves similar regions of the RXR homodimer (Table 2). Vivat-Hannah et al. mutated a residue on helix 9 (Tyr^{402}) to an alanine which weakened RAR heterodimerization with RXR but increased homodimerization of RXR-RXR [58]. This work reveals that although RXR-RAR heterodimer have similar dimerization surfaces, the residues on RXR contribute differently to the stabilization of homodimers and heterodimers. RXRα-LXRα LBD interfaces involve helices 3, 4, 5, 12 for RXR and helices 3, 7, 10/11, 12 for LXR (Table 2). For the RXRα-PPARγ heterodimer dimerization interface RXR interacts with PPAR through helices 7, 9, 10, and 11 and PPAR involves helices 9, 10, and 11. The differences in interfaces show how RXR can adapt depending on which NR it is bound to, possibly due to its flexible hinge region.

UAB30			
Hydrogen Bonds		Salt Bridges	
Interaction	Distance [Å]	Interaction	Distance [Å]
(L8) Lys^{381} - Glu^{352} (H7)	3.23	(L8) Lys^{381} - Glu^{352} (H7)	3.23
(L10) Arg^{421} - Asp^{379} (L8)	2.70	(L10) Arg^{421} - Asp^{379} (L8)	2.70
(H7) Lys^{356} - Asp^{379} (L8)	3.49	(L10) Arg^{421} - Asp^{379} (L8)	3.92
(L10) Arg^{421} - Asp^{379} (L8)	3.05	(H7) Lys^{356} - Asp^{379} (L8)	3.49
(H9) Tyr^{397} - Gly^{413} (H10)	3.40	(L10) Arg^{421} - Asp^{379} (L8)	2.95
(H11) Arg^{426} - Pro^{423} (H11)	3.30	(L10) Arg^{421} - Asp^{379} (L8)	3.05
Targretin			
Hydrogen Bonds		Salt Bridges	
Interaction	Distance [Å]	Interaction	Distance [Å]
(L8) Lys^{381} - Glu^{352} (H7)	2.84	(L8) Lys^{381} - Glu^{352} (H7)	2.84
(L10) Arg^{421} - Asp^{379} (L8)	2.67	(L10) Arg^{421} - Asp^{379} (L8)	3.82
(L10) Arg^{421} - Asp^{379} (L8)	3.17	(L10) Arg^{421} - Asp^{379} (L8)	2.67
(L8) Lys^{417} - Glu^{394} (H9)	3.74	(L10) Arg^{421} - Asp^{379} (L8)	3.17
(H9) Lys^{405} - Glu^{401} (H9)	3.38	(L10) Arg^{421} - Asp^{379} (L8)	2.98
(H9) Tyr^{397} - Gly^{413} (H10)	3.26	(L8) Lys^{417} - Glu^{394} (H9)	3.74
(H11) Arg^{426} - Pro^{423} (H11)	3.39	(H9) Lys^{405} - Glu^{401} (H9)	3.38

Table 1. Dimerization interface interactions of RXR in complex with UAB30 and RXR bound to Targretin.

RARβ : RXRα			
Hydrogen Bonds		Salt Bridges	
RARb : RXRa	Distance [Å]	RARb : RXRa	Distance [Å]
(L 8/9) Gln^{333} - Glu^{357} (H7)	3.87	(H9) Arg^{357} - Glu^{406} (H9)	2.98
(H9) Arg^{357} - Glu^{406} (H9)	2.75	(H9) Arg^{357} - Glu^{406} (H9)	2.75
(H10/H11) Lys^{369} - Glu^{395} (H9)	3.44	(H10/H11) His^{365} - Glu^{399} (H9)	3.74
(H10/H11) Lys^{369} - Glu^{399} (H9)	3.03	(H10/H11) Lys^{369} - Glu^{395} (H9)	3.44
(H10/H11) Arg^{378} - Ser^{432} (H11)	3.38	(H10/H11) Lys^{369} - Glu^{399} (H9)	3.03
(C-term) Leu^{416} - Gly^{346} (H7)	3.23	(H10/H11) Lys^{369} - Glu^{399} (H9)	3.50
(L 8/9) Gly^{330} - Lys^{361} (L7)	3.88	(L8/9) Asp^{331} - Arg^{426} (H11)	3.17
(L8/9) Asp^{331} - Arg^{426} (H11)	3.17	(L8/9) Asp^{331} - Arg^{426} (H11)	2.93
(L8/9) Asp^{331} - Arg^{426} (H11)	2.93	(L8/9) Asp^{331} - Arg^{426} (H11)	3.11
(L8/9) Asp^{331} - Arg^{426} (H11)	3.11	(L8/9) Asp^{331} - Lys^{361} (L7)	3.06
(L8/9) Asp^{331} - Lys^{361} (L7)	3.06	(H9) Asp^{342} - Lys^{361} (L7)	3.80
(H9) Asp^{342} - Lys^{361} (L7)	3.80	(H9) Asp^{342} - Lys^{361} (L7)	3.80
(H9) Asp^{342} - Lys^{361} (L7)	3.80		
(H9) Glu^{350} - Gly^{418} (H10)	3.89		
(H10/H11) Thr^{375} - Arg^{431} (H11)	3.87		
(H10/H11) Ser^{379} - Arg^{431} (H11)	3.44		
(C-term) Glu^{414} - Ile^{350} (H7)	2.89		
(C-term) Glu^{414} - Ala^{349} (H7)	2.65		
(C-term) Glu^{414} - Gly^{348} (H7)	3.18		
LXRα : RXRα			
Hydrogen Bonds		Salt Bridges	
LXRa : RXRa	Distance [Å]	LXRa : RXRa	Distance [Å]
(H10/H11) Arg^{427} - Asp^{273} (H3)	3.66	(H10/H11) Arg^{427} - Asp^{273} (H3)	3.66
(H3) Arg^{248} - Asp^{295} (H4)	2.78	(H3) Arg^{248} - Asp^{295} (H4)	2.78
(H3) Lys^{271} - Met^{455} (H12)	3.18	(H7) Glu^{332} - Arg^{302} (H4)	3.21
(L1) Gln^{243} - Leu^{294} (H5)	2.87	(H7) Glu^{332} - Arg^{302} (H4)	3.73
(H7) Glu^{332} - Arg^{302} (H4)	3.21		
(H7) Gln^{330} - Arg^{302} (H4)	2.93		
(H12) Glu^{330} - Thr^{450} (H12)	3.05		
(H12) Glu^{330} - Thr^{450} (H12)	2.91		
(H12) Glu^{330} - Phe^{451} (H12)	3.02		
(H12) Glu^{330} - Leu^{452} (H12)	3.24		

Table 2. Dimerization interface interactions of RARβ : RXRα, LXRα : RXRα, and PPARγ : RXRα.

Characterization of Rexinoids

9-cis-retinoic acid (9cRA) was the first RXR agonist discovered and was believed to be RXR's natural ligand [59, 60]. To date, several studies have called the role of 9cRA as an endogenous RXR ligand into question. Costaridis et al. were not able to detect the ligand in zebra fish [61]. Further studies were done on the spinal cords of mouse embryos that were able to detect ATRA and RXR but not 9cRA [62]. Schmit et al. used an automated solid-phase extraction procedure and were not able to detect 9cRA in liver, kidney, testes, or brain tissues [63]. These and numerous other studies show that 9cRA is unlikely RXR's endogenous ligand. 9cRA can bind both RXR and RAR, however all-*trans* retinoic acid is a more abundant natural ligand for RAR. 9cRA has been shown to effectively prevent chemically-induced mammary cancers in mouse and rat cancer models, but high levels of associated toxicities limit its application in humans. Interestingly, through *in vitro* assays, 9cRA was shown to increase the formation of RXR homodimers.

Structural studies on NRs mainly focus on RXR's bound partner [64]. Studies that do have RXR present consistently have the protein bound to 9cRA. Without RXR several NR would not be able to function, it still is not well understood how a ligand affects RXR's LBD and its partner. In efforts to understand the ligand-induced structural mechanism of RXR, our group has synthesized two separate classes of rexinoids, using 9cRA as a template (Fig. 6**).** Class I and II rexinoids have a conformation constraint of the C6-C7 bond which allows for selective binding to RXR. Class I rexinoids contain a 9Z-tetraenoic acid chain bonded to a disubstituted cyclohexenyl ring. Class II rexinoids pose the same

9Z-tetraenoic acid chain bonded to a tetralone ring. From the library of synthesized rexinoids, a class II rexinoid, UAB30, did not increase serum triglycerides in rodents and humans but was nevertheless effective in preventing cancer in rodents [65]. UAB30 has shown to be well tolerated by healthy human volunteers [66]. Currently, UAB30 is undergoing Phase II human clinical trials for the treatment of non-melanoma skin cancer. Non-melanoma skin cancer is the target for Phase II clinical trials over melanoma skin cancer due to melanoma skin cancer being more resistant to several drug treatments [67] [68] [69]. The two most common types of non-melanoma skin cancer are basal cell carcinoma and squamous cell carcinoma. Basal cell carcinoma is the most common type of skin cancer and begins in the deepest part of the epidermis specifically, in the basal cells [70]. Squamous cell carcinoma affects the squamous cells which are in the upper part of the epidermis [71].

The number of non-melanoma skin cancer patients has been increasing by ~8% since 1960 [72, 73]. Current treatments for non-melanoma skin cancer are surgery, curettage, cryotherapy, and chemotherapy [74, 75]. The invasiveness of non-melanoma treatments and the rate of incidences make the condition an important target for research.

While UAB30 clearly shows promise as a low-toxicity chemopreventive drug, the mechanism of UAB30 action at the molecular level is poorly understood. By modifying UAB30, we will be able to understand how structurally similar rexinoids produce dynamically different profiles.

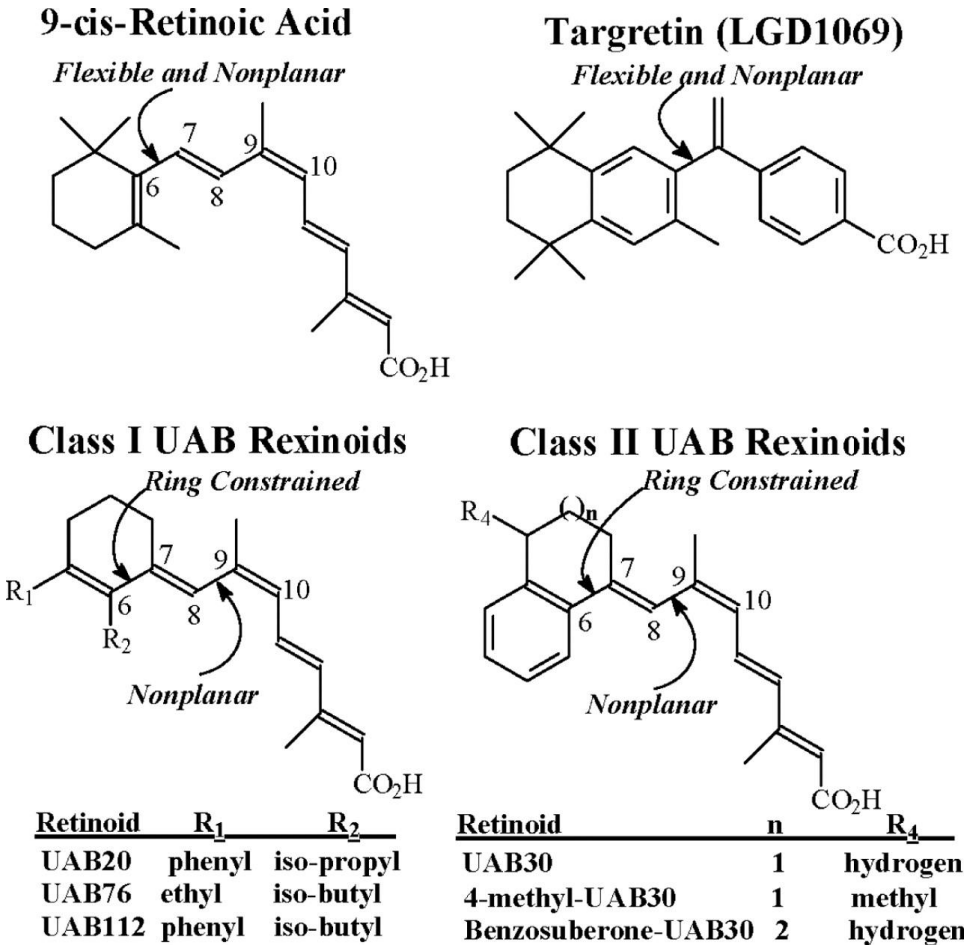

Note: From Grubbs, Clinton J., et al. "Efficacy of new retinoids in the prevention of mammary cancers and correlations with short-term biomarkers." *Carcinogenesis* 27.6 (2006): 1232-1239. Copyright Carcinogenesis 2006. Reprinted with permission.

Figure 6. Structures of the retinoids under investigation in this study.

Hydrogen Deuterium Exchange Mass Spectrometry

In pursuit of understanding proteins, the interplay between structure, dynamics, and functions need to be investigated. Crystallography has been used for over 100 years as a means of visualizing structural components [76]. As humans,

vision is a prominent sense which is why we have continued to eagerly build the 3D models of structures. Structure is what defines and enables the function of proteins, therefore we need to determine the structure of the protein to understand its function. However, macromolecules are not static but are dynamic at their physiological temperatures and dynamics are also believed to be related to biological function. As part of the biomolecular mechanism proteins can undergo fluctuations or motions [77]. Dynamic changes are a common part of protein function, especially within the NR mechanism. Ligand binding to the LBP of a NR induces helix 12 to become more dynamic, allowing for coactivators to bind and stabilize the coactivator binding site and recruit transcriptional machinery [78, 79]. However, in this work, we use hydrogen deuterium exchange mass spectrometry (HDX MS) to go beyond the coactivator binding site to investigate whether other dynamics influence NR transcriptional activation.

HDX-MS is a technique used to detect protein folding, ligand-induced conformational changes, the formation of protein/protein interfaces, and structural dynamics. The technique was developed by Linderstrom-Lang in the 1950s by the use of a density gradient column [80]. Lang realized that amide hydrogens participate in a continual exchange with the hydrogens of the solvent [80, 81]. Outside of density, hydrogen exchange can be measured through radioactivity through scintillation counting and nuclear magnetic resonance through NMR spectroscopy [82]. In 1991, Katta and Chat were the first to use mass spectrometry as a way to measure hydrogen exchange [83]. For this work we used mass spectrometry where the differences in hydrogen exchange can be detected through a mass increase. The mass of hydrogen is equal to 1.0078 Da where the mass of

deuterium is 2.0141 Da. Within the labeling experiment, the conditions are as "mild" as possible as to not disrupt the native, folded state. Important factors within the experiment can be divided into two sections: what is being controlled and what is being measured. pH and temperature are what is being controlled and solvent accessibility and hydrogen bonding is what is measured. A decrease in deuterium incorporation signifies a decrease in dynamics and an increase in protection. An increase in deuterium exchange is an increase in dynamics and a decrease in protection.

The exchange reaction can either be base-catalyzed (pH = 7) or acid-catalyzed (pH < 3) [84]. Given that pH of 7 is near a neutral pH the base-catalyzed reactions are primarily used within HDX. pH and temperature units are important within HDX experimental parameters. An increase in one pH unit accelerating the intrinsic exchange rates tenfold. Decreasing of one pH unit slows the intrinsic exchange rates to one-tenth. Similarly to pH, a decrease in temperature decelerates the intrinsic exchange rates. Temperature controls throughout the exchange experiment allows for the monitoring of back exchange. HDX MS can detect protein folding/unfolding rates from 10^{-3} to $>10^{4}$ seconds [85]. The reason why amide hydrogens are the type of hydrogens measured within HDX MS is because the rates of the side chain hydrogens are very fast and cannot be detected [86]. The amide hydrogens located on the peptide backbone have a partial double bond which reduces the rapid rate of exchange.

HDX MS can be performed by doing intact protein analysis or by protein digestion. Rosa and Richards were the first to incorporate digestion in the chemical hydrogen exchange measurements and showed how digestion can significantly

increase structural resolution [87]. Our group has made use of pepsin digestion as a way to monitor RXR peptide dynamics upon a ligand binding. The range of quantitation for deuterium replacing hydrogen encompasses from zero to the theoretical maximum exchange. When analyzing the theoretical maximum, proline is discarded due to the amino acid not having an amide hydrogen. Pepsin digestion leaves peptides with an N-terminal end [88]. The amide which is on the N terminus is no longer protected and undergoes fast back exchange therefore it is also not considered within the theoretical maximum [89].

HDX-MS allows for populations of exchanged and non-exchanged to be sampled. Within HDX-MS experiments there can be two different exchange kinetics: EX1 and EX2. EX1 kinetics can have two distributions within the isotope cluster. The first being an envelope representing a more unfolded species and a lower-mass envelope demonstrating a more folded species. For EX1 kinetics the closing rate is slow relative to the chemical exchange rate [90, 91]. In EX2 kinetics the rate is faster than the intrinsic rate of exchange. EX2 involves the amide hydrogens briefly being exposed for exchange also thought of as small and fast local structural fluctuations. There is one population which shows a gradual incorporation of deuterium as time in deuterium buffer increases.

The master peptide list in HDX MS comes from data independent acquisition (MSe). There are three main steps to the MSe process: separation, generation of a complete MS dataset, and alignment of spectra and data interpretation [92]. The first step, separation, involves utilize an UltraPerformance liquid chromatography (UPLC) to separate the peptide fragments. The second step is the generation of a complete MS data set which involves the mass spectrometer

continuously cycling between two states. The first state involves all ions being transmitted from the ion source to the collision cell, then to the mass analyzer without being fragmented. These ions are termed precursor ions or parent ions. The second state goes through the same process except for once the ions are in the collision cell the collision energy is increased to generate fragment ions. The last step is the alignment of spectra and data interpretation. The precursor and fragment ions are then associated via their retention times. The parameters in the peptide list involve the peptide sequence, start residue, end residue, undeuterated m/z, charge state, and retention time. We utilization a LEAP robot to aid in the preparation of samples by mixing deuterium with protein, quenching, and injecting. The software associated with the LEAP robot makes sure that only one experiment is occurring at a time.

Each HDX-MS experiment produces a great amount of data so data visualization is important. For our work we utilize two main methods for data visualization: heat maps mapped on to X-ray crystal structures and difference maps. Heat maps displayed on the X-ray crystal structures are labeled with shades of blue (decrease in dynamics) and shades of red (increase in dynamics). Difference maps display the peptide sequence, the location of the peptide sequence, and numerous HDX-MS datasets. Difference maps allow for the quick visualization of multiple data sets at various time points.

Our HDX-MS workflow involves the immersion of recombinant RXR-LBD homodimer in a deuterated buffer to produce a series of on-exchange time points. The time points are each quenched in acid followed by immediate injection into the chilled liquid chromatography (LC) system for in-line digestion with the

enzyme, pepsin. The digested peptides are then captured by a short C18 trap and then eluted across a longer C18 analytical column for electrospray ionization into the Synapt G2-Si MS. Individual peptide ions are then identified and tracked across the time points to determine the extent of deuterium incorporation. Once the rates of deuterium incorporation are plotted the cumulative results are then "color-coded" onto the structure of the RXR-LBD (Fig. 7).

Our group has been extensively researching RXR's function, structure, and dynamics for several years through the development of RXR specific ligands (rexinoids). Preliminary studies included crystallizing RXR in complex with each developed rexinoid. Electron density graphs revealed the rexinoid's positions and interactions with the LBP (Figure 8). Overlay of UAB30 (yellow), Targretin (magenta), and 9cRA (green) in the ligand-binding pocket (LBP) revealed that all three rexinoids bind in similar L-shaped conformations (Figure 8) [93]. In our previous work, we analyzed both UAB30 and Targretin's binding to RXR using HDX MS and compared the results to 9cRA [94]. The study involved the ternary structure of RXR-rexinoid-coactivator (CoA). Our results revealed that UAB30 and Targretin bound to RXR reduced the dynamics in helices 3, 11, and 12. 9cRA bound to RXR only reduced the dynamics of helices 3 and 11. Through the analysis when Targretin was present it had the largest effects in the CoA binding site followed by UAB30 and then 9cRA.

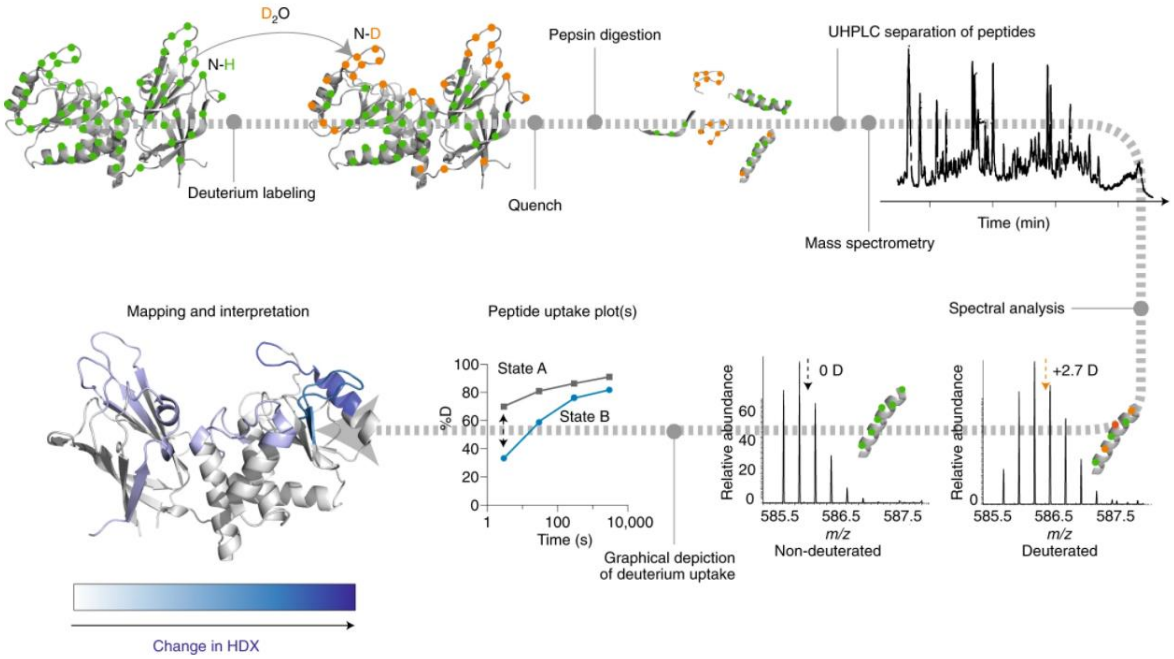

Note: From Masson, Glenn R., et al. "Recommendations for performing, interpreting and reporting hydrogen deuterium exchange mass spectrometry (HDX-MS) experiments." *Nature methods* 16.7 (2019): 595-602. Copyright Nature methods 2019. Reprinted with permission.

Figure 7. The common ‘bottom-up’ or ‘local’ HDX-MS experiment.

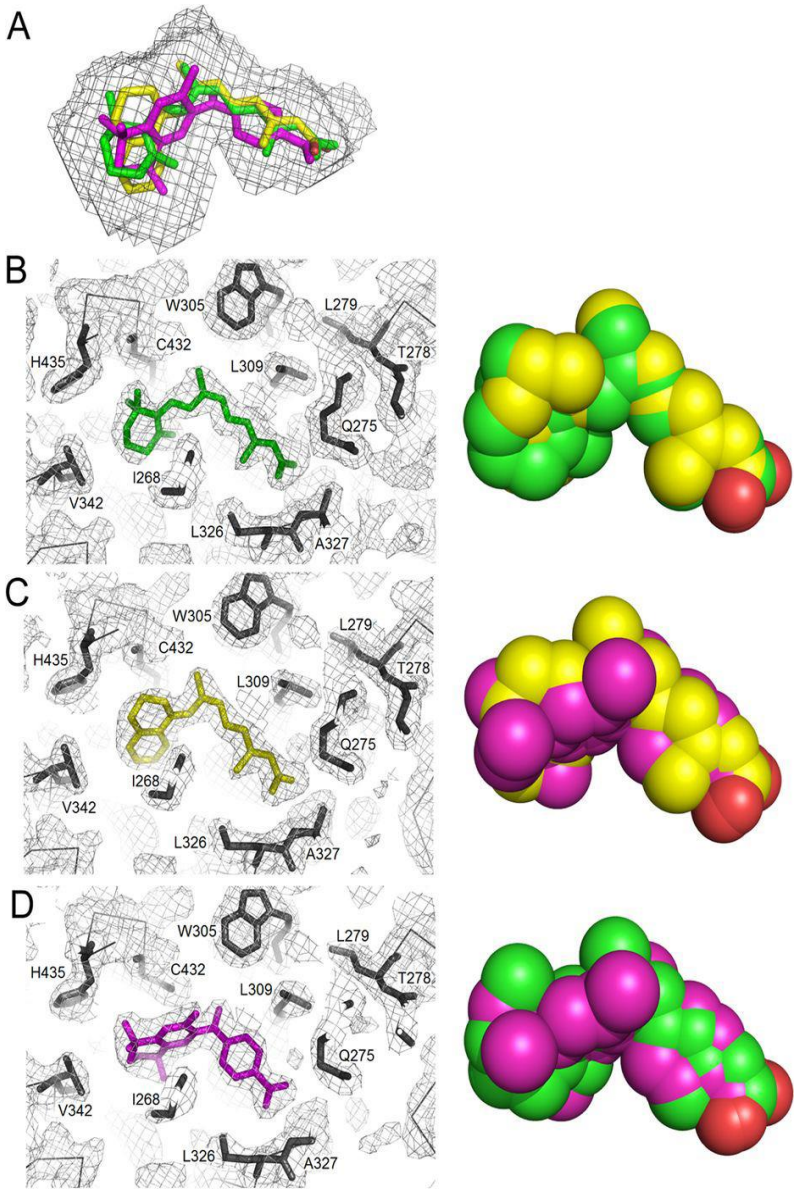

Note: From Boerma, LeeAnn J., et al. "Defining the communication between agonist and coactivator binding in the retinoid X receptor α ligand binding domain." *Journal of Biological Chemistry* 289.2 (2014): 814-826. Copyright Journal of Biological Chemistry 2014. Reprinted with permission.

Figure 8. Conformation of rexinoids and 9cRA in the ligand binding pocket of holo-hRXRα LBD.

Nuclear Receptor Associated Coregulatory Proteins

NR transcriptional regulation involves co-repressor bound to NR to maintain transcriptional repression. Upon a ligand binding to the NR a conformational change occurs, removing the corepressor allowing for a coactivator to bind. The first gene family to be classified and characterized as coactivators for NRs were the steroid receptor coactivator family (SRC) [95]. The members of this family act as bridging molecules by assisting in the assembly of the transcriptome complex. There are three members in the SRC family: SRC-1, SRC-2, and SRC-3. SRC-1 is also known as NCOA1, SRC-2 is also referred to as NCOA2, GRIP-1, and TIF2, and SRC-3 is known as NCOA3, ACTR, AIB1, p/CIP, RAC3, and TRAM-1 [96]. The SRC family contain four structural domains: the N-terminal domain, the central domain, and two C-terminal domains. The N-terminal domain interacts with numerous transcription factors, such as p53, STAT6, and TEF4 and is the most conserved domain among the three members. The central domains consist of three LXXLL motifs with the "X" signifying any amino acids. These motifs allow for direct interaction with NR LBDs. The two C-terminal domains are known as AD1 and AD2 and are responsible for recruiting co-coregulators for chromatin remodeling [97].

SRC's are not the only coactivator family, there have been more than 400 coregulators identified and understanding their biology within the NR is not well understood. SRCs have been shown to play roles in various cancers such as lung cancer (SRC-3), hepatic cancer (SRC-2, SRC-3), prostate cancer (SRC-1, SRC-2, SRC-3), breast cancer (SRC-1, SRC-3), ovarian cancer (SRC-1).

In previous studies by Boerma et al., they investigated the binding of coactivator (CoA) GRIP-1 binding to RXR through X-ray crystallography [94]. In this work, they used the GRIP-1 coactivator peptide that contained 13 residues (^{686}KHKILHRLLQDSS^{698}). Within this peptide, there was one of the LXXLL motifs which adopted a two-turn amphipathic helix (Figure 7). In Figure 7A, the hydrophobic residues (Ile^{689}, Leu^{693}, Leu^{690}, and Leu^{694}) were labeled in green and the hydrophilic residues (Lys^{686}, His^{687}, His^{691}, Lys^{688}, Arg^{692}, Asp^{696}) were colored in blue. In Figure 7B, there is an overlay of GRIP-1 as seen in the three ternary crystal structures of RXR. The two charge clamps between GRIP-1 and RXR are labeled in red dashed lines. A side view of GRIP-1 positioned in the coactivator binding site showed the positions of two key residues in helix 12 (Glu^{456} and Ala^{457}) to Lys on GRIP-1 (Figure 7C).

They went on to compare the crystal structures of RXR-9cRA to the ternary structure of RXR-rexinoid-GRIP-1 which revealed four structural changes. As stated in Boerma et al. “These changes are as follows: 1) the carboxylate group of Asp^{273} (H3) forms a strong interaction with Thr449 and Phe^{450} of H12; 2) the phenyl ring of Phe^{277} (H3) forms a π-hydrogen bond with Phe^{450} (H12); 3) the guanidinium group of Arg^{302} (H4) forms ionic interactions with Glu^{453} and Glu^{456} of H12; and 4) H11 changes its helical axis by 10°, and Phe^{437} (H11) moves from a solvent-exposed environment to one that interacts with hydrophobic side chain carbon atoms on Leu^{455} on H12.” [94]. The conclusions of this work helped guide the RXR structural investigation into focusing not just on helix 12 but also on helix 3.

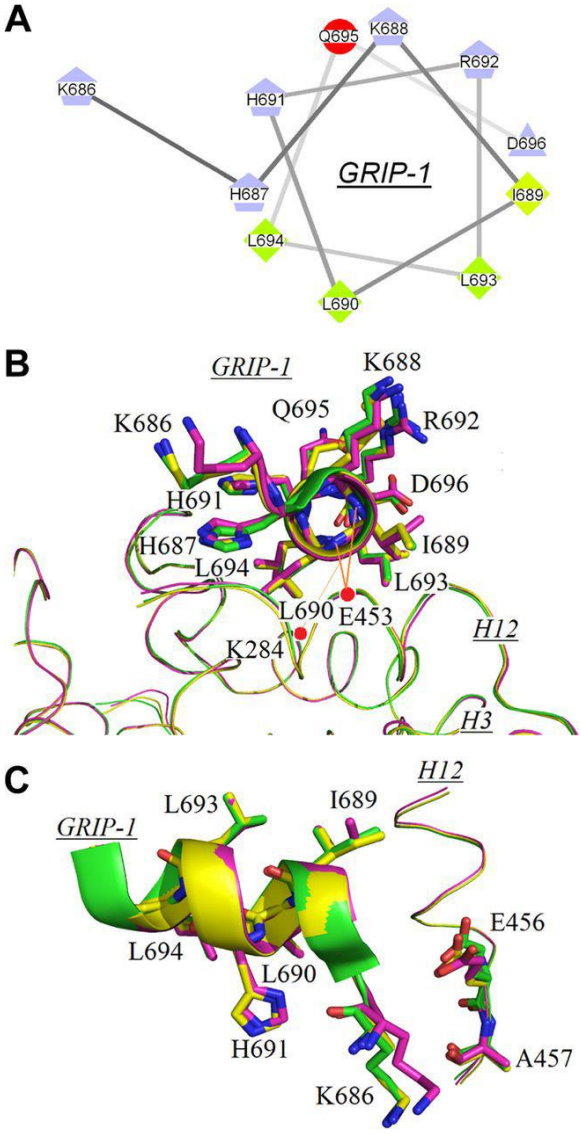

Note: From Boerma, LeeAnn J., et al. "Defining the communication between agonist and coactivator binding in the retinoid X receptor α ligand binding domain." *Journal of Biological Chemistry* 289.2 (2014): 814-826. Copyright Journal of Biological Chemistry 2014. Reprinted with permission.

Figure 9. Interactions of the coactivator peptide GRIP-1 with surface residues on holo-hRXRα –LBD.

CHAPTER II
CONNECTING LIGAND-INDUCED RETINOID X RECEPTOR STRUCTURAL DYNAMICS TO REXINOID AGONIST POTENCY

by

NATHALIA MELO, OLGA V. BELYAEVA, WILHELM K. BERGER, LASZLO HALASZ, JIANSHI YU, NAGESH PILLI, ZHENGRONG YANG, ALLA V. KLYUYEVA, CRAIG ELMETS, VENKATRAM ATIGADDA, DONALD D. MUCCIO, MAUREEN A. KANE, LASZLO NAGY, NATALIA Y. KEDISHVILI, MATTHEW B. RENFROW

In preparation for *Journal of Biological Chemistry*

Format adapted for thesis

ABSTRACT

Retinoid X receptors (RXR) are nuclear transcription factors that partner with other nuclear receptors to regulate numerous physiological processes. Although RXR represents a valid therapeutic target, only a few RXR-specific ligands (rexinoids) have been identified, in part due to the lack of clarity on how rexinoids selectively modulate RXR response. Previously, we showed that rexinoid UAB30 potentiates all-*trans*-retinoic acid (ATRA) signaling in human keratinocytes by stimulating ATRA biosynthesis. Here, we examined the mechanism of action of next-generation rexinoids UAB110 and UAB111 which are more potent *in vitro* than UAB30 and the FDA-approved Targretin. Both UAB110 and UAB111 enhanced ATRA signaling in human organotypic epithelium at a 50-fold lower concentration than UAB30. This was consistent with the 2- to 5- fold greater increase in ATRA in skin rafts treated with UAB110/111 *versus* UAB30. Furthermore, at 0.2 μM, UAB110/111 increased the expression of ATRA genes up to 16-fold stronger than Targretin. The less toxic and more potent UAB110 also induced more changes in differential gene expression than Targretin. The hydrogen deuterium exchange mass spectrometry analysis showed that both ligands reduced the dynamics of the ligand-binding pocket but also induced unique dynamic responses that were indicative of higher affinity binding relative to UAB30, especially for Helix 3. UAB110 binding also showed increased dynamics towards the dimer interface through the Helix 8 and Helix 9 regions. These data suggest that UAB110 and UAB111 are potent activators of RAR-RXR signaling pathways but accomplish activation through different molecular responses to ligand binding.

INTRODUCTION

Nuclear Receptors (NR) are ligand-activated transcription factors that are key targets for drug discovery and development due to their capabilities to directly modulate gene expression (1-4). There are 48 NRs and approximately half of them require heterodimerization with retinoid X receptor (RXR) to perform their function (2, 5).

The partners of RXR can be classified as permissive (PPARs, LXR, and FXR) or conditionally permissive (RAR, TR, VDR) (6-11). RXR heterodimers with permissive partners can be activated by either RXR agonists or its partner's specific ligands, and when both partners are activated, they act in an additive or synergistic manner. In contrast, in conditionally permissive heterodimers, the ligand-dependent transcriptional activity of RXR appears "subordinated" to the binding of the ligand to its partner (12, 13). NRs have a DNA binding domain (DBD) and a ligand binding domain (LBD). The DBD binds to the promoter region of DNA sequences of target genes (14). Rexinoids bind the LBD and induce a significant change in conformation of the domain, often referred to as the transconformation that involves the formation of the ligand binding pocket (LBP) and a surface site for coactivator binding that promotes the recruitment of coactivator proteins. An example of RXR coactivators are the steroid receptor coactivator (SRC) family of coactivators (15, 16). Rexinoids bind in an L-shape geometry to the LBP which consists of helices 3, 5, 7, and 11 (17, 18). The coactivator peptide has a LXXLL motif which interacts with helixes 3, 4, and 12, often referred to as the AF-2 site (19).

Considering that RXRs regulate numerous physiological processes such as differentiation and development, metabolism, apoptosis, and inflammation, RXRs represent a potential therapeutic target in many diseases (20). However, the development

of RXR-selective agonists has been somewhat stifled due to the lack of understanding of the molecular mechanism of rexinoid actions in the cells and the structural basis for rexinoid-mediated modulation of RXR function.

9-cis-Retinoic acid (9cRA) was the first RXR agonist discovered. 9cRA is clinically used for Kaposi Sarcoma but treatment induces severe grade three toxicities due to its pan-agonist activity for both RAR and RXR (21-23). Bexarotene (Targretin) is a rexinoid agonist that targets selectively RXR and is considerably less toxic than 9cRA (24-27). Even though Targretin is selective for RXR, human patients treated with this rexinoid develop hypertriglyceridemia (79%), hypercholesterolemia (48%), and hypothyroidism (40%). Our group designed the RXR-selective rexinoid, UAB30, based on the structure of 9cRA. UAB30 did not stimulate the biosynthesis of serum triglycerides in a rat model due to its low agonist effects in the liver (28-31). UAB30 has been demonstrated to be effective in several model systems of cancer (28, 31).

Our previous study focused on understanding the mechanism of action of UAB30 in a model of organotypic human epithelium (32). We have found that treatment of human organotypic epithelial skin raft cultures with UAB30 resulted in increased levels of all-trans-retinoic acid (ATRA) and upregulation of ATRA target genes. However, UAB30 was significantly less potent as a transcriptional regulator than Targretin, at least in this model. To further improve the potency of UAB30, we identified two next-generation rexinoids, UAB110 and UAB111 (Fig. 1). These rexinoids were found to be effective in preventing breast cancers in an in vivo rat model alone or in combination with tamoxifen (28). Their design was facilitated by use of X-ray crystallography to define the LBP and geometry of the rexinoid bound to RXRα-LBD (33-35). The crystal

structures show that UAB110 and UAB111 fill the ligand pocket well while still preserving the L-shaped geometry that renders the ligand-binding pocket. While crucial for the design process, crystallographic structures are static snapshots of ligand-bound proteins that exist in solution with dynamic molecular motions.

We and others have made use of hydrogen deuterium exchange mass spectrometry (HDX MS) to examine rexinoid-induced structural dynamics in RXR (7, 36-38). Through this technique, we have been able to analyze rexinoid binding sites and binding-associated structural dynamics. We have shown that the binding of UAB30 and Targretin reduces deuterium incorporation and stabilizes peptides in the LBP of the RXRα-LBD (17, 18, 34, 35). Furthermore, our studies showed addition of coactivator LXXLL binding motif peptide further reduces dynamics in the LBP and at the AF-2 site.

Here, to evaluate the biological efficacy of UAB110 and UAB111 relative to Targretin and UAB30, we examined their effects on gene transcription in a model of stratified human epidermis and compared their biophysical properties by HDX MS. Our results suggest that UAB110 and UAB111 are significantly more potent than either UAB30 or Targretin and reveal distinct responses of the RXRα-LBD to the four rexinoids.

RESULTS

The effects of UAB110 and UAB111 on epithelial gene expression

To compare the effects of UAB110 and UAB111 on gene expression with those of previously characterized rexinoids, UAB30 and Targretin, we employed organotypic skin raft culture as a model. Skin raft cultures allow for the monitoring of rexinoid effects

on proliferation and differentiation of the human keratinocytes through morphological changes in the three-dimensional architecture of the epidermis. Our previous results indicated that 2 μM UAB30 induced a visible reduction in the cornified and granular layers of skin rafts consistent with increased ATRA signaling. Therefore, we performed the initial evaluation of UAB110 and UAB111 at 2 μM. However, at this concentration of UAB110 and UAB111, the keratinocytes failed to differentiate and form stratified epithelium (data not shown), suggesting a greater potency of the new rexinoids.

Indeed, reducing the concentration of UAB110 and UAB111 in the skin raft culture medium to 0.2 μM allowed for the growth and differentiation of keratinocytes into spinous, granular, and cornified layers of skin rafts (Fig. 2). Notably, UAB30 at 0.2 μM had little or no effect on proliferation and differentiation of keratinocytes (Fig. 2*C*) compared to rafts treated with DMSO as indicated by hematoxylin and eosin (H&E) staining of sectioned rafts (Fig. 2*A*). In contrast, skin rafts treated with UAB110 and UAB111 displayed significantly reduced cornified and granular layers (Figs. 2*E* and 2*F*), resembling the morphology of skin rafts treated with 10 μM UAB30 (Fig. 2*D*). Interestingly, at 0.2 μM, Targretin appeared to be less potent in triggering the changes in morphology than either UAB110 or UAB111 (Fig. 2B).

Our previous study indicated that treatment with UAB30 enhanced the expression of genes regulated by ATRA (32). To determine whether UAB110 and UAB111 targeted the same genes, we examined the gene expression pattern in skin rafts by qPCR (Fig. 3 and S1). The series of targets included genes involved in ATRA biosynthesis, several known RAR- and RXR-regulated genes, as well as known markers of keratinocyte differentiation (*FLG*, *SPINK5*, *ACER*, *TGM2*). Treatment with 0.2 μM UAB110 and

UAB111 resulted in strong upregulation of ATRA-sensitive genes *LRAT*, *DHRS3*, *DHRS9*, *RARγ*, *STRA6*, and *GABRP*. Transcripts that have been previously reported as downregulated by ATRA (*FLG*, *RDHE2*) were also significantly downregulated after treatment with UAB110 and UAB111. Importantly, the effects elicited by UAB110 and UAB111 at 0.2 μM were comparable to the effects produced by UAB30 at 2 μM. Thus, the next generation rexinoids were at least ~10-fold more potent in regulating gene expression than UAB30 and several-fold more potent than Targretin.

RXR heterodimers control the expression of numerous other genes in addition to those regulated by the RXR-RAR pathway. To obtain a more global picture of the gene expression changes induced by rexinoids in skin rafts, we performed RNA-sequencing analysis (Fig. 4). These experiments focused on comparing the effects of UAB30 and Targretin to those of UAB110. Rexinoid UAB110 was shown to act as a full and potent RXR agonist in the HEK293T cell line (33), yet the increase in serum triglycerides in rats treated by UAB110 was very similar to the low toxicity UAB30. In contrast, while UAB111 was an even more potent agonist than UAB110, its administration to rats raised triglycerides levels by 280% or more over controls. Since UAB111 did not appear as a viable drug candidate, it was not included in the RNA-seq study.

The gene expression profile was compared for rafts treated with 0.2 μM UAB30, Targretin, and UAB110. Due to the lower potency of UAB30 rafts treated with 1 μM UAB30, was also included as a reference point. As suggested by the lack of changes in skin rafts' morphology, treatment with 0.2 μM UAB30 induced a significant change in expression of only one gene, *MAL*, encoding an integral membrane protein implicated in the apical transport of proteins in polarized epithelial cells.

UAB110 had the most significant impact on gene expression in skin rafts, upregulating 2311 genes and downregulating 2105 genes (CPM > 5, FDR < 0.05, FC > 1.5) (Fig. 4*C*). The top upregulated genes were *MUC21* and *GABRP* and the gene downregulated the most was *TGM3*. The expression of 2618 genes was uniquely affected by treatment with UAB110.

In comparison, Targretin treatment affected significantly fewer genes, upregulating 439 genes and downregulating 404 genes (CPM > 5, FDR < 0.05, FC > 1.5). *MUC21* was the gene in the top upregulated genes and the greatest downregulated genes were *TGM3* and *TGM2*. Also, significantly fewer genes (152) were uniquely affected by treatment with Targretin (Fig. 4*B*).

At 1 μM, UAB30 was the weakest agonist, upregulating 340 genes and downregulating 619 genes (CPM > 5, FDR < 0.05, FC > 1.5) (Fig. 4*A*). *LRAT* was one of the top upregulated genes and the gene downregulated the strongest was *TGM3*. Changes in 235 genes were unique to the UAB30 treatment.

Interestingly, 184 genes were affected by all three rexinoids. Pathway analysis performed against Reactome version 78 showed that, in agreement with profound changes in the morphology of skin rafts, the common genes affected were those involved in the formation of the cornified envelope and keratinization, developmental processes, activation of matrix metalloproteases, and extracellular matrix organization.

There were also notable differences in the pathways altered by individual rexinoids. While 1 μM UAB30 primarily altered the expression of the cornified envelope genes, 0.2 μM UAB110 and Targretin also had strong effects on endosomal/vacuolar pathway,

antigen presentation, and interferon α/β signaling, with cornified envelope pathway only in the fourth position and seventh position, respectively, based on the *p* values.

Signaling through other RXR partners was also somewhat altered. Among the targets of the RXR-LXR pathway, the *ABCG1* gene, which regulates cholesterol transportation and cellular lipid homeostasis, was down in rafts treated by UAB30 and UAB110, but it was up in rafts treated with Targretin. Similarly, the RXR-PPAR target gene *ACER1*, encoding a ceramidase, was down after treatment with UAB30 and UAB110, but up after treatment with Targretin. Thus, RNA-seq analysis provided a valuable insight into the similarities and differences in the actions of rexinoids at the level of gene transcription.

Detection of ATRA in skin rafts

Our previous study indicated that treatment with UAB30 raised the steady-state levels of ATRA in skin rafts (32). Since the expression of ATRA-regulated genes was altered in skin rafts treated with UAB110 and UAB111, we asked whether the levels of ATRA were increased in these rafts. Skin raft cultures were treated with 0.2 μM UAB110 and UAB111 and with 2 μM UAB30, for comparison. ATRA levels were determined using multiple reaction monitoring (MRM) mass spectrometry, using a parent ion peak of 301 *m/z* and a daughter ion of 123 *m/z*. Each sample was injected three times and a calibration curve was used to measure the concentration (Fig. 5).

The basal levels of ATRA in vehicle-treated rafts were 3.33 ± 0.62 pmol/g tissue. In the 2 μM UAB30-treated rafts, the concentration of ATRA rose to 6.57 ± 0.88 pmol/g tissue. In the 0.2 μM UAB110-treated rafts the concentration of ATRA nearly tripled to

10.45 ± 2.28 pmol/g of tissue. And the skin rafts treated with 0.2 μM UAB111 showed the highest levels of ATRA at 13.72 ± 3.88 pmol/g tissue. These results were consistent with the increasingly disordered appearance of skin rafts treated with UAB30 < UAB110 < UAB111 and with the increasing amplitude of changes in expression of ATRA-regulated genes. The levels of all-trans-retinol were decreased in skin rafts treated with UAB110 and UAB111, possibly due to enhanced conversion of retinol to ATRA (Fig. 5*B*). Retinyl ester content was similar in all treated and untreated rafts (Fig. 5*C*) despite the increase in the expression of *LRAT* in rexinoid-treated rafts. This could be due to the lower availability of retinol for esterification because of the increased demand for retinol for ATRA biosynthesis. Thus, the direct measurements of retinoids in skin rafts provided evidence that similarly to UAB30, UAB110 and UAB111 raise the cellular levels of ATRA.

HDX-MS analysis of rexinoids bound to the RXRa-LBD homodimer

To examine the structural and dynamical effects of rexinoid binding to its receptor we performed differential HDX MS where RXRα-LBD homodimer with no ligand bound (apo) was used as a reference. In-line pepsin digestions of RXRα-LBD and LC-MS analysis reliably yields 78 peptides that cover 97% of the primary sequence (Fig. S2 and S3). The deuterium uptake results are displayed as a difference map in Figure 6. A negative value in deuterium uptake represented a decrease in solvent accessibility and hydrogen bonding (less dynamic/ more protection) in a given region of the LBD when bound to rexinoid as compared to apo. A positive value represented an increase in

exchange (more dynamic/ less protection). A significant change in deuterium uptake was ±0.5 deuterium (Fig. S5).

The RXRα-LBD with rexinoid bound displayed overall reduced dynamics in regions that are part of the ligand-binding pocket (LBP), as we have previously shown (Fig. 6, shades of blue) (18). The LBP involves regions from H3, H5, β-sheet, H7, and H11. These same regions showed the greatest difference between the four rexinoids (Fig. 6, Fig. 7*A*, and Fig. S6). The binding of UAB111 caused the greatest reduction in dynamics for the LBP peptides in the H3, the H5/β1 region, and to a lesser extent H11 (Fig. 6, dark shades of blue). For UAB110 binding, the H3 region had reduced dynamics for all time points but to a lesser extent than UAB111. In contrast, upon UAB30 or Targretin binding, only the early time points displayed lowered dynamics. For the H5/β1 peptides, UAB111 binding to RXRα-LBD reduced dynamics in this region across all time points, whereas the other three rexinoids only displayed protection in the later time points. The difference in the H11 region between rexinoids was more gradual moving from less protection to more protection with UAB30, Targretin, UAB110, and then UAB111.

Beyond the LPB, there were two regions of the RXRα-LBD that displayed increased dynamics for UAB110 and Targretin (Fig. 6, shades of red). These were the C-terminal portion of H3 and the H8/H9 region including the loop between the two helices. RXR in complex with UAB30 or UAB111 did not induce significant changes in deuterium incorporation for these regions (Fig. S7).

The rate of exchange was examined within the HDX MS data of the RXRα-LBD. We observed both regimes of exchange kinetics (EX1 and EX2) within our data. The

majority of our HDX MS data on RXRα-LBD displayed EX2 kinetics (Fig. S8). Within EX2 kinetics, the exchange regimes reflect small and fast local structural fluctuations and was observed through a gradual shift in the peptide isotopic distribution (39). An example of EX2 kinetics was displayed in Figure 7*B* in the first column and in Figure S8.

In EX1 kinetics, the rate of exchange reflects a different unfolding pattern that was identified in the H3 peptide, A_{271}ADKQFTL$_{279}$ (Fig. 7*B*) (40, 41). The EX1 on-exchange kinetics for H3 was manifested through two populations of isotopic distributions in several of the on-exchange time points (Fig. 7*B*, second, third, and fourth columns). The first population had not undergone exchange and the second population had undergone exchange. For EX1 kinetics the closing rate is slow relative to the chemical exchange rate. The two populations of isotopic distributions (bi-modal distributions) were observed for RXRα-LBD bound to Targretin, UAB110, and UAB111. For either UAB110 or UAB111 in complex with RXRα-LBD, the bimodal distribution was seen until 3600s. Targretin only displayed a bi-modal distribution at 15s. By 3600s, each rexinoid bound to RXRα-LBD showed a single population of fully exchanged H3 peptides. Interestingly, H3 is the only region directly involved in both the LBP and in the formation of the coactivator binding site. Given that RXR-UAB110 and RXR-UAB111 complexes had bi-modal distributions with the largest portion displaying the slower exchange rate, it implies that UAB110 and UAB111 had higher affinity binding but also that H3 is making significant conformational changes upon ligand binding.

Based on this range in deuterium exchange for H3, we examined its correlation with the measured binding affinities for the various rexinoids. We have previously made use of differential scanning calorimetry (DSC) to determine the extent of thermo-

stabilization caused by agonist binding at both physiological and elevated temperatures (42). UAB110 and UAB111 have been shown to stabilize the RXRα-LBD homodimer more significantly than UAB30 with differences in free energy of stabilization (ΔΔG) reaching 7-8 kJ/mol. In addition, the increase in thermal unfolding temperature (ΔT_m) of the holo-homodimers bound with different agonists, with regard to the apo-homodimer, is directly proportional to the ΔΔG values.

Here, we measured the unfolding T_m of RXRα-LBD bound with Targretin by DSC and directly compared it with the T_m values of those bound with the UAB rexinoids (Fig. S4*A*). Subsequently, we looked for a correlation with the H3 peptide deuterium uptake to see if the H3 region served as a leading indicator of binding affinity. When plotted (Fig. S4*B*) a trend between the decrease in number of deuterium incorporations by H3 and the increase in ΔT_m is observed. Such correlation has been noted for other proteins (43). Overall, this analysis further confirmed the significant role of H3 in binding of rexinoids.

HDX-MS analysis of rexinoids + GRIP-1 coactivator bound to the RXRa-LBD homodimer

In our previous analysis of UAB30 and Targretin we also analyzed the RXRα-LBD by HDX MS in the presence of rexinoid and a coactivator peptide, GRIP-1. The GRIP-1 binding site is comprised of H3, H4 and H12. This work helped in the correlation between the observed dynamics and the existing X-ray crystallography structures. Thus, we performed similar HDX MS experiments with the ternary complex of RXRα-LBD-rexinoids-GRIP-1 with the two potent rexinoids, UAB110 and UAB111. The ternary

complexes displayed reduced dynamics in the coactivator binding site (Fig. 8). Compared to the HDX MS analysis of the RXRα-LBD-UAB110 or UAB111 complexes, GRIP-1 binding resulted in further suppressions in deuterium incorporation for regions involved in the LBP (Fig. 8).

These results mimicked what we saw in our previous analysis where GRIP-1 binding significantly stabilized the RXRα-LBD into the active conformation. Interestingly, the increased dynamics observed for the C-terminal end of H3 and the H8/H9 plus loop region when UAB110 alone was bound to the homodimer were not observed when GRIP-1 was added to the complex (Fig. 8*B* and 8*C*). While the addition of GRIP-1 provides context for comparison of HDX MS results to existing X-ray crystal structures, the rexinoid distinguishing characteristics were best observed in complexes that did not include the coactivator peptide.

Evaluating the positive RXRα-LBD dynamics and homodimer interface for the bound rexinoids

Based on the differences observed in the HDX MS profiles for each rexinoid bound to RXRα-LBD, we mapped the HDX MS deuterium incorporation results onto the X-ray crystal structures of RXRα-LBD homodimers in complex with UAB110 (PDBid: 4RMD) and UAB111 (PDBid: 4RME) (Fig. 8, and Fig. S11). Interestingly, the results for UAB110 and Targretin showed reduced dynamics (shades of blue) of H3 near the ligand and increased dynamics (shades of red) in the C-terminal portion of H3. The increased dynamics also occurs in the adjacent H8 region and then the loop to H9 region. By mapping the HDX MS results onto the X-ray crystal structures we observed a connecting

allosteric path of increased RXRα-LBD dynamics when UAB110 or Targretin were bound that seemed to move towards the homodimer interface. Correspondingly, the lack of these positive dynamics for UAB111 and UAB30 created a stark contrast. When the HDX MS results for the ternary complexes (RXRα-LBD-rexinoid-GRIP-1) are mapped onto the RXRα-LBD homodimer structures, the lack of positive dynamics is again noticeable. Given that the X-ray crystal structures of RXRα-LBD in complex with rexinoid alone have not been solved, our HDX MS results allowed for the understanding of both rexinoid and coactivator induced structural dynamics in a step-wise fashion.

Based on these observations, we then evaluated the dimer interface of all four RXRα-LBD-rexinoid-GRIP-1 X-ray structures by use of the Proteins, Interfaces, Structures, and Assemblies (PISA) server (44). Through this analysis, we identified RXRα-LBD homodimer interface contacts that are distinct when UAB111 and Targretin are bound (Fig. S10). Specifically, Lys^{417} in H10 forms a salt bridge with Glu^{390} in H9 of the opposite monomer when UAB111 is bound. There is a second salt bridge that is formed between Lys^{417} in H10 and Glu^{394} in H9 of the opposite monomer. There is one unique Targretin induced interaction between Lys^{405} in Helix 9 and Glu^{401} in H9 that is not seen in the other ligands. The unique and common interactions in the various homodimer interfaces identified by the PISA algorithm are listed in Figure S10. This evaluation of the ternary complex X-ray crystal structures indicated that the rexinoids may induce unique dimer interface interactions even in the presence of a GRIP-1 coactivator.

Overall, both our biological and biophysical analyses demonstrated that UAB110 and UAB111 are more potent agonists of RXR than either UAB30 or Targretin. Based on

the skin raft cultures and qPCR results, the potency of each of these rexinoids is unique with UAB111 increasing the expression of ATRA related genes the most and in many ways demonstrating the toxicity that was observed in previous studies (33). Both UAB110 and UAB111 significantly increased steady state levels of ATRA in the organotypic raft cultures at 10-fold lower concentrations than those observed for UAB30 in our previous studies (32). Finally, the biophysical analysis further confirms that binding of UAB110 or UAB111 to the RXRα-LBD produced agonist-like binding dynamics as observed by HDX MS. UAB111 binding induced the largest reduction in dynamics that indicated a very stable RXRα-LBD ligand binding pocket and again correlating with its toxicity. While UAB110 binding also induced a stable binding pocket, it also induced unique patterns of RXRα-LBD dynamics that distinguished it from UAB111. The potency of each of these novel rexinoids was higher than both UAB30 and Targretin. These studies demonstrated that the potencies of each of these rexinoids were distinct and likely followed unique RXR activation mechanisms with UAB111 being too toxic for therapeutic use. This leaves UAB110 as a uniquely potent rexinoid that does not induce toxicity and thus merits further investigations as a viable cancer therapeutic agent.

DISCUSSION

RXR agonists can have pleiotropic effects on gene transcription due to the role of RXR in heterodimerization with several nuclear transcription factors (45). Still, RXR remains a target for drug development based on the potential for elucidating selective RXR transcriptional response in certain tissues and different disease states such as cancer (3, 4, 20, 28). This study makes use of both an in vitro model of human epidermis and

biophysical analysis to demonstrate the higher potency of two RXR-selective agonists, UAB110 and UAB111. We identify similarities and differences in (1) how these two rexinoids influence RXR ligand-mediated signaling in terms of activation of ATRA-related transcriptional profiles in the human epidermis and (2) how they influence the structural dynamics of the RXRα ligand binding domain as observed in the differential HDX MS analysis.

In our current work at just 0.2 μM concentration both UAB110 and UAB111 triggered changes in the epidermal stratification pattern similar to those observed in skin rafts treated with 10 μM UAB30. The differences observed in the histology of skin rafts treated with rexinoids correlated to the gene activation levels and steady state levels of ATRA. Previously, we proposed that UAB30 would raise ATRA levels in a two-step mechanism. First, UAB30 potentiates the transcriptional activity of existing cellular ATRA bound to RXR-RAR heterodimers. This upregulates the ATRA-sensitive genes which include *STRA6* (46) and *LRAT* (47) required for the uptake and retention of retinol. Then, the increased influx of retinol promotes the biosynthesis of ATRA and increase in its cellular levels, leading to further upregulation of RXR-RAR signaling.

It is well known that vitamin A deficiency leads to an increased development of spontaneous and chemically induced tumors (48), whereas dietary vitamin A supplementation appears to decrease chemically induced tumor incidence. ATRA prevents tumor development by inhibiting proliferation (49-51), stimulating differentiation (52), inducing apoptosis (53, 54) or combinations of these mechanisms. We have shown that the expression of ATRA sensitive genes is altered in UVB irradiated mouse skin and in mouse models of UVB-induced basal cell carcinoma and squamous

cell carcinoma, suggesting that exposure to UVB lowers the levels of bioactive ATRA (32). The reduced ATRA signaling can be rescued by ATRA supplementation. Currently, ATRA is used in combination with other chemotherapeutic agents for the treatment of Acute Promyelocytic Leukemia (APL) in adults and of Neuroblastoma (NB) in children (55). Limitations in ATRAs therapeutic potential include rapid first-pass metabolism and poor aqueous solubility (56). One way around these limitations is to induce physiological ATRA biosynthesis through treatment with UAB rexinoids. As shown in the present study, at 0.2 μM concentrations, UAB110 and UAB111 significantly upregulated the expression of *STRA6* and *LRAT* resulting in 3-4 fold increase in ATRA concentrations. The high potency and low toxicity of UAB110 make it an attractive chemopreventive agent that could be used at much lower doses than UAB30 to raise ATRA levels in conditions and disease states known for reduced ATRA signaling.

A major challenge in drug development for nuclear receptors is the lack of understanding of how structurally similar agonists induce overall protein structural changes that produce different biological outcomes and enhanced degrees of potency. For rexinoids that bind RXR, the small molecule design challenge is further complicated due to their similarly bound L-shaped geometry profiles within the ligand binding pocket. X-ray crystal structures have provided details of these dimensions, but these structures do not reveal dynamic responses that we have shown to be important both in ligand binding and in coactivator recruitment (17, 18, 42). In the crystal structures of RXR bound to these rexinoids there were no significant differences in the overall structure of the LBD, however through HDX MS we observed how ligand binding induced rexinoid-specific dynamics in the RXRα-LBD.

The HDX MS data clearly demonstrated these potent rexinoids are specifically binding in the RXRα-LBD ligand binding pocket by reducing deuterium uptake in the regions that form the pocket (H3, H5, β1, H7, and H11) and not others (Fig. 6). The HDX MS data also revealed that between the four rexinoids, UAB110 and UAB111 protect the LBP structural elements from deuterium uptake to a larger extent compared to UAB30 and Targretin. This observed increased protection correlates well with their binding affinities and thermodynamic properties we have previously reported (33). This high affinity binding forms a stable binding pocket that then promotes the active conformation of RXRα-LBD more so than UAB30 and Targretin.

The HDX MS data allowed for the determination of where the higher affinity binding was occurring within the RXRα-LBD. The dynamics of H3 were reduced significantly more for RXRα-LBD in complex with UAB110 or UAB111 than UAB30 or Targretin. For UAB111 binding, this dynamic trend follows for all LBP helices but is most dramatic for H3. The UAB110 in complex RXRα-LBD had a significantly different response of binding compared to UAB111 (Fig. 6). RXR-UAB110 and RXR-Targretin complexes both displayed increased dynamics of the C-terminal end of H3 and the H8/H9 region. When mapped onto the homodimer structure, these positive dynamics appear to move in the direction of the homodimer interface. Similar dynamics profiles in the C-terminal end of H3 and the H8/H9 regions were reported for two LXR agonists bound complexes in a HDX-MS study of 17 different LXR-specific ligands (57). While this effect was not highlighted in the study, our RXRα-LBD-UAB110 biophysical data provide corroborating evidence that this can be a known response to some but not all ligands for nuclear receptors.

Upon addition of GRIP-1 coactivator peptide, the HDX MS profiles are nearly identical. Our data suggests the differences in RXR response due to UAB110 or UAB111 binding are occurring prior to coactivator binding. Based on previous reports of the toxicity of UAB111 and our current results from our in vitro organotypic skin raft cultures (morphology, qPCR, and RNAseq), we could interpret the biophysical HDX MS results for UAB111 binding as demonstrating what a full RXRα agonist profile would look like or even simulating some form of ligand-induced hyper-activation of RXR mediated transcription. In fact, it is notable how similar the HDX profiles for RXRα-LBD-UAB111 and the ternary complex of RXRα-LBD-UAB110-GRIP-1 are (Figs. 6 and 8). For UAB111 bound, it is as if the coactivator is already there to lock in the active conformation of RXRα-LBD. Our HDX MS data provides a better explanation for UAB111's toxicity than other forms of biophysical analysis can.

The two distinct RXRα-LBD biophysical responses to potent rexinoids in the context of our in vitro biological data raises questions as to how the observed LBD dynamics manifest in the molecular mechanism of RXR-mediated transcriptional signaling. Specifically, our data demonstrate these potent rexinoids are inducing RAR-RXR mediated transcription and increased steady state levels of ATRA. In the case of UAB110 binding, do the positive RXRα-LBD dynamics in H3 and H8/H9 exert an allosteric influence on the RXR homodimer promoting dissociation for (RAR) heterodimer association? Or do they contribute an allosteric role in RAR heterodimer signaling that would not occur in other RXRα heterodimer complexes? H9 is a significant part of the RXRα-LBD homodimer interface and also a part of the RAR-RXR heterodimer interface (58). Alternatively, given H3's dual role as part of the LBP and the

AF-2 coactivator binding site, could the increased H3 dynamics influence the extent of coactivator binding? Would increased dynamics of the AF-2 site influence full length RXR coactivator binding? GRIP-1 (also known as TIF2) has three LXXLL motifs and has been proposed to have a cooperative binding mechanism that includes the coactivator interacting with both ligand binding domains' AF-2 sites in an RAR-RXR heterodimer (59). In the context of a full-length GRIP-1 coactivator, the increased dynamics of UAB110 bound to RXRα could influence this dual binding. With the range of biological and biophysical responses we have demonstrated with these rexinoids in our model systems, all of these questions could be addressed going forward with focus on heterodimer and coactivator interactions. Our experiments demonstrate a unique combination of tools to understand the molecular mechanisms of differential rexinoid signaling in skin. Importantly, our work demonstrates the potential of UAB110 as a potent non-toxic anticancer agent.

EXPERIMENTAL PROCEDURES

Materials

UAB30, UAB110, and UAB111 were synthesized at the University of Alabama at Birmingham according to previous methods (33). Dr. Clinton Grubbs at UAB provided Targretin. The coactivator, GRIP-1, was synthesized by Thermo Scientific (^{686}KHKILHRLLQDSS^{698}) with a molecular mass of 1574.86 Da. The purity and structures of the rexinoids and coactivator were confirmed by LC-MS and NMR.

Preparation of organotypic skin rafts and treatment with rexinoids

Neonatal foreskins were obtained from the Newborn Nursery of the University of Alabama at Birmingham Hospital in compliance with the University of Alabama at Birmingham Institutional Review Board (IRB) regulations. As determined by the institutional IRB, the use of discarded unidentifiable foreskin tissue met the requirements for an exemption from IRB approval. Epidermal raft cultures were prepared as described previously (60,61). Briefly, primary human keratinocytes (PHKs) were isolated from freshly collected neonatal foreskins and cultured in DermaLife calcium-free medium (Lifeline Cell Technology, Walkersville, MD). PHKs were seeded onto a dermal equivalent consisting of collagen with embedded Swiss 3T3 J2 fibroblasts. After 3 days, skin equivalents were lifted onto stainless steel grids and cultured at the medium-air interface using raft culture medium prepared from Dulbecco's modified Eagle's medium, Ham's F12 medium, and 10% fetal bovine serum (Atlanta Biologicals, Atlanta, GA), which was supplemented with cholera toxin, insulin, apo-transferrin, hydrocortisone-21, and human epidermal growth factor as described previously (60,61). The raft culture medium was supplemented with rexinoids at specified concentrations from DMSO stocks, beginning from the day the skin equivalents were lifted onto the grids until harvest. The raft cultures were allowed to stratify and differentiate for 11 days, whereupon they were harvested for analysis.

H&E Staining

The rafts were fixed in 10% buffered formalin for 45 minutes and embedded in paraffin. Paraffin-embedded skin rafts were cut into 5-μm sections, mounted on

Superfrost/Plus slides (Fisher Scientific, Pittsburgh, PA). Sections were deparaffinized and rehydrated by a series of washes in decreasing concentrations of ethanol (95, 85, 70, 50, and 30 %), processed for Harris hematoxylin (Fisher Scientific, Pittsburgh, PA) and eosin (Fisher Scientific, Pittsburgh, PA) and mounted with Permount (Fisher Scientific, Pittsburgh, PA). All sections were analyzed using an AxioImager A2 microscope equipped with an AxioCam camera and AxioVision image capture software (Carl Zeiss MicroImaging, Inc., Thornwood, NY).

Quantitative Analysis of Gene Expression

Each rexinoid treatment group included three rafts. Gene expression in skin rafts was analyzed by qPCR. RNA from mouse tissues was extracted with TRIzol (Life Technologies, Carlsbad, CA), treated with DNase I (Promega, Madison, WI), and re-extracted with TRIzol according to the manufacturer's protocols. Two μg of RNA was reverse-transcribed in 20 μl reactions using the Superscript III kit (Life Technologies, Carlsbad, CA). Real-time PCR was performed in duplicates for each sample in a LightCycler® 480 instrument (Roche Diagnostics, Indianapolis, IN) using LightCycler® 480 SYBR Green I Master Mix (Roche Applied Science, Indianapolis, IN) with 0.5 μm primers and 2.5 μl of 5- or 15-fold dilution of reverse transcription reactions in the final volume of 10 μl. Levels of transcripts were determined using a relative quantification method (62) and normalized to the geometric mean of transcript levels of three reference genes (β-Actin, Gapdh, and Hprt and Ppia). Sequences of the primers are available by request. PCR without cDNA templates did not produce significant amplification products. The specificity of the primers was verified by amplification of a single PCR

product, which was determined by observing a single dissociation curve from each tissue. The primer sequences are available upon request.

Analysis of endogenous retinoid content

Skin raft samples were frozen upon collection and kept at −80 ºC until assay. Extraction of retinoids was carried out under yellow light and all retinoids were handled with glass syringes and containers during extraction and quantification procedures. For retinoid quantification, one skin raft per replicate was assayed. Skin rafts were homogenized in 0.9% normal saline as described previously prior to extraction (63). A two-step liquid-liquid extraction procedure was used to extract retinoids as described previously in detail (63). Briefly, the first extraction was done by mixing cell or tissue lysates with 1 or 3 ml 0.025 M KOH in ethanol, followed by 5 or 10 ml hexane, respectively. The mixture was vortexed and subjected to centrifugation at 1000×g for 30 s. The hexane phase containing retinol and retinyl esters was transferred to a new tube and put on ice. For the second extraction, the tissue lysates were mixed with 65 or 200 µL 4 M HCl followed by 5 or 10 mL hexane, respectively. The mixture was vortexed and centrifuged at 1000×g for 30 s. The solvent from the second hexane phase containing retinoic acid was transferred to a new tube and put on ice. All samples were then placed under a gentle stream of nitrogen with heating at 30 ºC until dry. Samples were then resuspended in 60 µL acetonitrile, placed in HPLC vials outfitted with low-volume deactivated glass inserts, and stored at −20 ºC until analyzed. As internal standards, each cell or tissue lysate sample was mixed with 2.2 µM all-*trans*-4,4-dimethyl-RA and 0.9 µM retinyl acetate.

ATRA levels were quantified using liquid chromatography-multistage-tandem mass spectrometry using a Shimadzu Prominence UFLC XR liquid chromatography system (Shimadzu, Columbia, MD) coupled to an AB Sciex 6500 QTRAP hybrid triple quadrupole mass spectrometer (AB Sciex, Framingham, MA) using atmospheric pressure chemical ionization (APCI) operated in positive ion mode as described previously in detail. RA quantification was performed in 20 µl samples, and the assay was carried out in the columns maintained at 25 ºC. Data were analyzed using Analyst (AB Sciex, Framingham, MA), and RA content in each sample was normalized to tissue weight. Levels of retinol and RE were quantified by HPLC-UV using a Waters H-Class UPLC system equipped with a photodiode array detector operated in single wavelength detection mode according to previously published methodology (32). HPLC-UV chromatograms were generated at 325 nm, and peaks were measured for retinol at 4.8 min, the internal standard retinyl acetate at 8.9 min, and RE at 16.6 min using Waters Empower Software. Total retinol and RE were normalized to tissue weight.

Protein Expression and Purification

hRXRα-LBD (Thr^{223} – Thr^{462}) was expressed and purified according to Moras and Egea (64) and Xia et al. (17). The expression of the His6-tagged hRXRα-LBD fusion protein was done in BL21 (DE3) Escherichia coli (Invitrogen). The bacteria were grown in Luria broth (LB) medium at 20 °C. 1 mM isopropyl-B-D-thiogalactopyranoside was used to induce protein expression. The cells were first treated with 0.5 M NaCl, 20 mM Tris (pH 8.0), cOmplete™ ULTRA tablets, and DNAse. A French press was used to lyse the cell (1500 p.s.i.) and then centrifuged at 25,000 rpm for 30 min. The His6-tagged

hRXRα-LBD was eluted from a nickel-chelating column (GE Healthcare) using a 10 mM Tris (pH 8.0) buffer containing 500 mM NaCl and 300mM imidazole. The fractions with hRXRα-LBD were then dialyzed in 10 mM Tris buffer (pH 8) containing 2 mM DTT, 0.5 mM EDTA, and 50 mM NaCl. α-thrombin (Novagen, Madison, WI) hydrolyzed the His6-tag at 4°C. The hRXRα-LBD homodimers and tetramers were separated at 4°C using a hiLoad Superdex 75 gel filtration column (SEC, GE Healthcare) with 1.0 mL/min flow rate. MALDI mass spectrometry and SDS-PAGE were used to establish a purity of >97% and mass of the monomers (m/z = 26,433.1 Da). Native PAGE and UV confirmed that the isolated fractions were hRXRα-LBD homodimers and the concentration of the fractions. Samples were then flash frozen and stored at -80 °C.

Differential Scanning Calorimetry

Calorimetry experiments were performed in a VP-Capillary DSC (Malvern Instruments, USA) in 0.130 ml cells at a heating rate of 2 °C/min. An external pressure of 2.0 atm was maintained using a nitrogen tank to prevent possible degassing of the samples on heating.

For the protein, the dimeric peak freshly eluted from SEC was used, and the SEC buffer was used as the matching buffer. In the cases where a ligand was used, a 10 mM stock of the ligand in degassed DMSO was prepared and stored at -80 °C protected from light. Prior to each set of experiments, the ligand stock was diluted in DMSO to 100 times the final desired concentration, and then diluted 100-fold into the protein sample or matching buffer. The samples were incubated at 22 °C for 10-15 minutes and then transferred into the DSC sample loading plate. The sample was stored at 5 °C at least 1 h

prior to the DSC runs depending on their position in the queue. DSC data analysis was carried out using the built-in analysis modules in Origin 7 (OriginLab, LLC., USA) provided by the DSC manufacturer as described (42).

Automated Hydrogen Deuterium Exchange and Data analysis

Solution phase H/D exchange experiments were performed using an automated LEAP Technologies Twin PAL RTC LEAP Technologies, (Carrboro, NC). Experiments were performed as previously described (18). 30 pmol of hRXRα-LBD homodimer was mixed with 10 times the concentration of ligand or vehicle (DMSO) with or without coactivator peptide and incubated at room temperature for one hour (18). The protein mix is then dispensed into a mixing tray where it is then diluted with 54 µL of deuterated buffer (or protonated buffer for control experiments). Following on-exchange time points (20 °C), 50 µL of the sample was aspirated and dispensed into 50 µL of quench buffer (3 M Urea, 1 % TFA, 50 mM TCEP, 2 °C). Samples were taken at 15s, 30s, 60s, 300s, 900s, and 3600s and performed in triplicate. Samples were digested for 120s on an enzymatic Waters pepsin column. Sample loading, digestion, and desalting were driven with a Shimadzu UPLC pump at 100 µL min-1. Peptic peptides were desalted on a Acclaim PepMap C18 trap column (ThermoScientific), followed by an Acquity BEH C18 reverse-phase column (1 mm x 50 mm; Waters. A gradient of 5-90% acetonitrile, 0.1% formic acid over 16 minutes was used to elute the peptides directly into the SYNAPT G2-Si at 100 µL min-1 with a dual electrospray ionization source. Spectra were acquired over the scan range of 300- 1500 m/z.

PLGS program (Waters) was used for peptide selection. Seven MsE runs were collected and peptides that were replicated in five of the seven MsE runs were used for analysis. HDX-MS raw files were processed and visualized by the use of HDExaminer software (Sierra Analytics). In total, 78 peptides representing 96.7% amino acid sequence coverage of the RXRα-LBD. The average length of peptides was 11.2 amino acids with an average redundancy of 3.6. Differential HDX perturbation values were calculated by taking the observed number of deuterium incorporated from ligand binding in the RXRα-LBD-rexinoid at a specific peptide and subtracting it by the number of deuterium incorporated in the apo state from that same peptide, at each of the seven time points. HDX perturbations greater than +/- 0.5 deuteriums were considered significant as described previously (65). Observed RXRα-LBD HDX MS peptides were manually curated across all timepoints to ensure consistent T0 peptide ion identification and subsequent shifting peptide ions as deuterium is incorporated across the timepoints. The deuterium vs. time plots for all RXRα-LBD peptides were visualized in HDExaminer to ensure reproducibility across time points. Each RXRα-LBD complex evaluated was performed at least twice. HDX MS results were then collated into the plots shown in Figures 6 and 8 based off of changes in deuterium incorporation relative to apo- RXRα-LBD. The results were also painted onto existing X-ray crystallographic structures and described in results section.

Data availability

All data are contained with this article and in the supporting information.

Supporting Information

This article contains supporting information

Funding and additional information

This work was supported by the UAB O'Neil Comprehensive Cancer Center, and the National Cancer Institute, NIH grant CA210946. The content is solely the responsibility of the authors and does not necessarily represent the official views of the National Institutes of Health. NM was supported by an NCI diversity supplement to CA210946.

Conflict of interest

The authors declare that they have no conflicts of interest with the contents of this article.

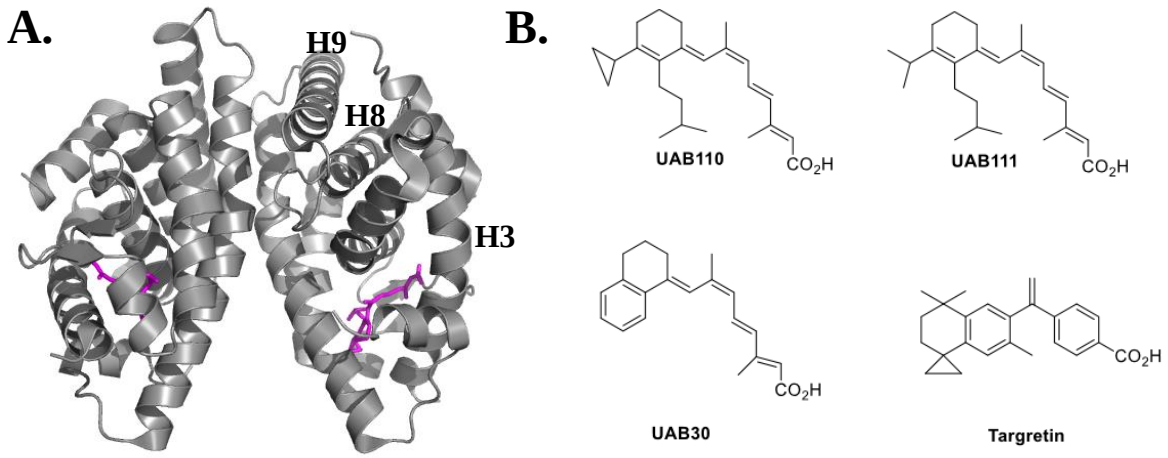

Figure 1. RXR homodimer ligand binding domain (LBD) bound to UAB110. (*A*) Crystal structure of RXR-LBD in complex with UAB110 (magenta) with helices 3, 8, and 9 labeled. (*B*) Structures of rexinoids UAB110, UAB111, UAB30, and Targretin.

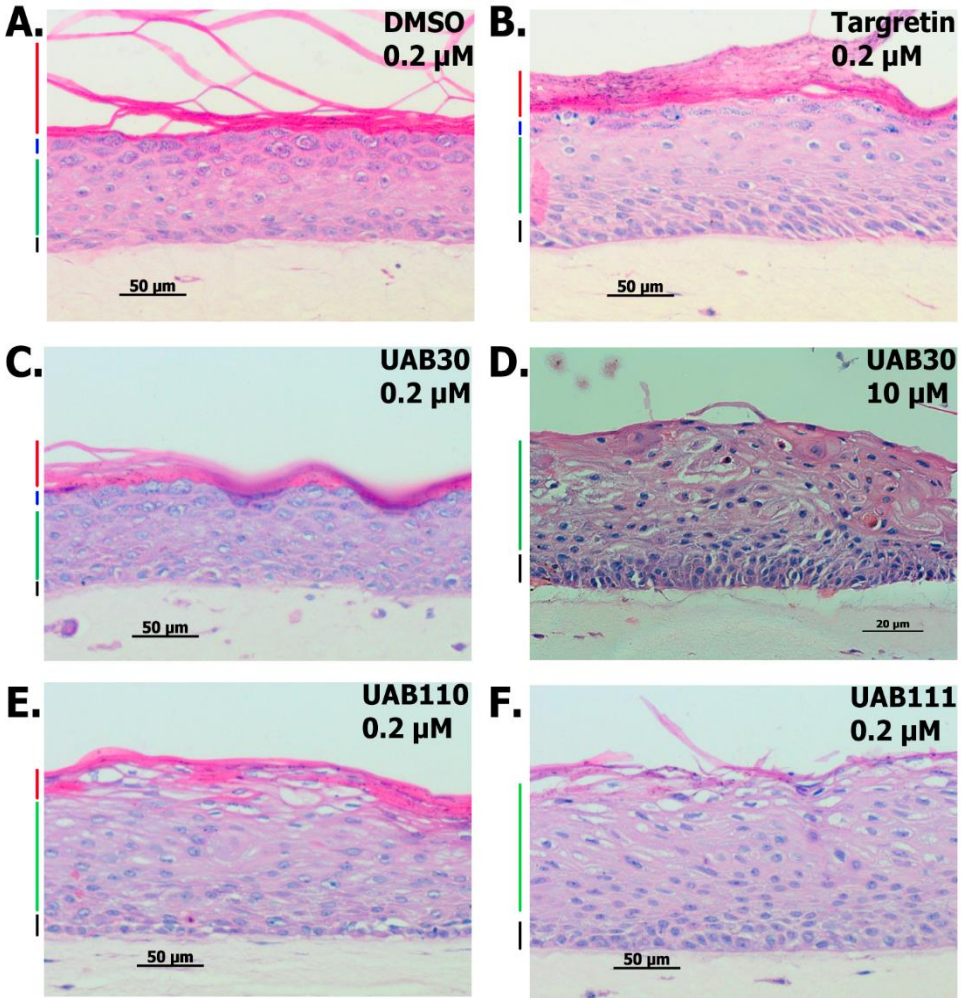

Figure 2. H&E staining of skin raft cultures treated with rexinoid agonists. Human organotypic skin raft cultures were treated with rexinoid agonists: (*B*) 0.2 µM Targretin, (*C*) 0.2 µM UAB30, (*D*) 10 µM UAB30, (*E*) 0.2 µM UAB110, and (*F*) 0.2 µM UAB111. The rexinoids were added to the culture medium at the onset of organotypic skin raft formation and the rafts were allowed to grow for 11 days. Colored lines at the left side of each stain demarcate the layers of the epidermis: cornified (red), granular (blue), spinous (green), and basal (black).

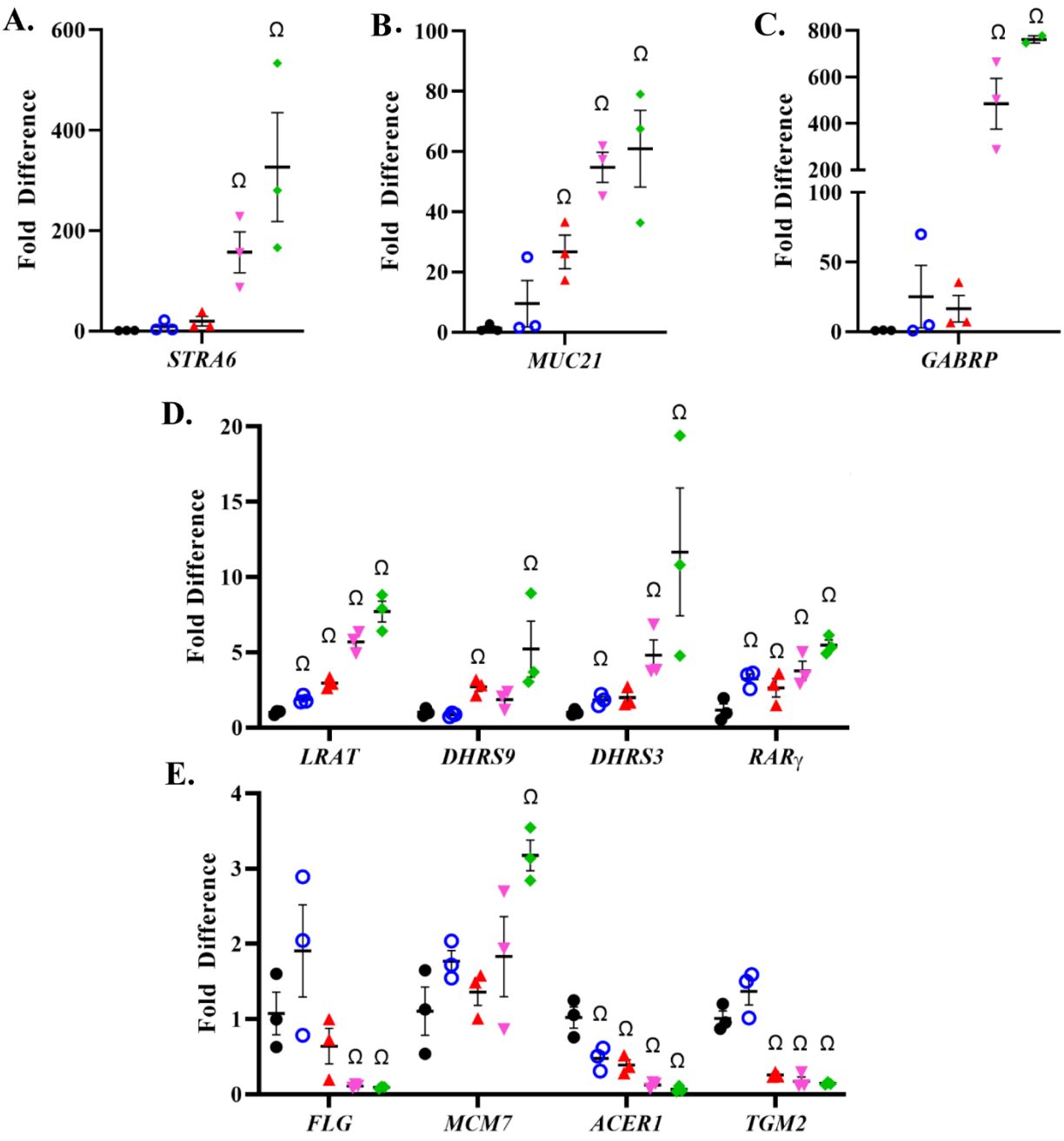

Figure 3. QPCR analysis of gene expression in skin rafts treated with rexinoids. (*A-E*) Quantitative PCR analysis of human skin raft cultures were done in triplicate. Conditions used were as followed: DMSO (black circle), UAB30 (hollow blue circle), Targretin (red triangle), UAB110 (magenta downward triangle), UAB111 (green diamond). (n=3 independent isolations, Ω $p < 0.05$ compared to DMSO control)

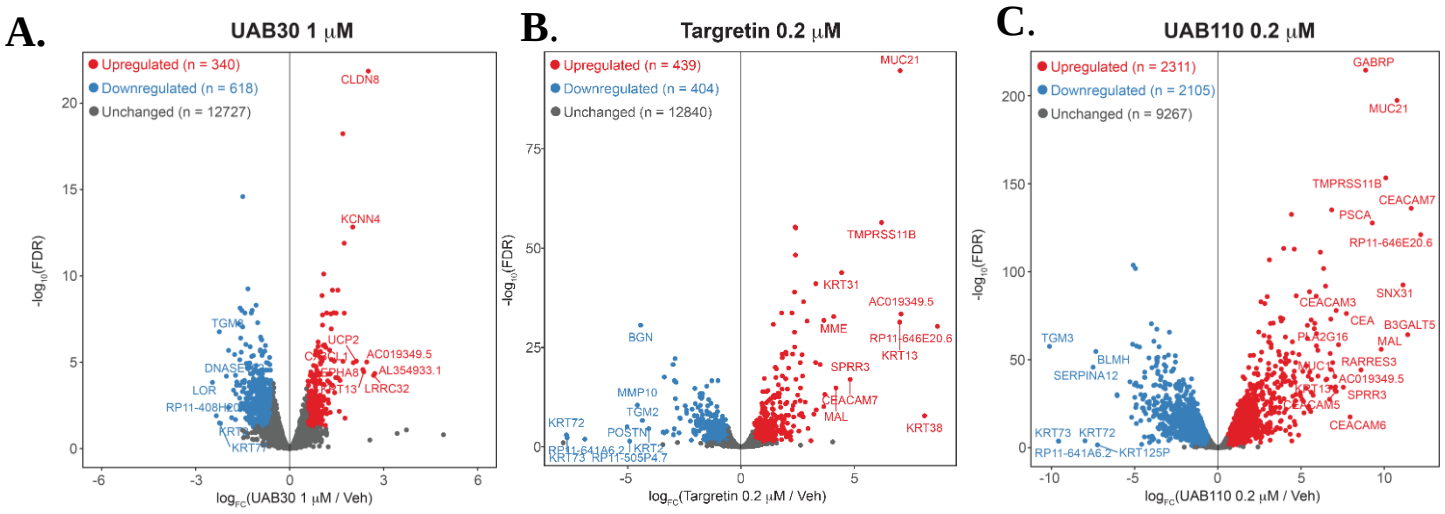

Figure 4. RNA sequencing analysis of skin rafts treated with rexinoids. RNA sequencing analysis of skin raft cultures treated with rexinoids for 11 days. Analysis was formatted into volcano plots detailing genes up and downregulated via rexinoid treatment. (*A*) UAB30, (*B*) Targretin, (*C*) UAB110. (n=4 independent isolations, CPM > 5, FDR < 0.05, FC > 1.5)

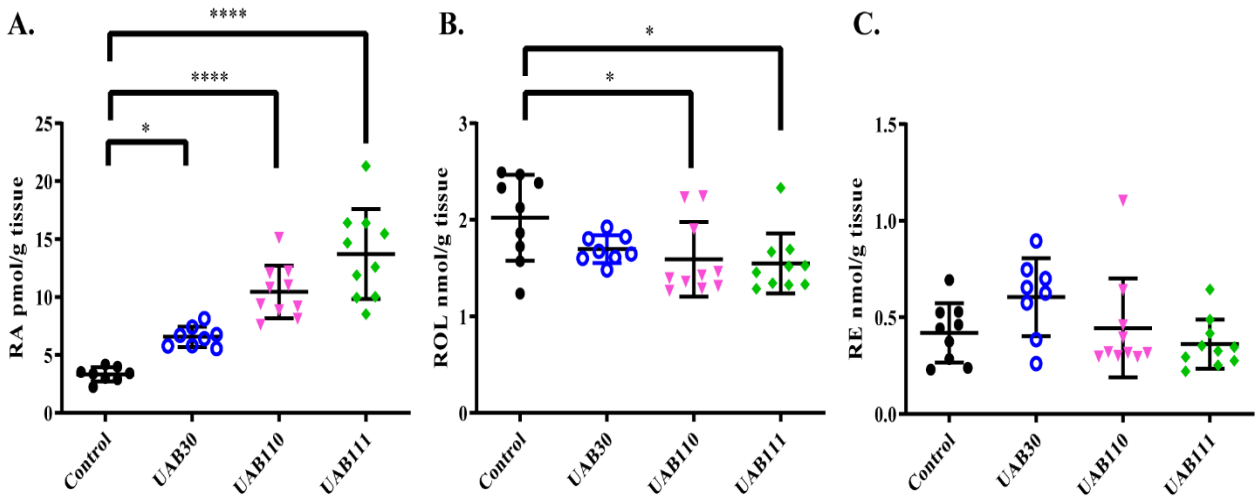

Figure 5. Quantification of retinoic acid, retinol, and retinyl esters. Retinoic acid (RA), retinol (ROL), and retinyl esters (RE) levels were assessed by liquid chromatography with multiple reaction monitoring mass spectrometry. Treatments used were as followed: DMSO (black circle), UAB30 (hollow blue circle), UAB110 (magenta downward triangle), UAB111 (green diamond). Retinyl esters (RE) represent the storage form of retinol (ROL). Retinol is the metabolic precursor of retinoic acid (RA). (*A*)Steady state levels of RA were significantly elevated in skin rafts treated with UAB110 or UAB111. (*B*) Skin rafts treated with UAB110 or UAB111 displayed significant reduction of retinol. *(C*) All three rexinoid treatments did not have significant differences in retinyl esters (RE). (n=8-10, * $p < 0.05$, **** $p < 0.0001$ compared to DMSO control)

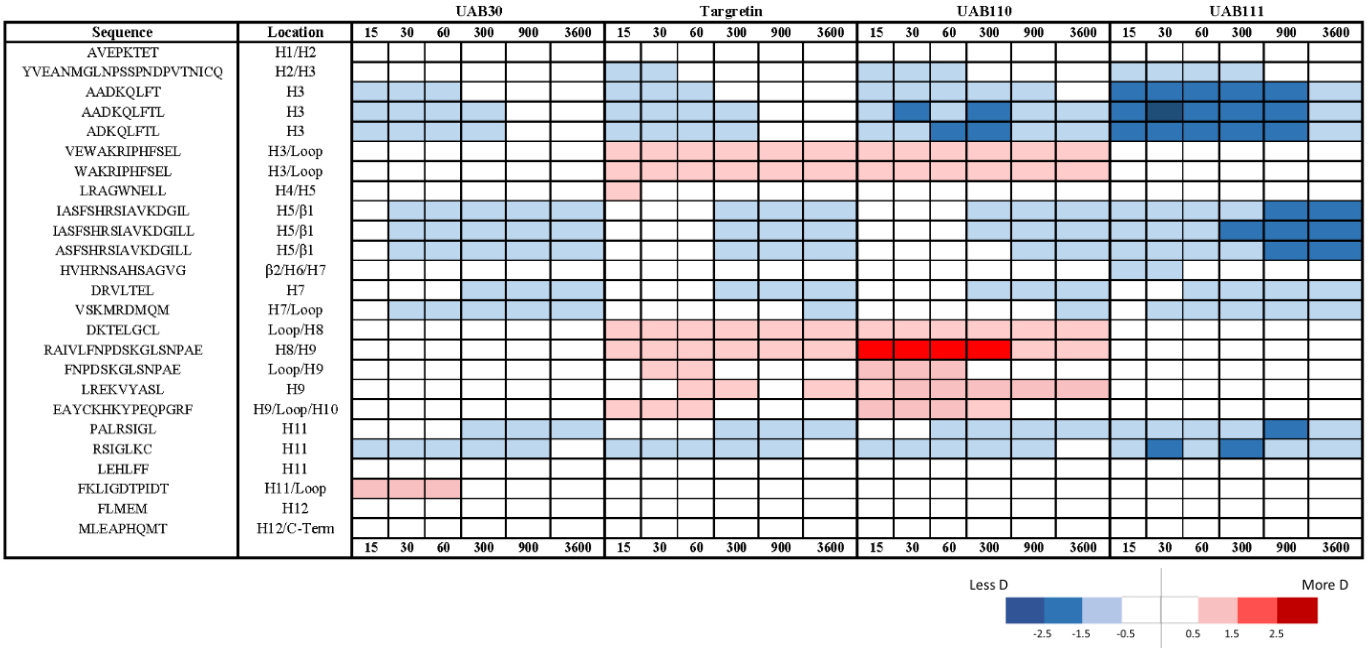

Figure 6. Deuterium incorporation difference maps of RXR*α*-LBD in complex with different rexinoids. HDX-MS analysis of four rexinoids with six on-exchange time points (15, 30, 60, 300, 900, and 3600s) organized into a difference map. Results are reported as an increase (shades of red) or decrease (shades of blue) in deuterium in different regions of the RXR-LBD: rexinoid complex relative to apo-RXR-LBD. All four complexes displayed reduced dynamics in regions of the LBP with UAB111 resulting in the greatest reduction of dynamics in H3. RXR: UAB110 and RXR: Targretin complexes revealed increased dynamics in the C-terminal end of H3, H8, and H9. Significance was established via volcano plots (Fig. S5).

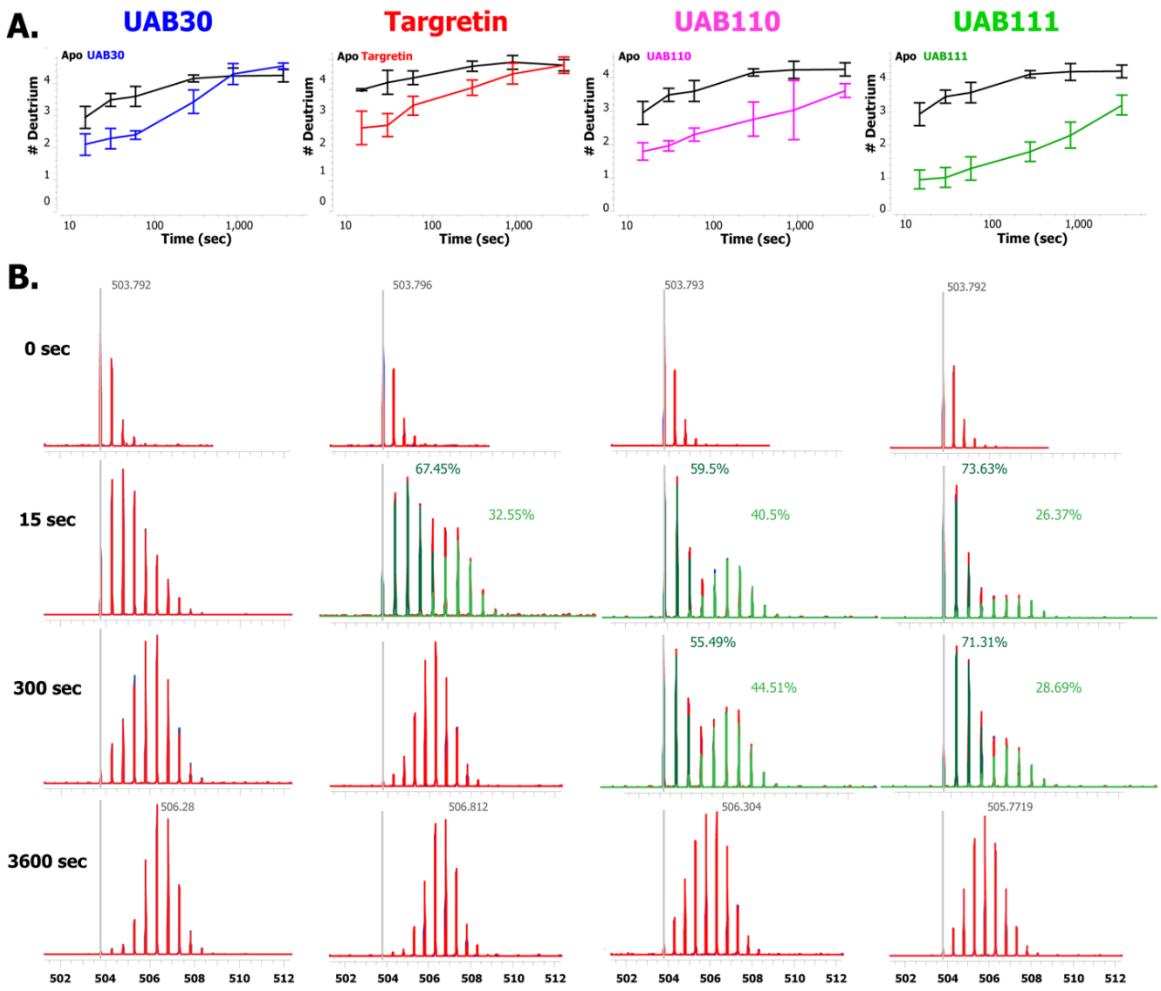

Figure 7. RXRα-LBD ligand binding pocket Helix 3 demonstrates the highest extent of HDX MS variation when bound to different rexinoids. H3 is involved in both the ligand binding pocket and the formation of the AF-2 coactivator binding site. (*A*) Deuterium uptake vs. time for the H3 peptide A_{271}ADKQLFTL$_{279}$ $^{2+}$ when bound to UAB30 (blue), Targretin (red), UAB110 (magenta), and UAB111(green) relative to apo- RXRα-LBD. UAB111 binding lowers the deuterium uptake for this region the most. (*B*) The HDX MS raw spectral data for the H3 peptide for the 0, 15, 300, and 3600 s timepoints. As the deuterium is incorporated over time, the isotopic envelope increases in mass. For UAB30 bound, the population of peptide ions shift higher as a whole. When the other rexinoids are bound, a separation of the H3 peptide ion populations can be seen at the 15s time point that indicates two populations of tightly bound vs. more deuterium accessible forms of the RXR-LBD in this region. This separation in the peptide ion populations is still visible in the UAB110 and UAB111 bound raw data at the 300s time points with both ligands still showing less overall deuterium incorporation at 3600s (broader isotopic envelope). These HDX MS bimodal distributions for UAB110 and UAB111 demonstrate the differential interactions of the various rexinoids with H3 and H3's "sensitivity" to differential ligand binding. Other ligand binding pocket regions of the RXR-LBD do not show this distinction in the data when the various rexinoids are bound. A similar plot of a Helix 7 peptide D_{347} RVLTEL$_{353}$ (1+) (also part of the ligand binding pocket) is provided (Fig. S8).

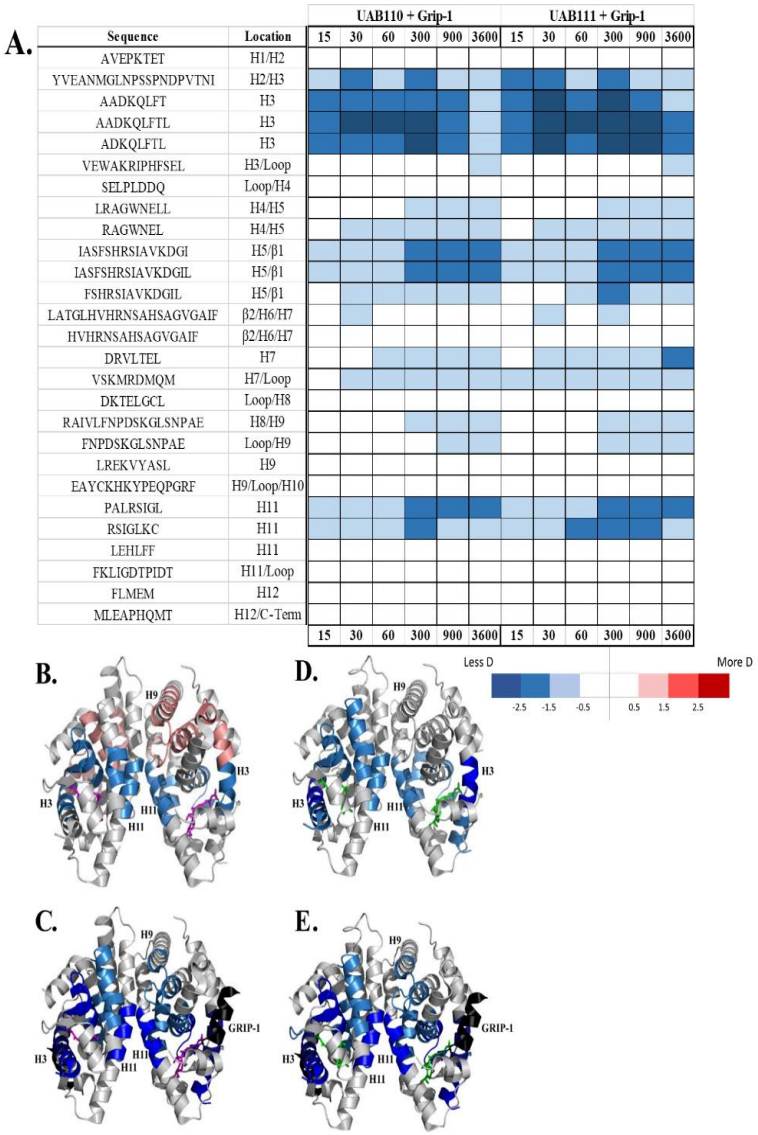

Figure 8. HDX MS analysis of RXR ternary complexes demonstrates potency of UAB110 and UAB111. (*A*) The HDX MS difference map of RXRα-LBD in complex with UAB110 or UAB111 and GRIP-1 coactivator peptide. When the HDX MS results for the two potent rexinoids are painted onto X-ray crytal structures, the patterns of deuterium uptake can be visualized and show how UAB110 binding (*B*, magenta) and UAB111 binding (*D*, green) to RXRα-LBD result in different patterns of dynamics. The regions shaded in blue show the extent of decreased dynamics for regions that are part RXR ligand binding pocket. There are positive dynamics observed in H3 and H8/H9 (shades of red) when UAB110 is bound. When UAB111 alone is bound (*D*) to the RXRα-LBD, the extent of decreased dynamics nearly matches the HDX MS results for the ternary complexes of UAB110 (*C*) or UAB111(*E*) bound plus the GRIP-1 coactivator peptide (black). Each potent rexinoid induces unique in solution dynamics for the RXRα-LBD.

Connecting ligand-induced retinoid X receptor structural dynamics to rexinoid agonist potency

Nathalia Melo[1], Olga V. Beliaeva[1], Welhelm K. Berger[3], Laszlo Halasz[3], Jianshi Yu[4], Nagesh Pilli[4], Zhengrong Yang[1], Alla V. Klyuyeva[1], Craig Elmets[2], Venkatram Atigadda[2], Donald D. Muccio[1], Maureen A. Kane[4], Laszlo Nagy[3], Natalia Y. Kedishvili[1], Matthew B. Renfrow[1]

From the [1]Department of Biochemistry and Molecular Genetics, University of Alabama at Birmingham, Birmingham, AL 35294; [2]Department of Dermatology, University of Alabama at Birmingham, Birmingham, AL 35294; [3]Medicine and Biological Chemistry, Johns Hopkins University School of Medicine, St. Petersburg, FL 33701; [4]Department of Pharmaceutical Sciences, University of Marlyand, Baltimore, MD 21201

Running title: High potency RXR-specific ligands UAB110 and UAB111

*To whom correspondence should be addressed: Matthew Renfrow: [1]Department of Biochemistry and Molecular Genetics, University of Alabama at Birmingham, Birmingham, AL 35294; renfrow@uab.edu; Tel. (205) 937-0546; Natalia Kedishvili: [1]Department of Biochemistry and Molecular Genetics, University of Alabama at Birmingham, Birmingham, AL 35294; nkedishvili@uab.edu; Tel. (205) 532-3738

Supporting Information

Supporting Information S6. Helix 5 and Helix 11 Deuterium Incorporation Plots

Supporting Information S7. Positive Perturbation seen in Deuterium Incorporation Plots

Supporting Information S8. Helix 7 Peptide showing no difference in deuterium incorporation

Supporting Information S9. Difference Maps: UAB30 + GRIP-1

Supporting Information S10. Dimerization Interface interactions

Supporting Information S11. HDX Results mapped on crystal structures

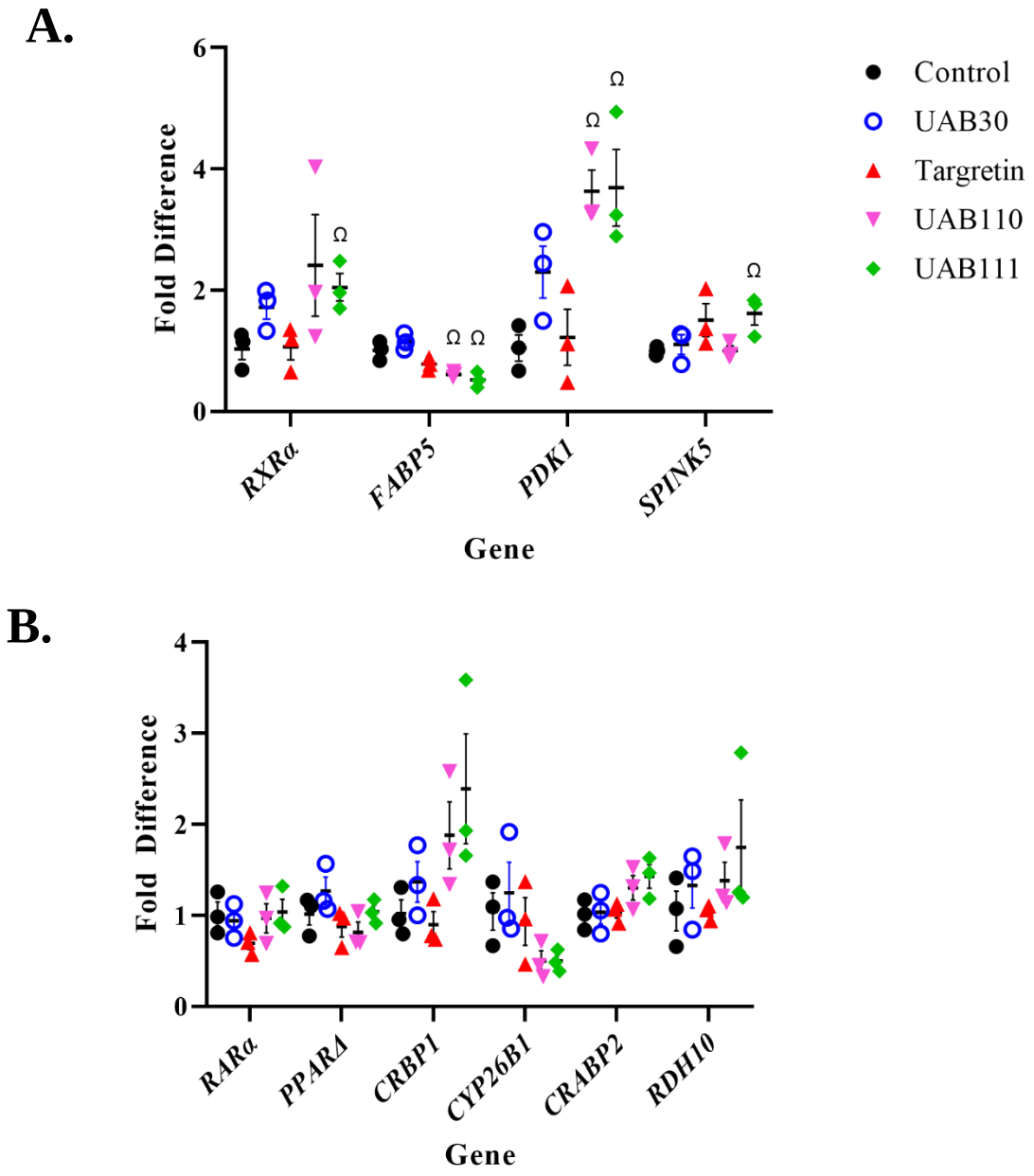

Figure S1. qPCR analysis of skin rafts treated with rexiniods. (*A*, *B*) Quantitative PCR analysis of human skin raft cultures after treatment with rexinoids for 11 days. Rexinoid treatment effects multiple ATRA target genes with UAB110 and UAB111 displaying the strongest effects (*A*) and no significant effects (*B*). (n=3 independent isolations, Ω $p < 0.05$

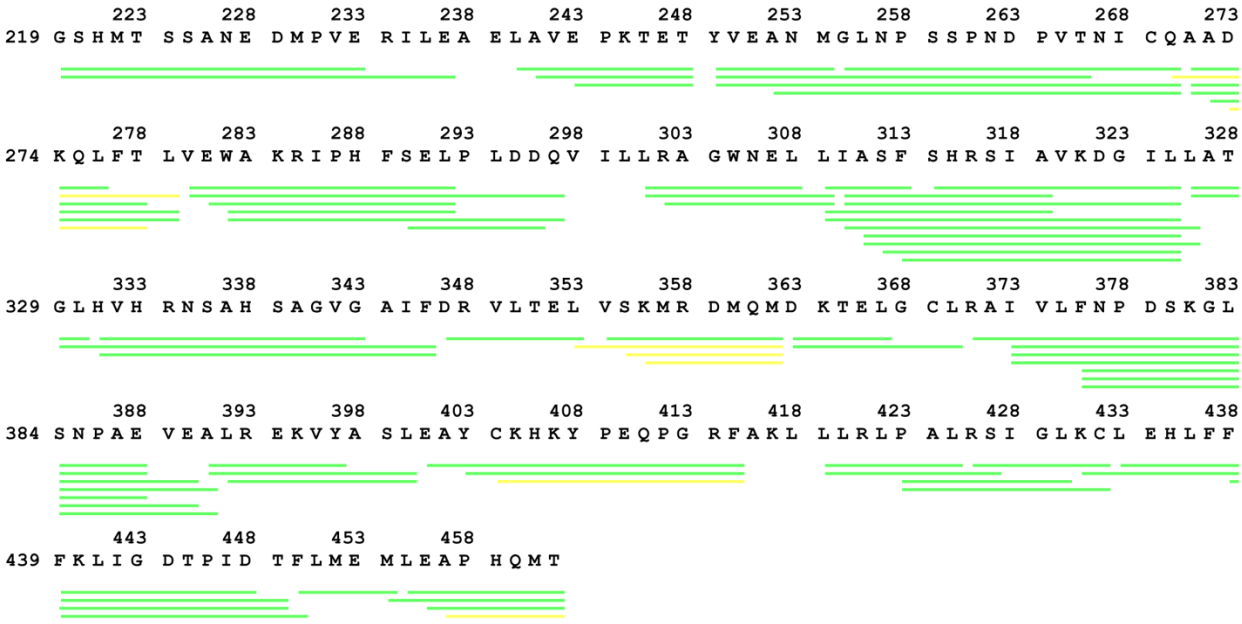

Figure S2. RXRa-LBD HDX-MS coverage map with 78 confirmed peptides covering 97% of the protein. The average length of the peptides were 11.2 with an average redundancy of 3.6.

Data Set: RXR LBD in complex with UAB110, UAB111, 9cUAB30, Targretin	
HDX time course (sec)	15, 30, 60, 300, 900, 3600
# of peptides	78
Sequence Coverage	96.70%
Average peptide length/ Redundancy	11.2/ 3.6
Replicates	3

Figure S3. HDX MS data summary table.

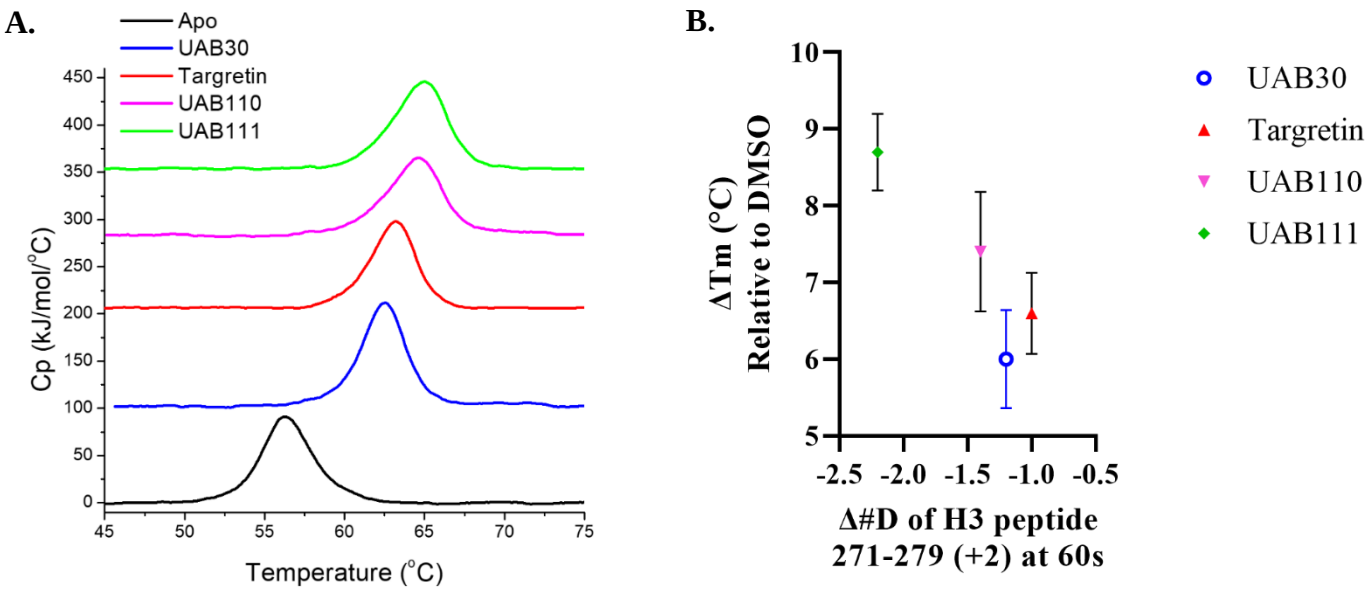

Figure S4. The correlation between the protection of a Helix 3 peptide and increased thermal stability. (*A*) Differential scanning calorimetry (DSC) profiles of RXRα-LBD with or without agonists. The temperature corresponding to the maximum Cp value on each curve is the thermal unfolding temperature (T_m). Curves are Y-shifted for clarity. (*B*) ΔT_m (with respect to the apo-RXRα-LBD) determined from DSC correlates with the decrease in deuterium incorporation determined from HDX analysis of peptide 271-279 (+2) of Apo (black), UAB30 (blue), Targretin (red), UAB110 (magenta), and UAB111 (green).

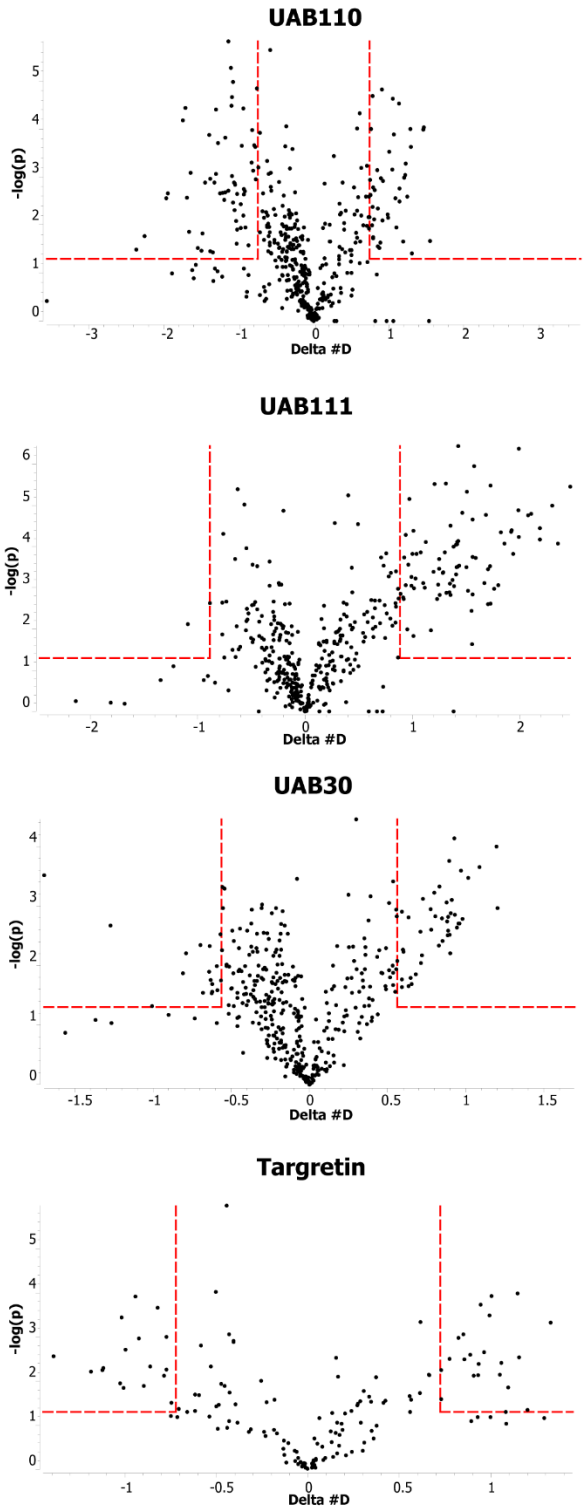

Figure S5. Volcano plots of HDX MS data. Hydrogen-deuterium exchange of rexinoids data is shown in a volcano plot of rexinoids compared to Apo. Volcano plots quantify the significance of a change in deuterium uptake against the magnitude of the change for each time point. The top right and left sectored by a red dotted line indicate the time points that showed significant differences with a 95% confidence level.

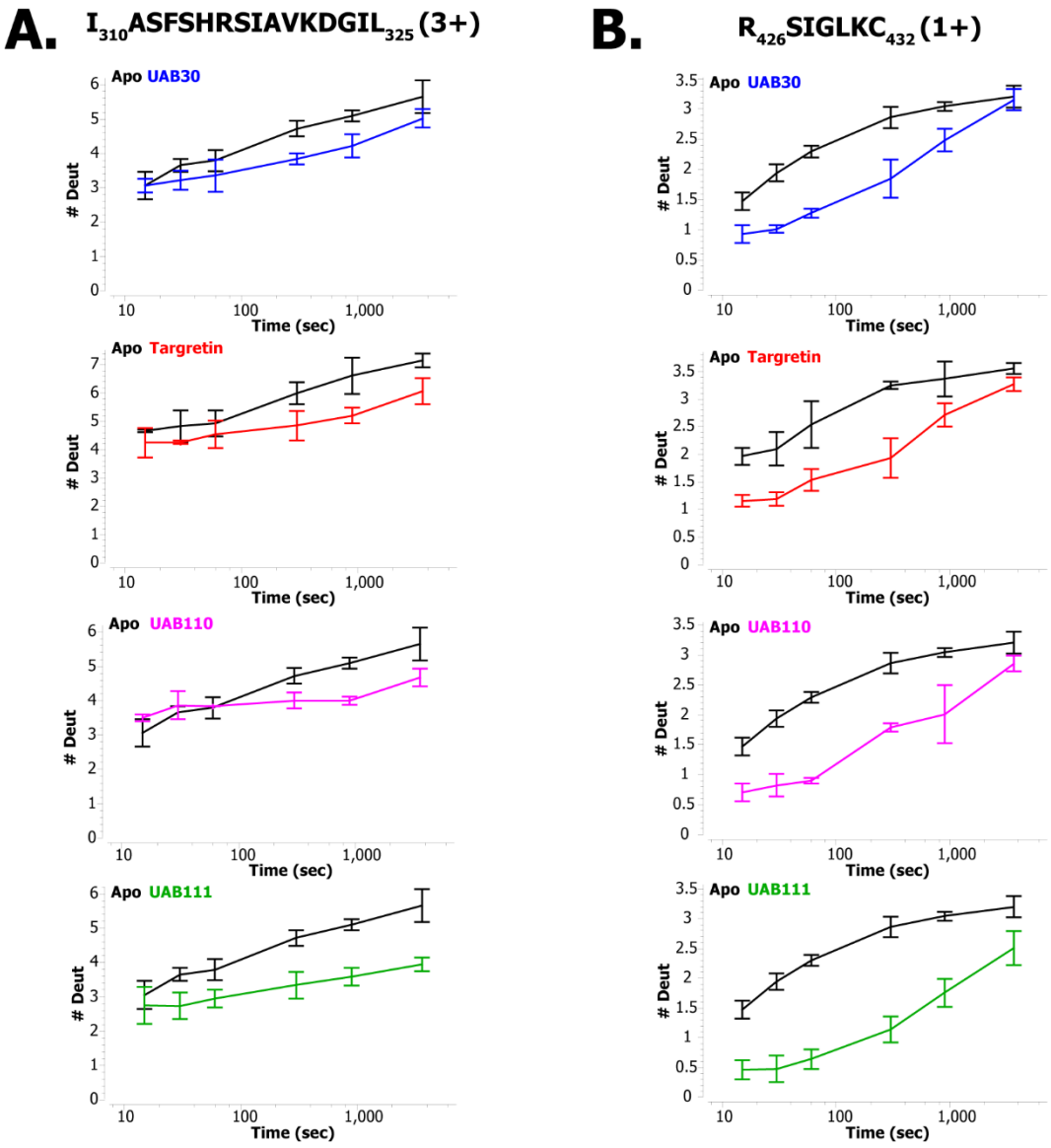

Figure S6. Deuterium incorporation plots of (*A*) Helix 5/B-sheet and (*B*) Helix 11. Both of these regions showed a significant deuterium suppression. (*B*) Peptide, R_{426} $SIGLKC_{432}$ (1+), displayed greater deuterium suppression in UAB111 compared to the other three rexinoids.

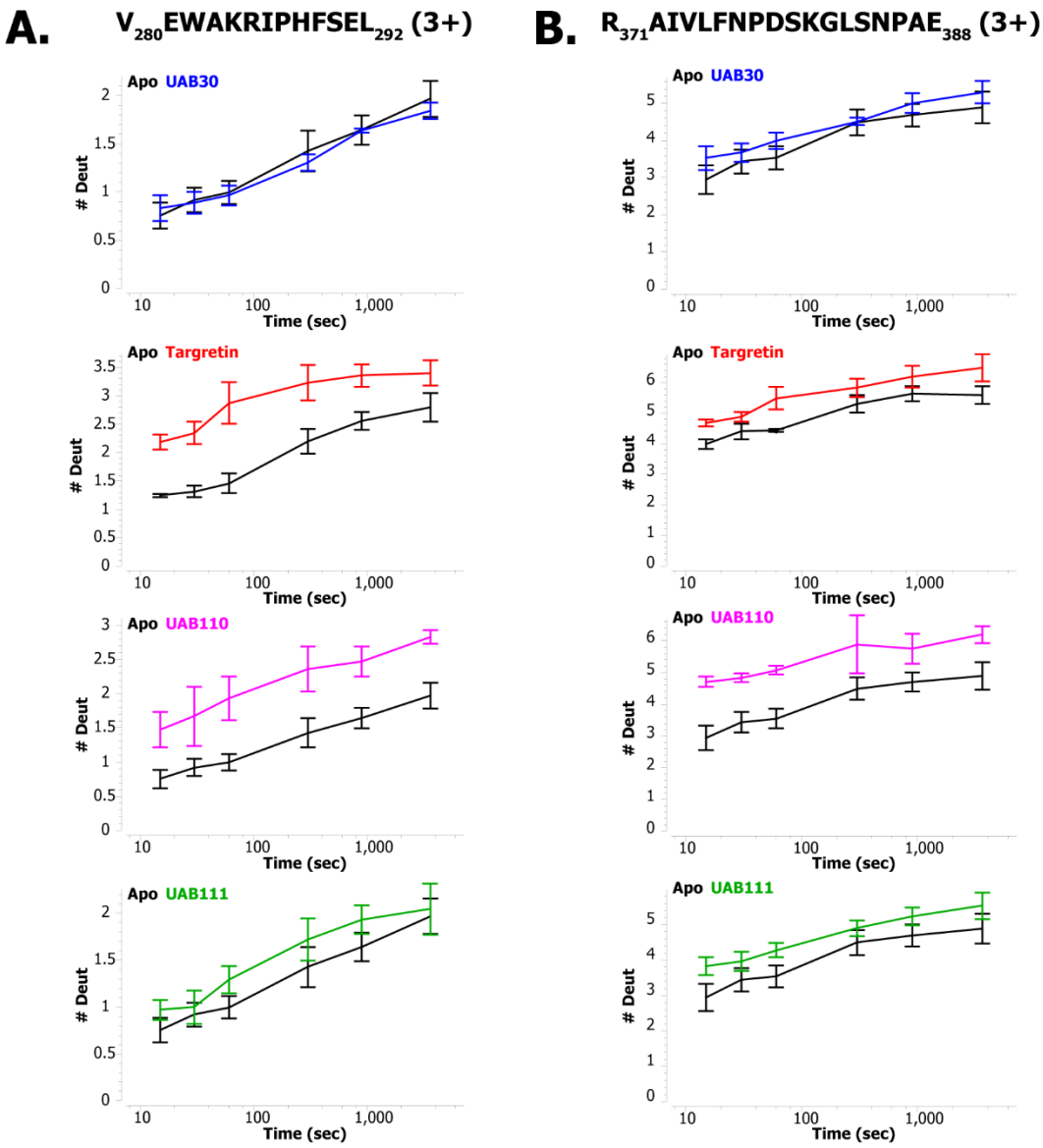

Figure S7. Deuterium incorporation plots of (A) C-Terminus of Helix 3 and (B) Helix 9 showing positive perturbation. (*A*) Helix 3 peptide, $V_{280}EWAKRIPHFSEL_{292}$ (3+), shows more deuterium uptake for Targretin and UAB110 but no difference for UAB30 and UAB111. (*B*) Same can be seen for Helix 9 peptide, $R_{371}AIVLFNPDSKGLSNPAE_{388}$ (3+).

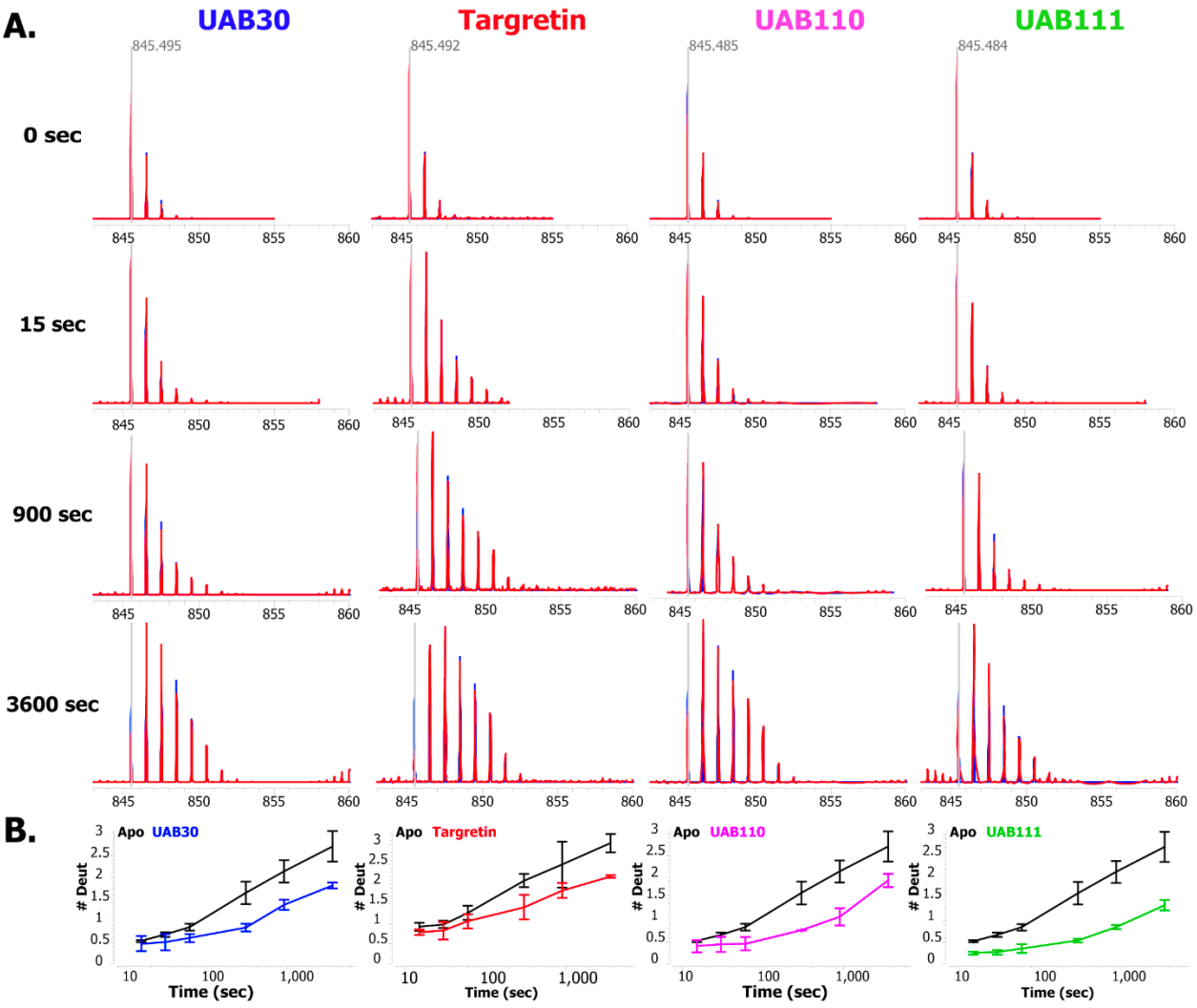

Figure S8. Helix 7 peptide, D_{347} RVLTEL$_{353}$ (1+), HDX-MS analysis. (*A*) Mass spectra of UAB30, Targretin, UAB110, and UAB111 at 0s, 15s, 900s, and 3600s. As the time progresses the mass increases due to deuterium uptake, which can be seen by the spectra shifting from left to right. (*B*) Deuterium incorporation plots of seven time points of each rexinoid. All four rexinoids take up deuterium in equal levels showing a peptide where there is no difference amongst rexinoids.

		UAB30 + Grip-1					
Sequence	**Location**	**15**	**30**	**60**	**300**	**900**	**3600**
AVEPKTET	H1/H2						
YVEANMGLNPSSPNDPVTNI	H2/H3						
AADKQLFT	H3						
AADKQLFTL	H3						
ADKQLFTL	H3						
VEWAKRIPHFSEL	H3/Loop						
SELPLDDQ	Loop/H4						
LRAGWNELL	H4/H5						
RAGWNEL	H4/H5						
IASFSHRSIAVKDGI	H5/β1						
IASFSHRSIAVKDGIL	H5/β1						
FSHRSIAVKDGIL	H5/β1						
LATGLHVHRNSAHSAGVGAIF	β2/H6/H7						
HVHRNSAHSAGVGAIF	β2/H6/H7						
DRVLTEL	H7						
VSKMRDMQM	H7/Loop						
DKTELGCL	Loop/H8						
RAIVLFNPDSKGLSNPAE	H8/H9						
FNPDSKGLSNPAE	Loop/H9						
LREKVYASL	H9						
EAYCKHKYPEQPGRF	H9/Loop/H10						
PALRSIGL	H11						
RSIGLKC	H11						
LEHLFF	H11						
FKLIGDTPIDT	H11/Loop						
FLMEM	H12						
MLEAPHQMT	H12/C-Term						
		15	**30**	**60**	**300**	**900**	**3600**

Figure S9. Difference maps of RXR bound to UAB30 in complex with coactivator, GRIP-1.

UAB110			
Hydrogen Bonds		Salt Bridges	
Interaction	Distance [Å]	Interaction	Distance [Å]
(L8) Lys^{381} - Glu^{352} (H7)	2.87	(L8) Lys^{381} - Glu^{352} (H7)	2.87
(H7) Lys^{356} - Asp^{379} (L8)	2.93	(L10) Arg^{421} - Asp^{379} (L8)	3.84
(H10) Arg^{421} - Asp^{379} (L8)	2.89	(H7) Lys^{356} - Asp^{379} (L8)	2.93
(H10) Arg^{421} - Asp^{379} (L8)	2.81	(H10) Arg^{421} - Asp^{379} (L8)	2.89
(H9) Tyr^{397} - Gly^{413} (H10)	3.57	(H10) Arg^{421} - Asp^{379} (L8)	3.08
(H11) Arg^{426} - Pro^{423} (H11)	3.39	(H10) Arg^{421} - Asp^{379} (L8)	2.81
UAB111			
Hydrogen Bonds		Salt Bridges	
Interaction	Distance [Å]	Interaction	Distance [Å]
(L8) Lys^{381} - Glu^{352} (H7)	3.05	(L8) Lys^{381} - Glu^{352} (H7)	3.05
(H7) Lys^{356} - Asp^{379} (L8)	3.23	(H7) Lys^{356} - Asp^{379} (L8)	3.23
(H10) Arg^{421} - Asp^{379} (L8)	2.83	(H10) Arg^{421} - Asp^{379} (L8)	2.83
(H10) Arg^{421} - Asp^{379} (L8)	2.82	(H10) Arg^{421} - Asp^{379} (L8)	3.23
(H9) Tyr^{397} - Gly^{413} (H10)	3.15	(H10) Arg^{421} - Asp^{379} (L8)	2.82
(H11) Arg^{426} - Pro^{423} (H11)	3.11	**(H10) Lys^{417} - Glu^{390} (H9)**	3.65
		(H10) Lys^{417} - Glu^{394} (H9)	3.76
UAB30			
Hydrogen Bonds		Salt Bridges	
Interaction	Distance [Å]	Interaction	Distance [Å]
(L8) Lys^{381} - Glu^{352} (H7)	3.23	(L8) Lys^{381} - Glu^{352} (H7)	3.23
(H10) Arg^{421} - Asp^{379} (L8)	2.70	(H10) Arg^{421} - Asp^{379} (L8)	2.70
(H7) Lys^{356} - Asp^{379} (L8)	3.49	(H10) Arg^{421} - Asp^{379} (L8)	3.92
(H10) Arg^{421} - Asp^{379} (L8)	3.05	(H7) Lys^{356} - Asp^{379} (L8)	3.49
(H9) Tyr^{397} - Gly^{413} (H10)	3.40	(H10) Arg^{421} - Asp^{379} (L8)	2.95
(H11) Arg^{426} - Pro^{423} (H11)	3.30	(H10) Arg^{421} - Asp^{379} (L8)	3.05
Targretin			
Hydrogen Bonds		Salt Bridges	
Interaction	Distance [Å]	Interaction	Distance [Å]
(L8) Lys^{381} - Glu^{352} (H7)	2.84	(L8) Lys^{381} - Glu^{352} (H7)	2.84
(H10) Arg^{421} - Asp^{379} (L8)	2.67	(H10) Arg^{421} - Asp^{379} (L8)	3.82
(H10) Arg^{421} - Asp^{379} (L8)	3.17	(H10) Arg^{421} - Asp^{379} (L8)	2.67
(L8) Lys^{417} - Glu^{394} (H9)	3.74	(H10) Arg^{421} - Asp^{379} (L8)	3.17
(H9) Lys^{405} - Glu^{401} (H9)	3.38	(H10) Arg^{421} - Asp^{379} (L8)	2.98
(H9) Tyr^{397} - Gly^{413} (H10)	3.26	**(L8) Lys^{417} - Glu^{394} (H9)**	3.74
(H11) Arg^{426} - Pro^{423} (H11)	3.39	**(H9) Lys^{405} - Glu^{401} (H9)**	3.38

Figure S10. Dimerization interface interactions for RXR bound to each rexiniod along with the distance between the interactions in angstroms

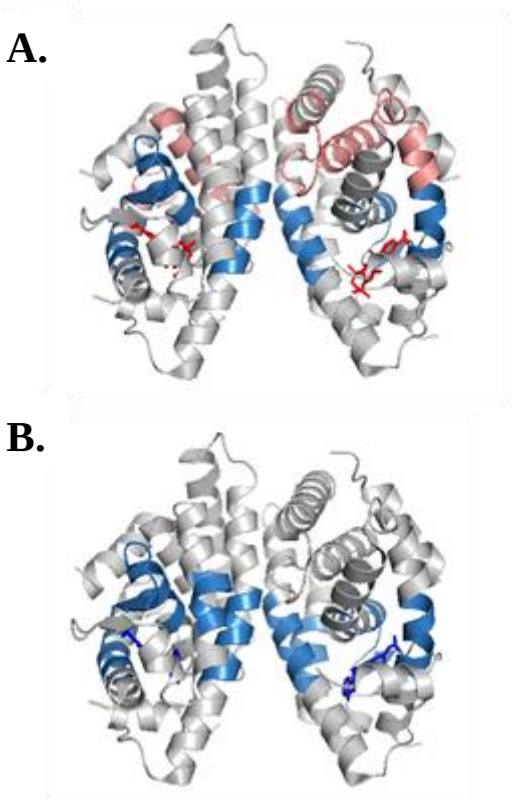

Figure S11. HDX MS results mapped on X-ray crystal structures. (*A*) Targretin in complex with RXR LBD. (*B*) UAB30 in bound with RXR LBD

REFERENCES

1. Bookout, A. L., Jeong, Y., Downes, M., Ruth, T. Y., Evans, R. M., and Mangelsdorf, D. J. (2006) Anatomical profiling of nuclear receptor expression reveals a hierarchical transcriptional network. Cell 126, 789-799

2. Mangelsdorf, D. J., and Evans, R. M. (1995) The RXR heterodimers and orphan receptors. Cell 83, 841-850

3. Santos, R., Ursu, O., Gaulton, A., Bento, A. P., Donadi, R. S., Bologa, C. G., Karlsson, A., Al-Lazikani, B., Hersey, A., and Oprea, T. I. (2017) A comprehensive map of molecular drug targets. Nature reviews Drug discovery 16, 19-34

4. Ottow, E., and Weinmann, H. (2008) Nuclear receptors as drug targets: A historical perspective of modern drug discovery. Nuclear Receptors as Drug Targets, 1-23

5. Mangelsdorf, D. J., Thummel, C., Beato, M., Herrlich, P., Schütz, G., Umesono, K., Blumberg, B., Kastner, P., Mark, M., and Chambon, P. (1995) The nuclear receptor superfamily: the second decade. Cell 83, 835

6. Altucci, L., Leibowitz, M. D., Ogilvie, K. M., de Lera, A. R., and Gronemeyer, H. (2007) RAR and RXR modulation in cancer and metabolic disease. Nature reviews Drug discovery 6, 793-810

7. Kojetin, D. J., Matta-Camacho, E., Hughes, T. S., Srinivasan, S., Nwachukwu, J. C., Cavett, V., Nowak, J., Chalmers, M. J., Marciano, D. P., and Kamenecka, T. M. (2015) Structural mechanism for signal transduction in RXR nuclear receptor heterodimers. Nature communications 6, 1-14

8. Cesario, R. M., Stone, J., Yen, W.-C., Bissonnette, R. P., and Lamph, W. W. (2006) Differentiation and growth inhibition mediated via the RXR: PPARγ heterodimer in colon cancer. Cancer letters 240, 225-233

9. Potter, G. B., Beaudoin, G. M., DeRenzo, C. L., Zarach, J. M., Chen, S. H., and Thompson, C. C. (2001) The hairless gene mutated in congenital hair loss disorders encodes a novel nuclear receptor corepressor. Genes & development 15, 2687-2701

10. Sturm, E., Wagner, M., and Trauner, M. (2009) Nuclear receptor ligands in therapy of cholestatic liver disease. Front Biosci 14, 4299-4325

11. Sánchez-Martínez, R., Castillo, A. I., Steinmeyer, A., and Aranda, A. (2006) The retinoid X receptor ligand restores defective signalling by the vitamin D receptor. EMBO reports 7, 1030-1034

12. Mark, M., Ghyselinck, N. B., and Chambon, P. (2006) Function of retinoid nuclear receptors: lessons from genetic and pharmacological dissections of the retinoic acid signaling pathway during mouse embryogenesis. Annu. Rev. Pharmacol. Toxicol. 46, 451-480

13. Chambon, P. (1996) A decade of molecular biology of retinoic acid receptors. The FASEB journal 10, 940-954

14. Zhao, Q., Chasse, S. A., Devarakonda, S., Sierk, M. L., Ahvazi, B., and Rastinejad, F. (2000) Structural basis of RXR-DNA interactions. Journal of molecular biology 296, 509-520

15. Jeyakumar, M., Tanen, M. R., and Bagchi, M. K. (1997) Analysis of the functional role of steroid receptor coactivator-1 in ligand-induced transactivation by thyroid hormone receptor. Molecular Endocrinology 11, 755-767

16. Han, J. S., and Crowe, D. L. (2010) Steroid receptor coactivator 1 deficiency increases MMTV-neu mediated tumor latency and differentiation specific gene expression, decreases metastasis, and inhibits response to PPAR ligands. BMC cancer 10, 1-14

17. Xia, G., Boerma, L. J., Cox, B. D., Qiu, C., Kang, S., Smith, C. D., Renfrow, M. B., and Muccio, D. D. (2011) Structure, energetics, and dynamics of binding coactivator peptide to the human retinoid X receptor α ligand binding domain complex with 9-cis-retinoic acid. Biochemistry 50, 93-105

18. Boerma, L. J., Xia, G., Qui, C., Cox, B. D., Chalmers, M. J., Smith, C. D., Lobo-Ruppert, S., Griffin, P. R., Muccio, D. D., and Renfrow, M. B. (2014) Defining the communication between agonist and coactivator binding in the retinoid X receptor α ligand binding domain. Journal of Biological Chemistry 289, 814-826

19. Heery, D. M., Kalkhoven, E., Hoare, S., and Parker, M. G. (1997) A signature motif in transcriptional co-activators mediates binding to nuclear receptors. Nature 387, 733-736

20. Overington, J. P., Al-Lazikani, B., and Hopkins, A. L. (2006) How many drug targets are there? Nature reviews Drug discovery 5, 993-996

21. Levin, A. A., Sturzenbecker, L. J., Kazmer, S., Bosakowski, T., Huselton, C., Allenby, G., Speck, J., Rosenberger, M., Lovey, A., and Grippo, J. F. (1992) 9-cis retinoic acid stereoisomer binds and activates the nuclear receptor RXRα. Nature 355, 359-361

22. Heyman, R. A., Mangelsdorf, D. J., Dyck, J. A., Stein, R. B., Eichele, G., Evans, R. M., and Thaller, C. (1992) 9-cis retinoic acid is a high affinity ligand for the retinoid X receptor. Cell 68, 397-406

23. Mangelsdorf, D. J., Borgmeyer, U., Heyman, R. A., Zhou, J. Y., Ong, E. S., Oro, A. E., Kakizuka, A., and Evans, R. M. (1992) Characterization of three RXR genes that mediate the action of 9-cis retinoic acid. Genes & development 6, 329-344

24. Dawson, M. (2004) Synthetic retinoids and their nuclear receptors. Current Medicinal Chemistry-Anti-Cancer Agents 4, 199-230

25. Gottardis, M. M., Bischoff, E. D., Shirley, M. A., Wagoner, M. A., Lamph, W. W., and Heyman, R. A. (1996) Chemoprevention of mammary carcinoma by LGD1069 (Targretin): an RXR-selective ligand. Cancer research 56, 5566-5570

26. Duvic, M., Hymes, K., Heald, P., Breneman, D., Martin, A. G., Myskowski, P., Crowley, C., and Yocum, R. C. (2001) Bexarotene is effective and safe for treatment of refractory advanced-stage cutaneous T-cell lymphoma: multinational phase II-III trial results. Journal of clinical oncology 19, 2456-2471

27. Duvic, M., Martin, A. G., Kim, Y., Olsen, E., Wood, G. S., Crowley, C. A., and Yocum, R. C. (2001) Phase 2 and 3 clinical trial of oral bexarotene (Targretin capsules) for the treatment of refractory or persistent early-stage cutaneous T-cell lymphoma. Archives of dermatology 137, 581-593

28. D Muccio, D., R Atigadda, V., J Brouillette, W., I Bland, K., Krontiras, H., and J Grubbs, C. (2017) Translation of a tissue-selective rexinoid, UAB30, to the clinic for breast cancer prevention. Current topics in medicinal chemistry 17, 676-695

29. Kolesar, J. M., Hoel, R., Pomplun, M., Havighurst, T., Stublaski, J., Wollmer, B., Krontiras, H., Brouillette, W., Muccio, D., and Kim, K. (2010) A pilot, first-in-human, pharmacokinetic study of 9cUAB30 in healthy volunteers. Cancer Prevention Research 3, 1565-1570

30. Vedell, P. T., Lu, Y., Grubbs, C. J., Yin, Y., Jiang, H., Bland, K. I., Muccio, D. D., Cvetkovic, D., You, M., and Lubet, R. (2013) Effects on gene expression in rat liver after administration of RXR agonists: UAB30, 4-methyl-UAB30, and Targretin (Bexarotene). Molecular pharmacology 83, 698-708

31. Williams, A. P., Garner, E. F., Stafman, L. L., Aye, J. M., Quinn, C. H., Marayati, R., Stewart, J. E., Atigadda, V. R., Mroczek-Musulman, E., and Moore, B. P. (2019) UAB30, A Novel Rexinoid Agonist, Decreases Stemness In Group 3 Medulloblastoma Human Cell Line Xenografts. Translational oncology 12, 1364-1374

32. Wu, L., Chaudhary, S. C., Atigadda, V. R., Belyaeva, O. V., Harville, S. R., Elmets, C. A., Muccio, D. D., Athar, M., and Kedishvili, N. Y. (2016) Retinoid X receptor agonists upregulate genes responsible for the biosynthesis of all-trans-retinoic acid in human epidermis. PLoS One 11, e0153556

33. Atigadda, V. R., Xia, G., Deshpande, A., Wu, L., Kedishvili, N., Smith, C. D., Krontiras, H., Bland, K. I., Grubbs, C. J., and Brouillette, W. J. (2015) Conformationally defined rexinoids and their efficacy in the prevention of mammary cancers. Journal of medicinal chemistry 58, 7763-7774

34. Atigadda, V. R., Xia, G., Desphande, A., Boerma, L. J., Lobo-Ruppert, S., Grubbs, C. J., Smith, C. D., Brouillette, W. J., and Muccio, D. D. (2014) Methyl substitution of a rexinoid agonist improves potency and reveals site of lipid toxicity. Journal of medicinal chemistry 57, 5370-5380

35. Desphande, A., Xia, G., Boerma, L. J., Vines, K. K., Atigadda, V. R., Lobo-Ruppert, S., Grubbs, C. J., Moeinpour, F. L., Smith, C. D., and Christov, K. (2014) Methyl-substituted conformationally constrained rexinoid agonists for the retinoid X receptors demonstrate improved efficacy for cancer therapy and prevention. Bioorganic & medicinal chemistry 22, 178-185

36. Chandra, V., Wu, D., Li, S., Potluri, N., Kim, Y., and Rastinejad, F. (2017) The quaternary architecture of RARβ–RXRα heterodimer facilitates domain–domain signal transmission. Nature communications 8, 1-9

37. Mayne, L. (2016) Hydrogen exchange mass spectrometry. in Methods in enzymology, Elsevier. pp 335-356

38. Marcsisin, S. R., and Engen, J. R. (2010) Hydrogen exchange mass spectrometry: what is it and what can it tell us? Analytical and bioanalytical chemistry 397, 967-972

39. Hodge, E. A., Benhaim, M. A., and Lee, K. K. (2020) Bridging protein structure, dynamics, and function using hydrogen/deuterium-exchange mass spectrometry. Protein Science 29, 843-855

40. Engen, J. R. (2009) Analysis of protein conformation and dynamics by hydrogen/deuterium exchange MS. ACS Publications

41. Morgan, C. R., and Engen, J. R. (2009) Investigating solution-phase protein structure and dynamics by hydrogen exchange mass spectrometry. Current protocols in protein science 58, 17.16. 11-17.16. 17

42. Yang, Z., Muccio, D. D., Melo, N., Atigadda, V. R., and Renfrow, M. B. (2021) Stability of the Retinoid X Receptor-α Homodimer in the Presence and Absence of Rexinoid and Coactivator Peptide. Biochemistry 60, 1165-1177

43. Strutzenberg, T. S., Garcia-Ordonez, R. D., Novick, S. J., Park, H., Chang, M. R., Doebellin, C., He, Y., Patouret, R., Kamenecka, T. M., and Griffin, P. R. (2019) HDX-MS reveals structural determinants for RORγ hyperactivation by synthetic agonists. Elife 8, e47172

44. Krissinel, E., and Henrick, K. (2007) Inference of macromolecular assemblies from crystalline state. Journal of molecular biology 372, 774-797

45. Evans, R. M., and Mangelsdorf, D. J. (2014) Nuclear receptors, RXR, and the big bang. Cell 157, 255-266

46. Kawaguchi, R., Zhong, M., Kassai, M., Ter-Stepanian, M., and Sun, H. (2015) Vitamin A transport mechanism of the multitransmembrane cell-surface receptor STRA6. Membranes 5, 425-453

47. O'Byrne, S. M., and Blaner, W. S. (2013) Retinol and retinyl esters: biochemistry and physiology: thematic review series: fat-soluble vitamins: vitamin A. Journal of lipid research 54, 1731-1743

48. Niles, R. M. (2004) Signaling pathways in retinoid chemoprevention and treatment of cancer. Mutation Research/Fundamental and Molecular Mechanisms of Mutagenesis 555, 97-105

49. Langenfeld, J., Kiyokawa, H., Sekula, D., Boyle, J., and Dmitrovsky, E. (1997) Posttranslational regulation of cyclin D1 by retinoic acid: a chemoprevention mechanism. Proceedings of the National Academy of Sciences 94, 12070-12074

50. Matsuo, T., and Thiele, C. J. (1998) p27 Kip1: a key mediator of retinoic acid induced growth arrest in the SMS–KCNR human neuroblastoma cell line. Oncogene 16, 3337-3343

51. Teixeira, C., and Pratt, M. C. (1997) CDK2 is a target for retinoic acid-mediated growth inhibition in MCF-7 human breast cancer cells. Molecular endocrinology 11, 1191-1202

52. Chen, L.-C., Sly, L., and De Luca, L. M. (1994) High dietary retinoic acid prevents malignant conversion of skin papillomas induced by a two-stage carcinogenesis protocol in female SENCAR mice. Carcinogenesis 15, 2383-2386

53. Fujimura, S., Suzumiya, J., Anzai, K., Ohkubo, K., Hata, T., Yamada, Y., Kamihira, S., Kikuchi, M., and Ono, J. (1998) Retinoic acids induce growth inhibition and apoptosis in adult T-cell leukemia (ATL) cell lines. Leukemia research 22, 611-618

54. Hsu, S.-L., Yin, S.-C., Liu, M.-C., Reichert, U., and Ho, W. L. (1999) Involvement of cyclin-dependent kinase activities in CD437-induced apoptosis. Experimental cell research 252, 332-341

55. Reynolds, C. P., Matthay, K. K., Villablanca, J. G., and Maurer, B. J. (2003) Retinoid therapy of high-risk neuroblastoma. Cancer letters 197, 185-192

56. Giuli, M. V., Hanieh, P. N., Giuliani, E., Rinaldi, F., Marianecci, C., Screpanti, I., Checquolo, S., and Carafa, M. (2020) Current trends in ATRA delivery for cancer therapy. Pharmaceutics 12, 707

57. Belorusova, A. Y., Evertsson, E., Hovdal, D., Sandmark, J., Bratt, E., Maxvall, I., Schulman, I. G., Åkerblad, P., and Lindstedt, E.-L. (2019) Structural analysis identifies an escape route from the adverse lipogenic effects of liver X receptor ligands. Communications biology 2, 1-13

58. Bourguet, W., Ruff, M., Chambon, P., Gronemeyer, H., and Moras, D. (1995) Crystal structure of the ligand-binding domain of the human nuclear receptor RXR-α. Nature 375, 377-382

59. Senicourt, L., Le Maire, A., Allemand, F., Carvalho, J. E., Guee, L., Germain, P., Schubert, M., Bernadó, P., Bourguet, W., and Sibille, N. (2021) Structural insights into the interaction of the intrinsically disordered co-activator TIF2 with retinoic acid receptor heterodimer (RXR/RAR). Journal of molecular biology 433, 166899

60. Lee, S.-A., Belyaeva, O. V., Wu, L., and Kedishvili, N. Y. (2011) Retinol dehydrogenase 10 but not retinol/sterol dehydrogenase (s) regulates the expression of retinoic acid-responsive genes in human transgenic skin raft culture. Journal of Biological Chemistry 286, 13550-13560

61. Wang, H.-J., Chen, T., Cheng, L., Cheng, T., and Tung, Y. (1995) Human keratinocyte culture using porcine pituitary extract in serum-free medium. Burns 21, 503-506

62. Pfaffl, M. W. (2001) A new mathematical model for relative quantification in real-time RT–PCR. Nucleic acids research 29, e45-e45

63. Napoli, J. L., and Horst, R. L. (1998) Quantitative analyses of naturally occurring retinoids. Retinoid Protocols, 29-40

64. Egea, P. F., and Moras, D. (2001) Purification and crystallization of the human RXRα ligand-binding domain–9-cisRA complex. Acta Crystallographica Section D: Biological Crystallography 57, 434-437

65. Hageman, T. S., and Weis, D. D. (2019) Reliable identification of significant differences in differential hydrogen exchange-mass spectrometry measurements using a hybrid significance testing approach. *Analytical chemistry* **91**, 8008-8016

CHAPTER III
ANALYZING THE STRUCTURAL DYNAMICS OF RETINOID X RECEPTOR BOUND TO UAB30 METHYLATED DERIVATIVES

by

NATHALIA MELO, ALEXANDER ROSENBURG, ZHENGRONG YANG, DONALD MUCCIO, VENKATRAM ATIGADDA, MATTHEW B. RENFROW

In preparation for *Biochemistry*

Format adapted for dissertation

ABSTRACT

Retinoid x receptor (RXR), a nuclear receptor, is involved in ligand inducible transcription and is a key modulator of cellular proliferation, differentiation, and growth. RXR functions by heterodimerizing with several other nuclear receptors, including retinoic acid receptors (RAR). Agonists that exclusively target RXR are known as rexinoids, which pioneer conformational changes allowing for coactivator recruitment and transcriptional initiation. 9-cis-UAB30 (UAB30), is a non-toxic rexinoid and has been previously shown to have anti-cancer properties in several different model systems. UAB30 methyl derivatives (4mUAB30, 5mUAB30, 6mUAB30, 7mUAB30, and 8mUAB30) are next-generation rexinoids that have shown similar anti-cancer properties. Structure, function, and dynamics are three key components in understanding RXR's mechanism of action. We have previously investigated RXR in complex with UAB30 methylated derivatives through X-ray crystallography and several in vitro and in vivo systems. In this work, we analyzed the structural and dynamical changes produced upon UAB30 methyl derivatives binding to the human RXRα ligand-binding domain (LBD). Hydrogen deuterium exchange mass spectrometry identified two distinct responses of the RXRα LBD to the two rexinoids: reduced dynamics of the ligand-binding pocket and de-protection of the C-terminal end of Helix 3, Helix 8, and Helix 9 towards the dimer interface. Taken together, our studies show that UAB30 methylated derivatives follow the two responses of binding we previously revealed.

INTRODUCTION

Nuclear Receptors (NR) are targets for drug discovery due to physiological activation by low-molecular-mass ligands (1-3). Retinoid X receptor is a Class II NR and can perform its function by heterodimerizing with several other NRs, which leads to DNA binding and downstream gene translation (4). Agonists that exclusively target RXR are known as rexinoids. While the presence of the RXR ligand is not always required for the function of RXR heterodimers, the addition of RXR agonists can enhance the transcriptional activities of heterodimeric nuclear receptors (5). This property makes RXR an attractive target for pharmacotherapy.

The first RXR agonist to be discovered was 9-*cis*-Retinoic acid (9cRA) (6-8). 9cRA is used for the treatment of skin sores caused by Kaposi Sarcoma, but as a side effect induces hypertriglyceridemia (9). An FDA-approved rexinoid, Bexarotene (Targretin), is used to treat Cutaneous T-Cell Lymphoma (CTCL) (10-12). Even though Targretin is substantially less toxic in humans than 9cRA, hypertriglyceridemia, hypercholesterolemia, and hypothyroidism occur frequently. To achieve higher RXR selectivity, while still remaining non-toxic, our group has designed rexinoids that are effective agents to inhibit epithelial cancer formation but with lower toxicity than Targretin

Our group has designed an RXR-selective rexinoid, 9-*cis*-UAB30 (UAB30), based on the structure of 9cRA. UAB30 was effective in aiding in the prevention of cancer in cells and rodents (13-15). Treatment of UAB30 showed to not increase serum triglycerides (16). As shown in our previous study, treatment of

human organotypic epithelium with UAB30 resulted in increased levels of all-trans-retinoic acid (ATRA) and upregulation of ATRA target genes (14). However, UAB30 was significantly less potent as a transcriptional regulator than Targretin, at least in this model. To further improve the potency of UAB30, we synthesized UAB30 methylated derivatives: 4mUAB30, 5mUAB30, 6mUAB30, 7mUAB30, and 8mUAB30 (Fig. 1). The analogs differ in the positioning of a single methyl group to various sites of the tetralone ring. They are named accordingly based on which carbon the methyl group is attached to on the tetralone ring. In our previous studies, using receptor reporter assays in RK3E cells, the EC50 values for RXRα activation were reported (17). 5mUAB30 and 8mUAB30 had similar EC50 values to UAB30. The EC50 values of 4mUAB30, 6mUAB30, and 7mUAB30 were similar to 9cRA and much lower than UAB30. The methyl derivatives were then tested for RARα activation. The majority of rexinoids did not induce activation of RARα, except for 8mUAB30 which increased activation of RAR-mediated transcription by 20% (17). The methyl derivatives were tested on an animal model of methylnitrosourea (MNU) induced mammary cancer, where treatment with 4mUAB30 and 7mUAB30 reduced mammary cancer multiplicity (18). Both 5mUAB30 and 6mUAB30 did not produce any chemopreventive activity while interestingly, treatment of 8mUAB30 increased the growth of mammary cancers by 108% (18). These rexinoids were found to be effective in preventing breast cancers in an in vivo rat model alone or in combination with tamoxifen (19-22). The derivatives were also examined in neuroblastoma where treatment of 6mUAB30 was shown to induce differentiation and growth arrest in neuroblastoma (23,24).

Given that elevations of serum triglycerides are a dose-limiting toxicity of the rexinoid drug class, we were interested in how our methyl homologs UAB30 would affect these levels given their differential experimental effects. (17). When compared to UAB30 treatment in rats, 5mUAB30, 6mUAB30, and 8mUAB30 had similar serum TG levels. 4mUAB30 raised TG levels by 420% which was similar to the levels seen in Targretin treatment, while 7mUAB30 had the highest levels of TGs with a 642% increase. This data indicates that although 4mUAB30 and 7mUAB30 have chemopreventative effects, they are highly toxic and likely clinically irrelevant.

The design of the UAB30 methylated derivatives was facilitated by using X-ray crystallography to define the binding pocket and geometry of the rexinoid bound to RXRα-LBD (Fig. 1). The crystal structures show that the methyl derivatives fill the ligand pocket while still preserving the L-shaped geometry seen in UAB30 and Targretin (17,21). Similar to Targretin and 9cRA, 4mUAB30 was shown to interact with helices 3 and 7 more than UAB30 (21). In the RXRα-LBD homodimer, there is also a π-turn located in helix 7 (25). The π-turn consists of RxxxE motif, and is part of the RXR homodimer interface. The motif helps in stabilizing the interface by forming a salt bridge with Glu352 in helix 7 of one monomer to Lys381 in the loop between helix 8 and 9 of the other monomer. While analyzing the crystal structures, we found that the structures between all methyl derivatives were extremely similar, leaving no structural explanation for their differing clinical outcomes. While crucial for the design process, crystallographic structures are static snapshots of ligand-bound proteins that exist in solution with

dynamic molecular motions (26). We and others have made use of hydrogen-deuterium exchange mass spectrometry (HDX MS) to examine rexinoid-induced structural dynamics in RXR (27,28). Through this technique, we have been able to analyze rexinoid binding sites and binding-associated structural dynamics. In our previous work, we showed that the binding of either UAB30 or Targretin to RXRα LBD reduces deuterium incorporation and stabilizes regions in the ligand-binding pocket (29,30). Furthermore, our studies revealed that the binding of coactivator binding peptide, GRIP-1, to RXRα LBD reduces dynamics for the surfaces for the coactivator binding pocket (helices 3, 4, and 12) (29).

We have previously shown that the UAB30 methyl derivatives have EC50's acting on RXR that are more potent compared to UAB30 in a Gal4 cell line reporter assay (17). Given this, coupled with the lack of differences in crystal structures, the question remains about how these rexinoids exert their differential effects. Here we investigate their biophysical properties by HDX MS to gain further analysis of the RXRα LBD that could explain these differences Analysis of dynamic structural profiles of the LBD upon rexinoid binding identifies that each rexinoid creates unique dynamic profiles, demonstrating a stepwise process of ligand-specific activation and dimer interface interactions to inform our understanding of how ligands differentially activate RXR.

MATERIALS AND METHODS

Protein Expression and Purification

The human RXRα LBD was overexpressed and purified using the same methodology as described by Xia et al (30). RXRα LBD was tagged with a His6- tag and separated using a HiTrap Ni-chelating column (GE Healthcare, Piscataway, NJ). The tag was then removed using a-thrombin and confirmed using mass spectrometry (MALDI-TOF). Using size-exclusion chromatography with a HiLoad Superdex 75 column, the RXRa LBD homodimers were separated from the tetramers. The complexes were then confirmed through MALDI-TOF and SDS-PAGE analysis.

Hydrogen Deuterium Exchange Mass Spectrometry

HDX MS experiments were performed using a LEAP HD/X-PAL fluidics system (Trajan). HDX experiments and analysis were performed as previously described (Melo et al). RXRα LBD homodimer: rexinoid complexes were formed by incubating them at a 1:10 (protein: ligand) ratio for 1 hour on ice. The sample was then diluted into a deuterium buffer (10 mM Tris, 50 mM NaCl, 0.5 mM EDTA, and 2 mM DTT) for various time points (15, 30, 60, 300, 900, and 3600 s) at 20 °C. After the conclusion of the time point, 50 uL of the sample was injected into 50 uL of quench buffer (3 M Urea, 1% TFA, 50 mM TCEP, pH 2.5) at 4 °C. Enzymatic Waters pepsin column (2.1 mm x 30 mm) was then used to digest the samples for 120 s. Samples were then captured and desalted on an Acclaim PepMap C18 trap column (Thermo Fisher) then an Acquity BEH C18 reverse-phase column (1 mm x 50 mm; Waters Corp.) analytical column using a Waters Acquity pump system. Liquid chromatography was performed using a linear gradient of an increasing concentration from 5% to 90% of

acetonitrile with 0.1 % formic acid. The eluent was injected into a SYNAPT G2-Si and acquired over the scan range of 300 – 1500 m/z. ProteinLynx Global Server (Waters) was used to select peptides and the amount of deuterium exchange was quantified using HDExaminer software (Sierra Analytics, Modesto, CA). Details of the HDX experiments are provided in Supplemental Figure 1.

RESULTS AND DISCUSSION

I. HDX MS Analysis of Triglyceride inducing rexinoids bound to RXRα LBD Homodimers

The structural and dynamic effects of rexinoid binding to RXRα LBD homodimer were analyzed using HDX MS. RXRα LBD with no ligand present (apo state) was used as a reference and the experimental time course ranged from 15 s to 3600 s. An increase in deuterium incorporation (shades of red) signified a decrease in protection and an increase in dynamics. The opposite is true for a decrease in deuterium (shades of blue) resulting in an increase in protection and a decrease in dynamics (Fig. 2). HDX MS results of the 300 s time point were mapped onto the crystal structures of RXR bound to 4mUAB30 (PBDid: 4M8H) and 7mUAB30 (PBDid: 4POJ). The crystal structures of rexinoids bound to RXR were only able to be crystallized with the coactivator peptide, GRIP-1 incorporated (17,21). Crystal structures of RXR in complex with ligand alone have proven too challenging for a crystal structure to be devised. Given this, our method has given insight into rexinoid-inducing structural mechanisms.

Overall, both compounds displayed a decrease in deuterium exchange (decrease dynamics) for regions in the ligand-binding pocket (LBP): helix 3, helix 5, β-sheet, helix 7, and helix 11. However, while both conditions caused reduced dynamics in the LBP

they affected the amount of exchange in different ways. For RXR in complex with 4mUAB30, there was the largest decrease in dynamics for helix 5 and β-sheet (Fig. 2). 7mUAB30 bound to RXR had the greatest reduction in dynamics in helix 3. HDX MS results displayed dynamic alterations outside of the LBP. 4mUAB30 had a decrease in exchange in helix 6, whereas 7mUAB showed no significant differences. Unlike 4mUAB30, 7mUAB30 had a response of binding resulting in increased dynamics in helices 8 and 9. These regions that had decreased protection consisted of the RXRα LBD homodimer interface.

In our previous studies, we analyzed the crystal structures of the methyl derivatives in complex with RXRα LBD. Through the structural analysis, we found that hyperlipidemia-inducing rexinoids interacted with residues on helix 7 (F369 and V349) and was termed a toxicity "hot spot". In our current work, HDX results displayed that RXR-4mUAB30 reduced dynamics in the helix 7 regions. In Melo et al. HDX results of UAB111, which is also a rexinoid that significantly induces hyperlipidemia, displayed reduced dynamics in these same regions. Given that two toxic rexinoids, 4mUAB30 and UAB111, both induced decreased dynamics in the helix 7 this could be a structural dynamic toxicity marker for future rexinoid studies. In our current work, 7mUAB30 is also a toxic rexinoid however, RXR-7mUAB30 did not display decreased dynamics in helix 7. These results show that toxicity effects are not limited to one mechanism of action.

II. Structural Dynamics of Non-toxic Rexinoids in Complex with RXRα LBD Homodimers

HDX MS analysis of rexinoids that were previously shown to not induce hyperlipidemia were mapped onto their respective X-ray crystal structures (5mUAB30 PBDid: 4PP5, 6mUAB30 PBDid: 4PP3, 8mUAB30 PBDid: 4POH) (Fig. 3) (17,21). All non-toxic rexinoids (5mUAB30, 6mUAB30, and 8mUAB30) had protective effects in regions of the ligand-binding pocket, but varied amongst their levels. RXR-5mUAB30 and RXR-6mUAB30 did not show significant differences in helix 3 when compared to apo, but both complexes displayed reduced dynamics in helix 5, which was not present in RXR-8mUAB30. 6mUAB30 in complex with RXR had the greatest reduction in dynamics in helix 11 compared to all other complexes. Finally, 8mUAB30 bound to RXR incorporated the highest amount of exchange in helix 3. RXR-8mUAB30 differed from both RXR-5mUAB30 and RXR-6mUAB30 due to the HDX results displaying no significant exchange in helix 7. However, RXR-8mUAB30 had a significant reduction in the dynamics of the C-terminal end of helix 11 and the loop between helix 11 and helix 12. In the same way that RXRα LBD-7mUAB30 decreased protection of the helices 8 and 9 regions, 8mUAB30 also had an increase in dynamics in these same regions.

Figure 4 displays a difference map with several peptide sequences and the locations of the peptides. HDX MS data collected from the UAB30 methylated derivatives at various time points revealed the influx of dynamics from 15s to 3600s. The analysis of various time points allowed for the further validation of studying dynamics due to the differences in levels of exchange exhibited throughout varying time points. RXR in complex with 7mUAB30 and RXR-8mUAB30 revealed increased dynamics in

helices 8 and 9 and the loop between them. The RXRα LBD homodimer interface consists of several regions including helices 9, 10, and 11, and the loop between helices 8 and 9. In HDX MS results of the RXRα LBD complexes, we revealed increased dynamics in the regions of the RXRα LBD homodimer interface. These results could translate not only to RXR but also to another nuclear receptor, the retinoic acid receptor (RAR) which has a similar dimerization interface when bound to RXR (31,32). Dai et al. analyzed selective estrogen receptor modulators (SERM) binding to estrogen receptor (ER) using HDX MS. Within their study, the loop between helices 9 and 10, and part of helix 10 revealed increased dynamics compared to the apo state. These regions were associated with the homodimerization interface. Belorusova et al. explored the structural dynamics of agonists binding to liver X receptor (LXR) which showed an increase in exchange in the C-terminal end of helix 3, the loop between helices 8 and 9, and the N-terminal end of helix 9. However, they did not make further conclusions as to why there was an increase in dynamics for those regions. Both of these studies show that the responses of binding we revealed of rexinoids binding to RXR can be translated into other NRs.

Our previous in vitro and in vivo studies revealed numerous similarities between 5mUAB30 and 6mUAB30 (17,21). Neither rexinoid increased serum triglyceride levels (31% and 51%, respectively). The binding affinities were also comparable with 5mUAB30 having a Kd of ~18 nM and the Kd of 6mUAB30 being ~15 nm. HDX MS results of RXR bound to either of these rexinoids correlated with the previous work done in that the exchange profiles only differed with helix 11.

Overall, all rexinoids bound to RXR LBD induced a decrease in dynamics in helix 3. Rexinoids 7mUAB30 and 8mUAB30 had the greatest increase in protection of helix 3. The dynamics of several other NRs have been studied and numerous groups reported reduced dynamics in helix 3 (33,34). In heterodimers of RXR-VDR, a VDR ligand 1,25D3, binding induced decreased dynamics in helix 3 of RXR. This potentially indicates that helix 3 is involved in heterodimerization allosteric communication. The variation of dynamics of the helix indicates that it plays an important role in RXR's homodimer and heterodimer function.

Most NR research focuses on RXR's heterodimer binding partner (35). If RXR is utilized in the study, 9cRA is often used as an agonist, along with a coactivator present (32). In studies that do on RXR, they mainly focus on RXR's "active conformation" centering on the coactivator binding site (H3, H4, and H12). Given this, there is a gap in knowledge in understanding rexinoid binding effect on the RXRα LBD. Most structural features for allosteric signal integration have remained a mystery, limited in part by our insufficient structural understanding of signaling within the individual domains. Our work above has taken the first step in elucidating how the RXRα LBD domain is modified by binding with various structurally similar ligands, which allows us to begin to deconstruct our understanding of how ligands differentially dynamically alter RXRα LBD.

IV. Structural Dynamics of the Ternary Structures of RXRα LBD-Rexinoid-GRIP-1

Agonist rexinoid binding to RXR induces conformational changes for coactivator recruitment (36). HDX MS was performed on the RXR ternary structures of the UAB30 methylated derivatives to guide the understanding of coactivator binding (Fig. 5 and 6).

The coactivator peptide, GRIP-1, is involved in both RXR homodimers and RXR-RAR heterodimers and was used for these studies (31). GRIP-1 involves an LxxLL motif and binds to helices 3, 4, and 11 on the RXR LBD. All UAB30 methylated derivatives displayed reduced dynamics in the coactivator binding site and the ligand-binding pocket. RXR-4mUAB30-GRIP-1 and RXR-8mUAB30-GRIP-1 complexes displayed the greatest reduction in dynamics followed by the ternary structures of 5mUAB30 and 7mUAB30. RXR-8mUAB30-GRIP-1 complex displayed the greatest amount of protection. Interestingly, 8mUAB30 both in HDX results and in the MNU mammary cancer models had unique results that differed from the other rexinoids. It appears as though the binding of 8mUAB30 and GRIP-1 lock RXR in an over-activated state. Coactivator binding to all ternary complexes, except for RXR-6mUAB30, reduced dynamics in helices 8 and 9. Helix 11 is part of the RXR homodimer interface and showed the lowest level of exchange in the RXR-6mUAB30 complex. This could be an indication of why coactivator binding did not further reduce the dynamics in the interface since the region was already stabilized by 6mUAB30 binding.

Ternary complexes involving 8mUAB30, 4mUAB30, and 7mUAB30 increased protection in H12. An increase in protection of helix 12, also known as the activation function-2 (AF-2) site, has been correlated with full agonist activity in PPARγ (34). Interestingly, these three ternary complexes also displayed reduced dynamics in helix 6 that was not observed for RXR-5mUAB30 or RXR-6mUAB30. The ternary structure of RXR-6mUAB30-Grip-1 displayed the lowest amount of deuterium incorporation in the coactivator binding site (Fig. 6). Potentially signifies that 6mUAB30 is a partial agonist. Partial agonists have proven to be a viable strategy for NRs. The positives about partial

agonists are that they can show a dissociation between positive and adverse effects. Interestingly, the ternary complex of RXR-6mUAB30-GRIP-1 is the only complex in which GRIP-1 interacting with RXR involves one charge clamp instead of two (17). This could explain why there was a lower amount of exchange in regions of the coactivator binding site.

V. Independent Hierarchical Clustering Analysis of HDX MS Results

To aid in the understanding of rexinoid and coactivator's mechanism of action when bound to RXR, we performed an independent clustering analysis on 19 RXRα LBD complexes (Fig. 7). Within these 19 RXR complexes, there were 11 RXRα LBD with rexinoid bound and 8 RXRα LBD with rexinoid and coactivator bound results. The ward's method was used as the criterion applied in the hierarchical cluster analysis. Figure 7 displayed a heat map of HDX MS results of all 19 RXRα LBD complexes. The dendrogram located on the left allowed for the visualization of the clustering analysis. Columns represented the peptide sequences as well as the locations of the peptides on the RXRα LBD. The rows were the HDX results of each RXRα LBD-rexinoid or RXRα LBD-rexinoid-coactivator complex. The majority of RXR ternary HDX results were clustered together on the top of the heat map (Fig. 7). Only two of the 8 complexes were not in the top cluster which was RXRα LBD-UAB30-GRIP-1 and RXRα LBD-6mUAB30-GRIP-1. RXRα LBD in complex with both 8mUAB30 and GRIP-1 resulted in the greatest reduction of deuterium incorporation throughout the entire LBD. The results of UAB110 and UAB111 in the ternary structures revealed the most similarities among the HDX results. The dendrogram also clustered UAB30, 5mUAB30, and 6mUAB30 HDX results which correlate to our in vitro and in vivo analyses of these

rexinoids (17,21). Through hierarchical clustering analysis, we have determined that the highest levels of distinct responses of binding are displayed with RXR-rexinoid alone, without GRIP-1 present.

CONCLUSIONS

In this study, we demonstrated through HDX MS that structurally similar rexinoids produce distinct responses of binding. Exchange profiles of RXR-rexinoid complexes correlated with the two previously reported responses of rexinoid binding. The first response of binding was a reduction of dynamics in helices 3 and 5. In helix 3, the greatest reduction of deuterium was displayed in the middle of the helix specifically, A^{271}ADKQLFTL^{279}. For helix 5, I^{310}ASFSHRSIAVKDGILL^{326}, also had the lowest number of deuterium incorporation. HDX MS results of RXR-4mUAB30 and RXR-7mUAB30 displayed the greatest reduction in dynamics in the LBP. Through a reduction in dynamics of LBP regions, 4mUAB30 and 7mUAB30 could be locking the pocket into a more active conformation for coactivator binding. Similar responses of binding were seen in HDX MS studies done on LXR where the greatest protection was displayed in H3 (35). In work done with a high-affinity ligand for PPARγ LBD levels of exchange displayed helix 3 as having the strongest protection and further supporting the ligands binding properties (37). The second response to binding is the positive perturbation observed mostly for 7mUAB30 and 8mUAB30 each in complex with RXR in helices 8 and 9. R^{371}AIVLFNPDSKGLSNPAE^{388} is a peptide that spans both H8 and H9 displayed the greatest increase in dynamics.

X-ray crystallography of ligand-bound- RXRα LBD complexes requires the inclusion of coactivator peptides, usually the GRIP-1 LXXLL motif. Our analysis of

differential ligand binding to RXRα LBD before coactivator binding by HDX MS shows that there can be distinct responses to ligand binding that indicate allosteric effects at the dimer interface. For some ligands such as 7mUAB30 and 8mUAB30, rexinoid binding alone can cause a positive dynamic push towards the dimer partner. Each of these dynamic responses to ligand binding have implications for the active confirmation of RXR itself, RXR heterodimer interactions before coactivator binding, which coactivator may bind, and RXR heterodimer interactions after the coactivator are bound. Our biophysical results show how each of these steps in the RXR activation process can be different depending on which ligand is bound.

The biophysical analysis that identifies differences in ligand binding also points us towards biological questions that we can probe in our model system through genomics analysis wide. These findings provide a structural and functional map for the understanding of RXR cancer-relevant transcription. The accumulated profiles of various RXR bound agonists allow us to become predictive of what a high potency and/ or low toxicity profile looks like to guide the optimizations of chemopreventative rexinoids. The results of this work significantly further the nuclear receptor drug design process.

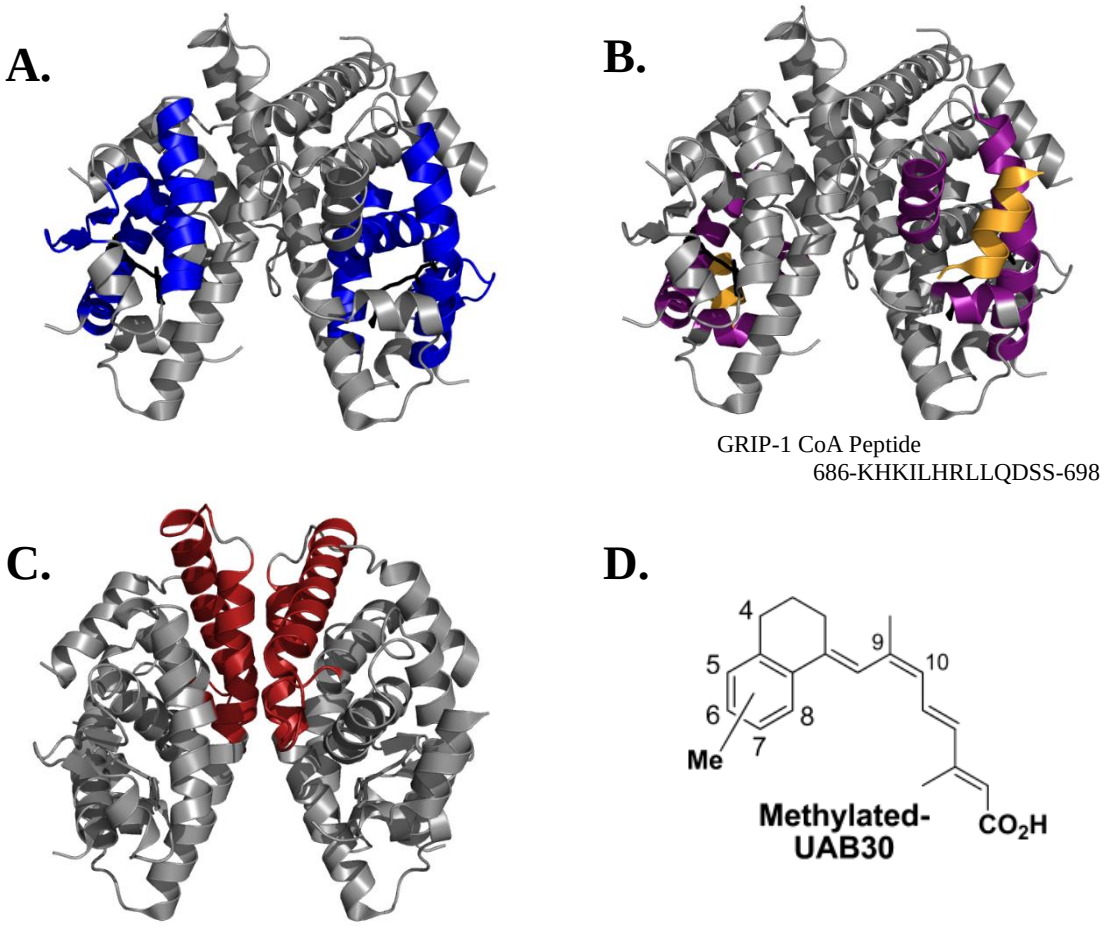

Figure 1. Structural components of RXRα-LBD homodimer in complex with UAB30 (black). (A) Helices involved in ligand binding pocket (blue). Regions in the ligand binding pocket are H3, H5, β-turn, H7, and H11. (B) Coactivator peptide (yellow) and helices in the coactivator binding pocket (purple). Helices include H3, H4, and H12. (C) Regions involved in the dimerization interface are H9, loop between H8/H9, and H11 (red). (D) Structures of methylated UAB30 derivatives. Each methyl derivative has a methyl group in the position labeled surrounding the tetralone ring. Ligands are named respectaviley: 4mUAB30, 5mUAB30, 6mUAB30, 7mUAB30, 8mUAB30.

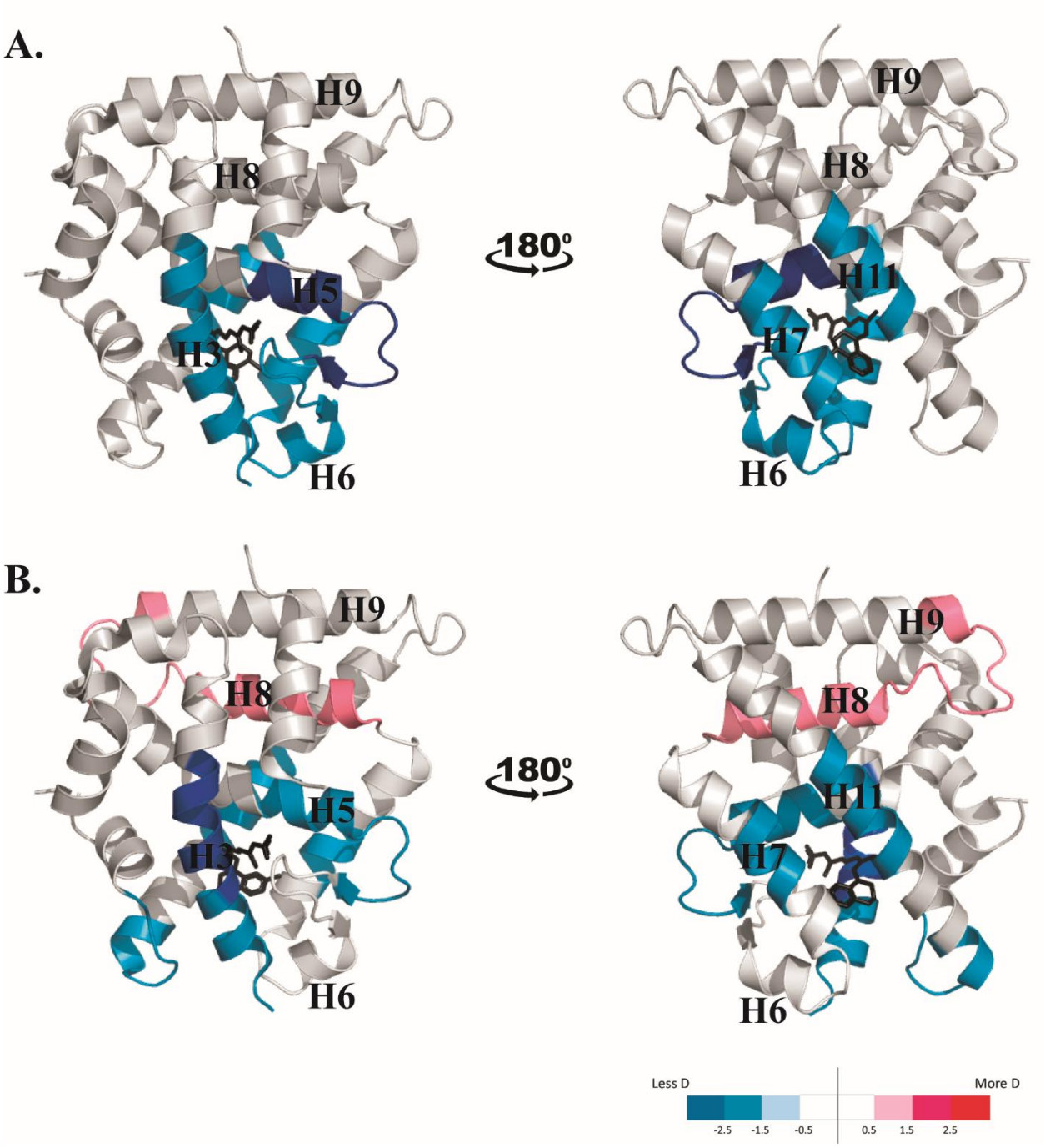

Figure 2. Differential HDX MS results mapped on X-crystal structures of RXRα-LBD in complex with hyperlipidemia inducing rexinoids. (A) Rexinoid 4mUAB30 (B) Rexinoid 7mUAB30. The change in deuterium uptake of time point 300s were overlaid onto the RXR LBD. Results are reported as an increase (shades of red) or decrease (shades of blue) in deuterium in different regions of the RXR LBD in complex with the rexinoids relative to apo-RXR LBD.

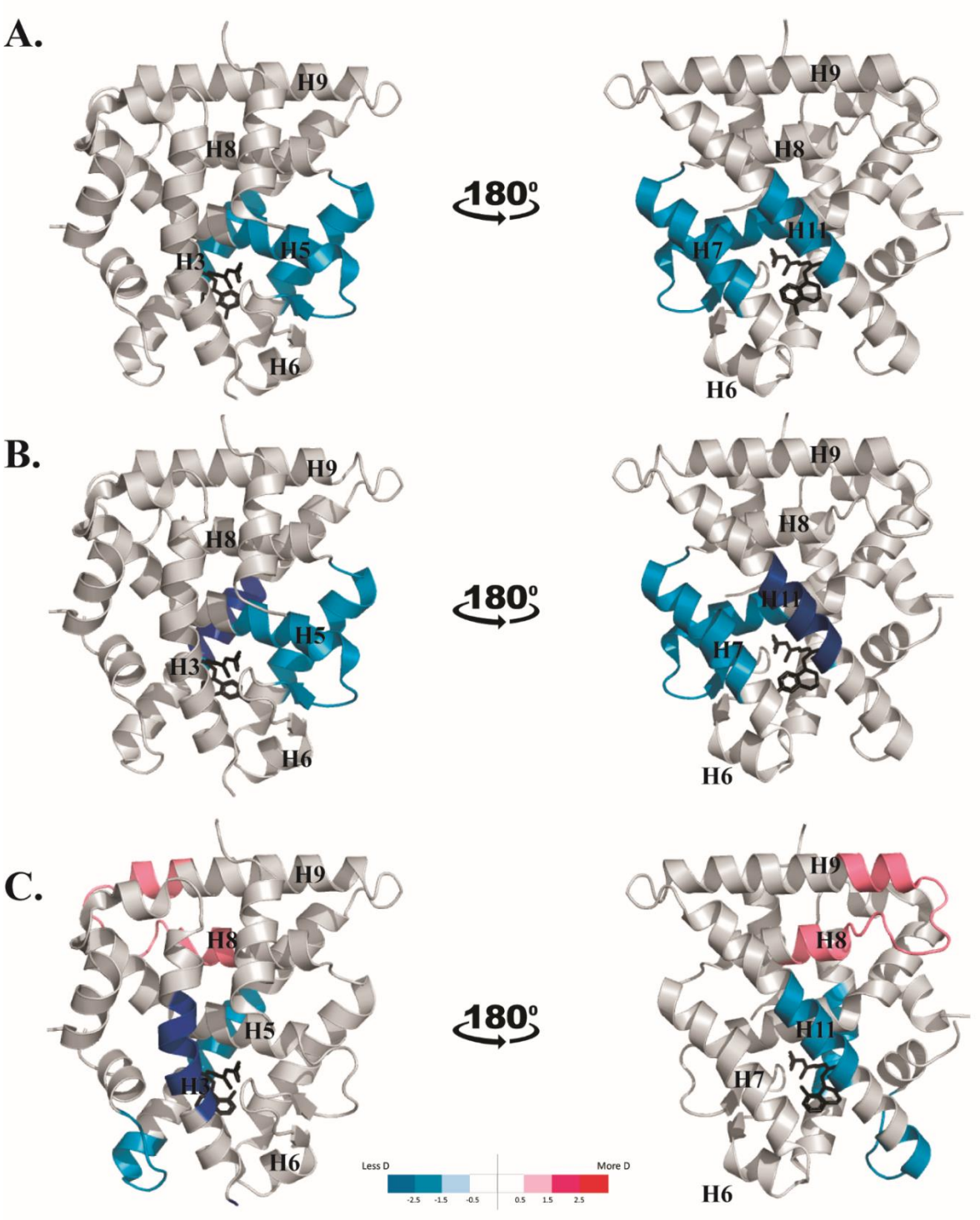

Figure 3. HDX MS results mapped on X-ray crystal structures of RXRα-LBD bound to non-toxic rexinoids. (A) 5mUAB30 (B) 6mUAB30 (C) 8mUAB30.

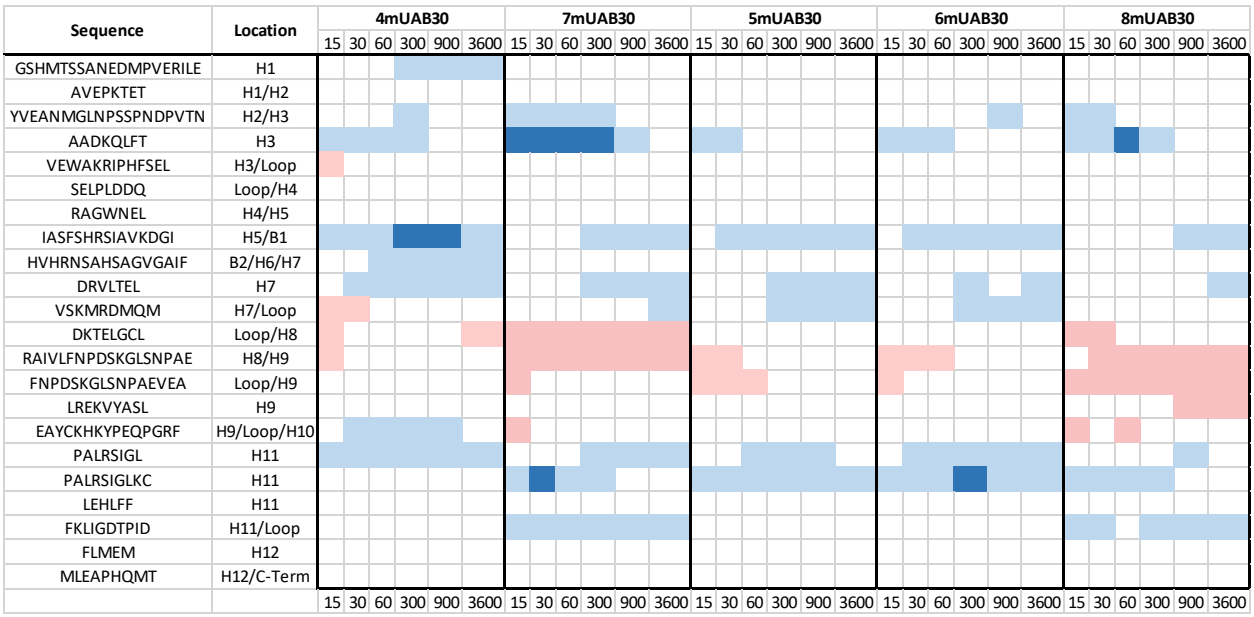

Figure 4. HDX MS difference maps of UAB30 methylated derivatives in complex with RXR LBD. ∆#D (difference from apo control) values for 5 rexinoids are plotted as a difference map according to the color at the bottom right. Each row represents a compound and each column represents a peptide. The locations of the peptides can be found directly to the left of the peptide sequence.

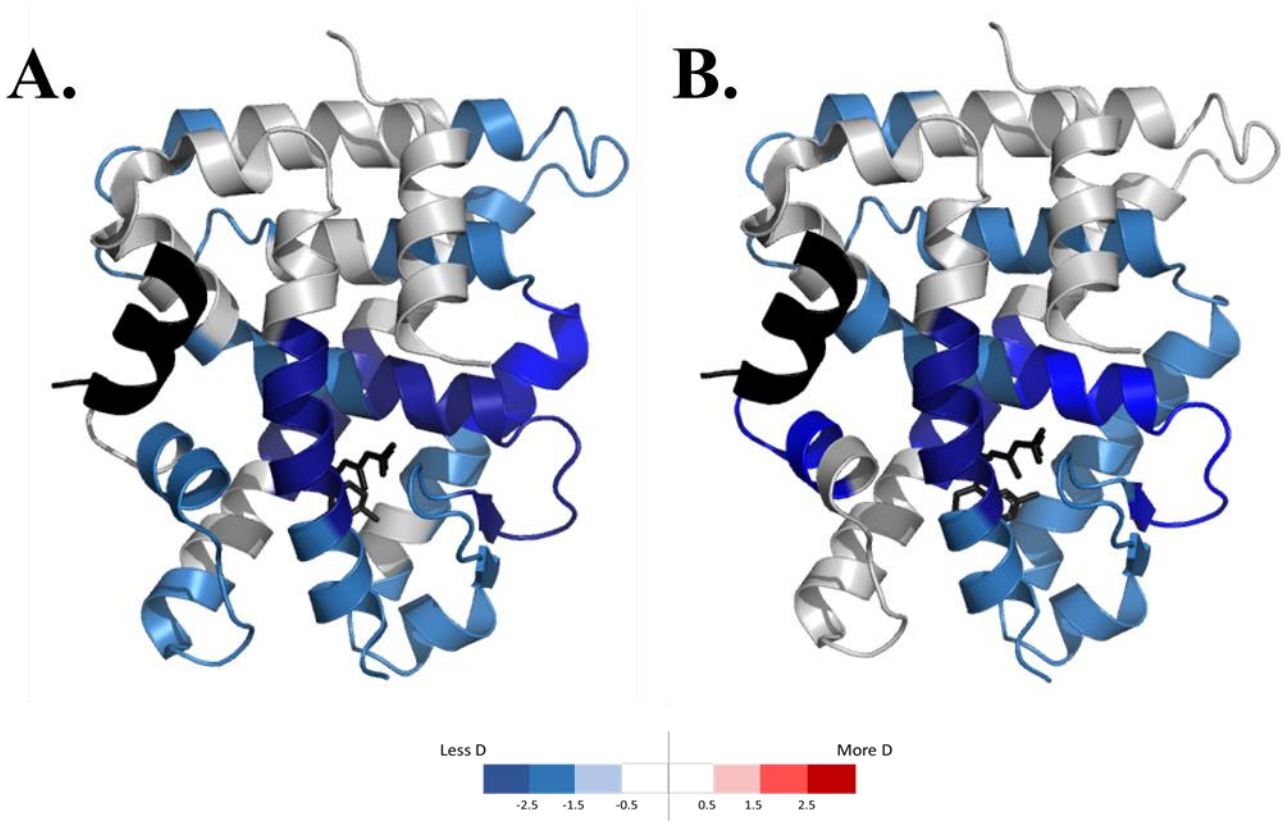

Figure 5. HDX MS data of RXR ternary structures mapped onto X-ray crystal structures. (A) RXR-4mUAB30-GRIP-1 (black) (B) RXR-7mUAB30-GRIP-1 (black)

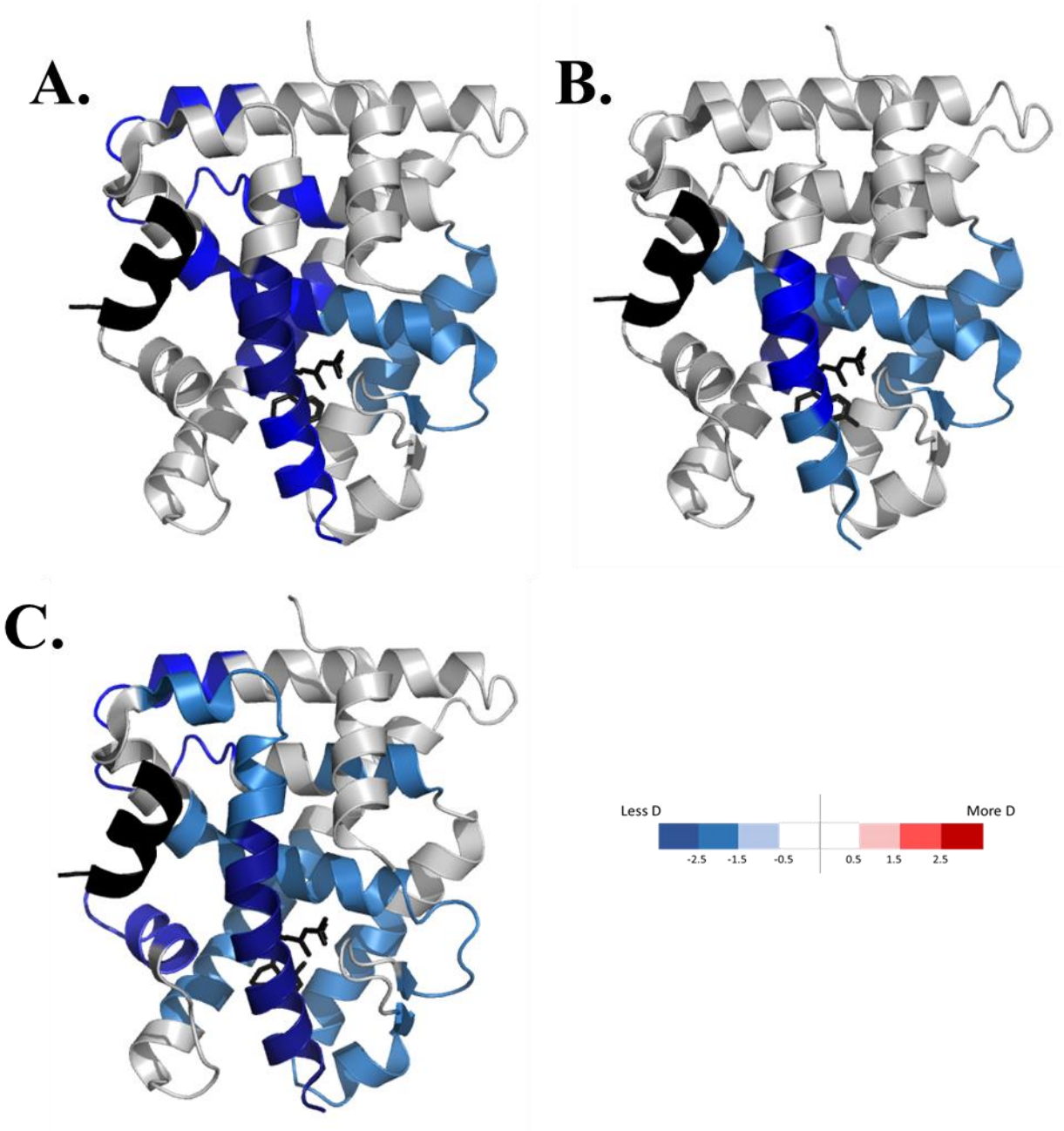

Figure 6. HDX results mapped on to RXR ternary structures. (A) RXR-5mUAB30-GRIP-1 (black) (B) RXR-6mUAB30-GRIP-1 (black) (C) RXR-8mUAB30-GRIP-1 (black)

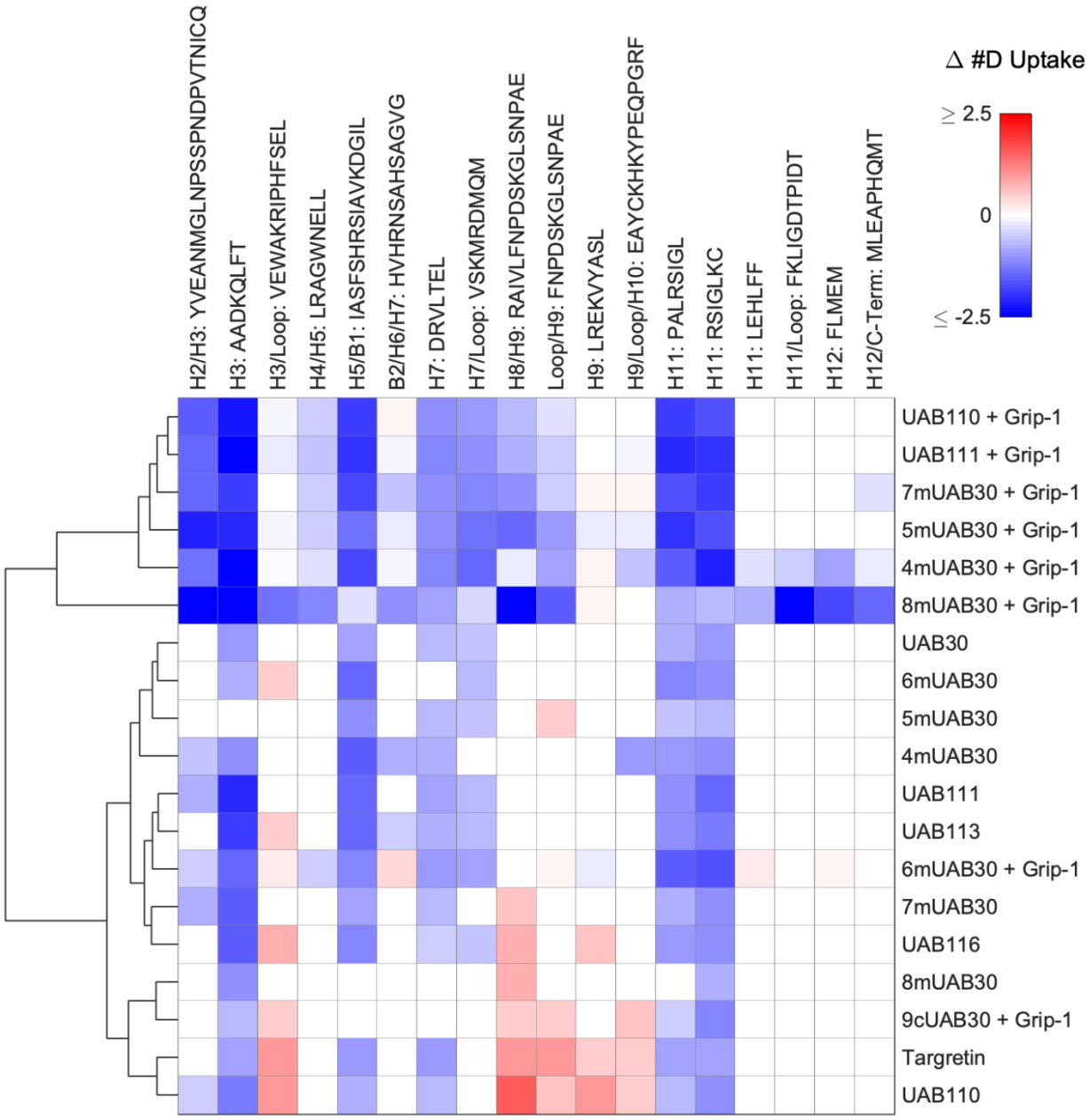

Figure 7. Independent clustering analysis of HDX MS results. Using Ward's method as the hierarchical clustering algorithm, 19 complexes were independently clustered based on their exchange profiles. Each column represents a peptide with the location labeled accordingly. The rows represent the RXR compounds which include RXR: rexinoid and RXR-rexioid-GRIP-1. The dendogram on the left linked the complexes based on their degrees of similarities.

Data Set: RXR LBD bound to UAB30 methyl derivatives	
HDX time course (sec)	15, 30, 60, 300, 900, 3600
# of peptides	138 peptides
Sequence Coverage	100%
Average peptide legnth/ redundancy	11.9/ 6.7
Replicates	3

S1. Summary table of HDX MS experiments

REFERENCES

1. Ottow, E., and Weinmann, H. (2008) Nuclear receptors as drug targets: A historical perspective of modern drug discovery. Nuclear Receptors as Drug Targets, 1-23

2. Overington, J. P., Al-Lazikani, B., and Hopkins, A. L. (2006) How many drug targets are there? Nature reviews Drug discovery 5, 993-996

3. Santos, R., Ursu, O., Gaulton, A., Bento, A. P., Donadi, R. S., Bologa, C. G., Karlsson, A., Al-Lazikani, B., Hersey, A., and Oprea, T. I. (2017) A comprehensive map of molecular drug targets. Nature reviews Drug discovery 16, 19-34

4. Mangelsdorf, D. J., and Evans, R. M. (1995) The RXR heterodimers and orphan receptors. Cell 83, 841-850

5. Sánchez-Martínez, R., Castillo, A. I., Steinmeyer, A., and Aranda, A. (2006) The retinoid X receptor ligand restores defective signalling by the vitamin D receptor. EMBO reports 7, 1030-1034

6. Heyman, R. A., Mangelsdorf, D. J., Dyck, J. A., Stein, R. B., Eichele, G., Evans, R. M., and Thaller, C. (1992) 9-cis retinoic acid is a high affinity ligand for the retinoid X receptor. Cell 68, 397-406

7. Kersten, S., Pan, L., Chambon, P., Gronemeyer, H., and Noy, N. (1995) Role of ligand in retinoid signaling. 9-cis-retinoic acid modulates the oligomeric state of the retinoid X receptor. Biochemistry 34, 13717-13721

8. Levin, A. A., Sturzenbecker, L. J., Kazmer, S., Bosakowski, T., Huselton, C., Allenby, G., Speck, J., Rosenberger, M., Lovey, A., and Grippo, J. F. (1992) 9-cis retinoic acid stereoisomer binds and activates the nuclear receptor RXRα. Nature 355, 359-361

9. Aboulafia, D. M., Norris, D., Henry, D., Grossman, R. J., Thommes, J., Bundow, D., Yocum, R. C., and Stevens, V. (2003) 9-cis-retinoic acid capsules in the treatment of AIDS-related Kaposi sarcoma: results of a phase 2 multicenter clinical trial. Archives of dermatology 139, 178-186

10. Duvic, M., Hymes, K., Heald, P., Breneman, D., Martin, A. G., Myskowski, P., Crowley, C., and Yocum, R. C. (2001) Bexarotene is effective and safe for treatment of refractory advanced-stage cutaneous T-cell lymphoma: multinational phase II-III trial results. Journal of clinical oncology 19, 2456-2471

11. Duvic, M., Martin, A. G., Kim, Y., Olsen, E., Wood, G. S., Crowley, C. A., and Yocum, R. C. (2001) Phase 2 and 3 clinical trial of oral bexarotene (Targretin capsules)

for the treatment of refractory or persistent early-stage cutaneous T-cell lymphoma. Archives of dermatology 137, 581-593

12. Straus, D. J., Duvic, M., Kuzel, T., Horwitz, S., Demierre, M. F., Myskowski, P., and Steckel, S. (2007) Results of a phase II trial of oral bexarotene (Targretin) combined with interferon alfa-2b (Intron-A) for patients with cutaneous T-cell lymphoma. Cancer 109, 1799-1803

13. Jiang, W., Deng, W., Bailey, S., Nail, C. D., Frost, A. R., Brouillette, W. J., Muccio, D. D., Grubbs, C. J., Lobo-ruppert, S. M., and Ruppert, J. M. (2009) Prevention of KLF4-mediated tumor initiation and malignant transformation by UAB30 rexinoid. Cancer biology & therapy 8, 289-298

14. Wu, L., Chaudhary, S. C., Atigadda, V. R., Belyaeva, O. V., Harville, S. R., Elmets, C. A., Muccio, D. D., Athar, M., and Kedishvili, N. Y. (2016) Retinoid X receptor agonists upregulate genes responsible for the biosynthesis of all-trans-retinoic acid in human epidermis. PLoS One 11, e0153556

15. Waseem, M., Kashyap, M. P., Li, C., Chaudhary, S. C., Chandrashekar, D. S., Atigadda, V. R., Varambally, S., Elmets, C. A., and Athar, M. (2019) Abstract LB-247: 9cis-retinoic UAB30 inhibits UVB-induced pro-inflammatory cytokines/chemokines signaling via targeting Bromodomain-4. AACR

16. Kolesar, J. M., Hoel, R., Pomplun, M., Havighurst, T., Stublaski, J., Wollmer, B., Krontiras, H., Brouillette, W., Muccio, D., and Kim, K. (2010) A pilot, first-in-human, pharmacokinetic study of 9cUAB30 in healthy volunteers. Cancer Prevention Research 3, 1565-1570

17. Atigadda, V. R., Xia, G., Desphande, A., Boerma, L. J., Lobo-Ruppert, S., Grubbs, C. J., Smith, C. D., Brouillette, W. J., and Muccio, D. D. (2014) Methyl substitution of a rexinoid agonist improves potency and reveals site of lipid toxicity. Journal of medicinal chemistry 57, 5370-5380

18. Muccio, D., Lubet, R., Atigadda, V., Brouillette, W., and Grubbs, C. (2009) Effects of methyl derivatives of the rexinoid UAB30 on methylnitrosourea (MNU) induced mammary cancers and on various indicators of toxicity. AACR

19. D Muccio, D., R Atigadda, V., J Brouillette, W., I Bland, K., Krontiras, H., and J Grubbs, C. (2017) Translation of a tissue-selective rexinoid, UAB30, to the clinic for breast cancer prevention. Current topics in medicinal chemistry 17, 676-695

20. Atigadda, V. R., Xia, G., Deshpande, A., Wu, L., Kedishvili, N., Smith, C. D., Krontiras, H., Bland, K. I., Grubbs, C. J., and Brouillette, W. J. (2015) Conformationally defined rexinoids and their efficacy in the prevention of mammary cancers. Journal of medicinal chemistry 58, 7763-7774

21. Desphande, A., Xia, G., Boerma, L. J., Vines, K. K., Atigadda, V. R., Lobo-Ruppert, S., Grubbs, C. J., Moeinpour, F. L., Smith, C. D., and Christov, K. (2014) Methyl-substituted conformationally constrained rexinoid agonists for the retinoid X receptors demonstrate improved efficacy for cancer therapy and prevention. Bioorganic & medicinal chemistry 22, 178-185

22. Grubbs, C. J., Lubet, R. A., Atigadda, V. R., Christov, K., Deshpande, A. M., Tirmal, V., Xia, G., Bland, K. I., Eto, I., and Brouillette, W. J. (2006) Efficacy of new retinoids in the prevention of mammary cancers and correlations with short-term biomarkers. Carcinogenesis 27, 1232-1239

23. Marayati, R., Williams, A. P., Bownes, L. V., Quinn, C. H., Stewart, J. E., Mroczek-Musulman, E., Atigadda, V. R., and Beierle, E. A. (2020) Novel retinoic acid derivative induces differentiation and growth arrest in neuroblastoma. Journal of pediatric surgery 55, 1072-1080

24. Bayeva, N., Coll, E., and Piskareva, O. (2021) Differentiating neuroblastoma: A systematic review of the retinoic acid, its derivatives, and synergistic interactions. Journal of Personalized Medicine 11, 211

25. Beinsteiner, B., Markov, G. V., Erb, S., Chebaro, Y., McEwen, A. G., Cianférani, S., Laudet, V., Moras, D., and Billas, I. M. (2021) A structural signature motif enlightens the origin and diversification of nuclear receptors. PLoS Genetics 17, e1009492

26. Miller, M. D., and Phillips, G. N. (2021) Moving beyond static snapshots: Protein dynamics and the Protein Data Bank. Journal of Biological Chemistry 296

27. Engen, J. R. (2009) Analysis of protein conformation and dynamics by hydrogen/deuterium exchange MS. ACS Publications

28. Morgan, C. R., and Engen, J. R. (2009) Investigating solution-phase protein structure and dynamics by hydrogen exchange mass spectrometry. Current protocols in protein science 58, 17.16. 11-17.16. 17

29. Boerma, L. J., Xia, G., Qui, C., Cox, B. D., Chalmers, M. J., Smith, C. D., Lobo-Ruppert, S., Griffin, P. R., Muccio, D. D., and Renfrow, M. B. (2014) Defining the communication between agonist and coactivator binding in the retinoid X receptor α ligand binding domain. Journal of Biological Chemistry 289, 814-826

30. Xia, G., Boerma, L. J., Cox, B. D., Qiu, C., Kang, S., Smith, C. D., Renfrow, M. B., and Muccio, D. D. (2011) Structure, energetics, and dynamics of binding coactivator peptide to the human retinoid X receptor α ligand binding domain complex with 9-cis-retinoic acid. Biochemistry 50, 93-105

31. Senicourt, L., Le Maire, A., Allemand, F., Carvalho, J. E., Guee, L., Germain, P., Schubert, M., Bernadó, P., Bourguet, W., and Sibille, N. (2021) Structural insights into

the interaction of the intrinsically disordered co-activator TIF2 with retinoic acid receptor heterodimer (RXR/RAR). Journal of molecular biology 433, 166899

32. Chandra, V., Wu, D., Li, S., Potluri, N., Kim, Y., and Rastinejad, F. (2017) The quaternary architecture of RARβ–RXRα heterodimer facilitates domain–domain signal transmission. Nature communications 8, 1-9

33. Zhang, J., Chalmers, M. J., Stayrook, K. R., Burris, L. L., Wang, Y., Busby, S. A., Pascal, B. D., Garcia-Ordonez, R. D., Bruning, J. B., and Istrate, M. A. (2011) DNA binding alters coactivator interaction surfaces of the intact VDR–RXR complex. Nature structural & molecular biology 18, 556-563

34. SAKamenecka, B. (2007) Partial agonists activate PPARgamma using a helix 12 independent mechanism. Structure 15, 12581271

35. Belorusova, A. Y., Evertsson, E., Hovdal, D., Sandmark, J., Bratt, E., Maxvall, I., Schulman, I. G., Åkerblad, P., and Lindstedt, E.-L. (2019) Structural analysis identifies an escape route from the adverse lipogenic effects of liver X receptor ligands. Communications biology 2, 1-13

36. Onate, S. A., Tsai, S. Y., Tsai, M.-J., and O'Malley, B. W. (1995) Sequence and characterization of a coactivator for the steroid hormone receptor superfamily. Science 270, 1354-1357

37. Zheng, J., Corzo, C., Chang, M. R., Shang, J., Lam, V. Q., Brust, R., Blayo, A.-L., Bruning, J. B., Kamenecka, T. M., and Kojetin, D. J. (2018) Chemical crosslinking mass spectrometry reveals the conformational landscape of the activation helix of PPARγ; a model for ligand-dependent antagonism. Structure 26, 1431-1439. e1436

CHAPTER IV
STABILITY OF THE RETINOID X RECEPTOR-A HOMODIMER IN THE PRESENCE AND ABSENCE OF REXINOID AND COACTIVATOR PEPTIDE

by

ZHENGRONG YANG, DONALD D. MUCCIO, NATHALIA MELO, VENKATRAM R. ATIGADDA, AND MATTHEW RENFROW

Biochemistry 2021, 60, 15, 1165–1177

Format adapted and errata corrected for dissertation

ABSTRACT

Differential scanning calorimetry and differential scanning fluorimetry were used to measure the thermal stability of human retinoid X receptor-α ligand binding domain (RXRα LBD) homodimer in the absence or presence of rexinoid and coactivator peptide, GRIP-1. The apo-RXRα LBD homodimer displayed a single thermal unfolding transition with a Tm of 58.7 °C and an unfolding enthalpy (ΔH) of 673 kJ/mol (12.5 J/g), much lower than average value (35 J/g) of small globular proteins. Using a heat capacity change (ΔCp) of 15 kJ/(mol K) determined by measurements at different pH values, the free energy of unfolding (ΔG) of the native state was 33 kJ/mol at 37 °C. Rexinoid binding to the apo-homodimer increased Tm by 5 to 9 °C and increased the ΔG of the native homodimer by 12 to 20 kJ/mol at 37 °C, consistent with the nanomolar dissociation constant (Kd) of the rexinoids. GRIP-1 binding to holo-homodimers containing rexinoid resulted in additional increases in ΔG of 14 kJ/mol, a value that was the same for all three rexinoids. Binding of rexinoid and GRIP-1 resulted in a combined 50% increase in unfolding enthalpy, consistent with reduced structural fluidity and more compact folding observed in other published structural studies. The complexes of UAB110 and UAB111 are each more stable than the UAB30 complex by 8 kJ/mol due to enhanced hydrophobic interactions in the binding pocket because of their larger end groups. This increase in thermodynamic stability positively correlates with their improved RXR activation potency. Thermodynamic measurements are thus valuable in predicting agonist potency.

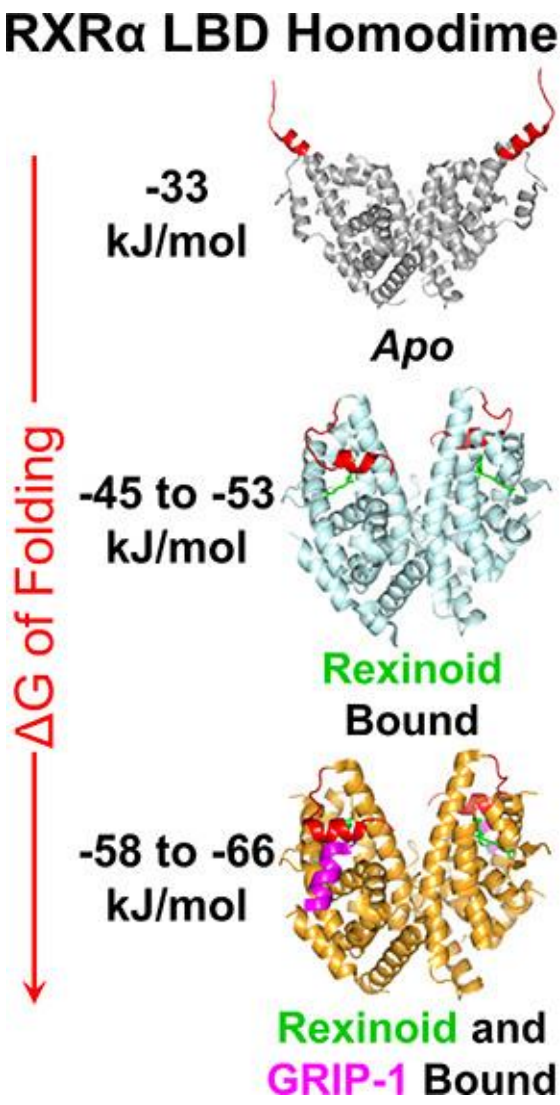
RXRα LBD Homodimer
ΔG of Folding
-33 kJ/mol
Apo
-45 to -53 kJ/mol
Rexinoid Bound
-58 to -66 kJ/mol
Rexinoid and GRIP-1 Bound

INTRODUCTION

Human retinoid X receptors (RXRα, RXRβ, and RXRγ) play a key role in many signaling processes which control cellular proliferation, differentiation, and growth in epithelial tissue as well as maintain proper lipid and glucose homeostasis.1 The three RXR isotypes each display different functions in modulating gene transcription of target genes.2 The proteins are approximately 51 kDa and contain two folded domains and three flexible, largely unstructured regions. The DNA binding domain (DBD) binds to specific DNA sequences at the start of target genes3 using two Zn-finger motifs. The ligand binding domain (LBD) at the c-terminal end of RXR is responsible for ligand recognition as well as the associated conformational changes that promote recruitment of coactivator proteins (with replacement of corepressor proteins) important for stabilizing RNA polymerase II to start transcription. The LBD of RXR is connected to the DBD by a short unstructured linker region largely separating the two functions of RXR: specific recognition of target genes and ligand-induced activation of the target gene. Both DBD and LBD contribute to the dimerization interface of the receptor.

The X-ray crystal structures of RXR LBD homodimers alone (apo-RXR LBD) or bound to a variety of ligand agonists (holoRXR LBD) and coactivator peptides revealed the significant conformational changes that allow for agonist-induced transcriptional activation.4−14 In apo-RXRα LBD, helix 12 extends away from the core of the domain (Figure 1D) whereas, in the complexes, helix 12 reorients and folds back toward the ligand binding pocket (LBP). Molecular interactions, which occur between the LXXLL15 motif of the coactivator peptide and helices 3, 4, and 12, stabilize the active conformation only observed in the presence of agonists (Figure 1D). The tertiary

structural changes induced by coactivator peptide binding also extend to helix 11 residues that interact directly with the agonists. Hydrogen−deuterium exchange mass spectrometry (HDX-MS) and fluorescence polarization studies strongly support that helix 12 is dynamic in both apo- and holohomodimers and only stabilized when both the coactivator peptide and the agonist are present.8,9,16−18 Recent X-ray and HDX-MS studies19−23 of nuclear receptor heterodimers containing the entire RXR bound to double stranded DNA with a target recognition site support the validity of those structural and dynamical conclusions drawn from studies on RXRα LBD homodimers.

Our group has designed and studied many rexinoids for the use in cancer treatment and prevention.13,14,24−27 UAB30 (Figure 1B) is a novel rexinoid developed by our group currently in phase II clinical trials. Compared to Targretin, the only clinically used rexinoid approved by the FDA,28 UAB30 exhibits high efficacy in cancer prevention without inducing hyperlipidemia which is the dose-limiting toxicity of Targretin.25,29−32 UAB110 and UAB111 (Figure 1B) are two rexinoids belonging to another structural class of UAB rexinoids other than UAB30. Each of these three UAB rexinoids bind the RXRα LBD with nanomolar affinities. UAB110 and UAB111 exhibit potencies approximately 40-fold higher than UAB30 in RXR transcriptional activation.14 However, UAB111 induces hyperlipidemia at its effective dose, while UAB110 does not increase triglyceride levels.

To design more potent and nontoxic rexinoids with greater clinical potential and selectivity, we need to fully understand the interactions between the rexinoids and RXRα LBD, and their effects on the structure and dynamics of the RXR homodimers and heterodimers with other nuclear receptors. Xray crystal structures of RXRα LBD in

complex with each UAB rexinoid and a coactivator peptide, GRIP-1 (e.g., RXRα LBD:UAB30:GRIP-1 complex in Figure 1), revealed that only subtle structural differences occurred in the LBP, but there was essentially no difference in the overall backbone fold of the homodimer (Figure 1E).8,9,13,14,33 Using isothermal titration calorimetry (ITC), we showed that GRIP-1 binds to holo-RXR LBD homodimers in complex with each UAB rexinoid with nearly identical affinity and similar enthalpic and entropic signatures.8,9,13,14 The binding thermodynamics of rexinoids to RXR LBD in the absence of coactivator peptide have not been determined, because of limitations to the applicability of ITC in such systems of high-affinity, hydrophobic ligands with small binding enthalpy changes.34,35 Differential scanning calorimetry (DSC) provides an alternative method to obtain thermodynamic data on ligand binding. From the differences in the unfolding temperature and enthalpy with and without a ligand, the thermodynamic parameters of binding of the ligand are determined.36,37

Using DSC, we conducted in this study a complete thermodynamic analysis of the thermal unfolding of human RXRα LBD homodimer in the absence or presence of rexinoid and the coactivator peptide, GRIP-1. The goal was to understand how rexinoids and coactivator peptides modulate the energetics of this protein domain, and to gain knowledge on the thermodynamic parameters of interaction between rexinoids and apo-RXRα LBD. Differential scanning fluorimetry (DSF), a complementary thermal unfolding method to DSC, was used to inform on key aspects of the unfolding of the domain and to rapidly scan unfolding conditions. We obtained the full panel of unfolding thermodynamic parameters on apoRXRα LBD, including unfolding temperature (Tm), enthalpy (ΔH), entropy (ΔS), and heat capacity change (ΔCp u).

These parameters are essential for analyzing binding energetics of agonists and coactivators to RXR but have never been reported before. From the DSC data obtained in the presence of UAB rexinoids and/or GRIP-1, we calculated the thermodynamic parameters of UAB rexinoids binding to apo-RXRα LBD homodimer, which clearly demonstrated for the first time that rexinoid binding was an entropically driven process and correlated well with rexinoid potency as agonists. We also calculated thermodynamic parameters of GRIP-1 binding to holo-RXRα LBD homodimers containing the rexinoids. They corresponded closely to those determined by ITC, which demonstrated the validity of this approach. Thermal unfolding of RXRα LBD homodimer was not completely reversible, and we provided a general guideline on how to deal with this complication to gather meaningful thermodynamic values of ligand binding.

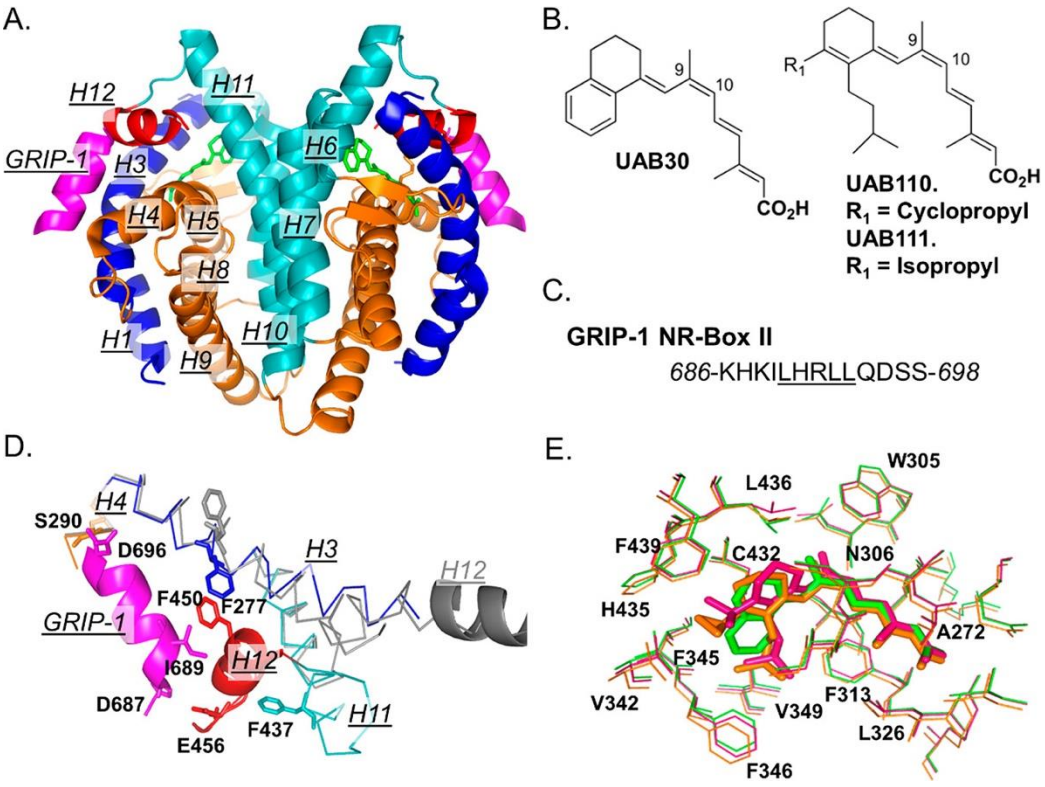

Figure 1**.** Structures of RXRα LBD, rexinoids, and coactivator peptide. (A) Crystal structure of RXRα LBD homodimer in complex with UAB30 and GRIP-1 (PDB ID: 4K4J). Secondary elements of each dimer are colored according to their positions in the three-layer helical sandwich: helices 1 and 3 are blue; helices 4, 5, 8, and 9 and the β-sheets orange; and helices 6, 7, 10, and 11 teal. Helices 12, which change conformation upon GRIP-1 binding, are red. GRIP-1 peptides are pink. UAB30 rexinoids are displayed as green sticks. (B) Chemical structures of UAB30, UAB110, and UAB111. (C) Peptide sequence of GRIP-1 NR-Box II coactivator peptide. (D) Conformations of helices 3 (blue), 11 (teal), and 12 (red) in the complex, in comparison with their positions in apo-RXRα LBD (gray, PDB ID: 6HN6). (E) Conformations of UAB30 (green), UAB110 (orange), and UAB111 (deep pink) in the ligand binding pocket of RXRα LBD. The rexinoids are displayed as sticks. The amino acid residues lining the pocket are displayed as thin lines.

MATERIALS AND METHODS

Protein Purification

Overexpression and purification of human RXRα LBD (amino acid residues T223−T462) were performed as described by Xia et al.9 Briefly, the His6-tagged RXRα LBD fusion protein was purified using a HiTrap Nichelating column (GE Healthcare,

Piscataway, NJ), and the His6-tag was removed by incubating with human α-thrombin overnight. The complete removal of His6-tag was confirmed by MALDI-TOF mass spectrometry. The tagless RXRα LBD was further purified on a HiLoad Superdex 75 size exclusion column (SEC, GE Healthcare, Piscataway, NJ). The fractions containing RXRα LBD homodimers or tetramers (Figure S1A) were pooled separately. SDS-PAGE and MALDI were used to establish a purity of >95% and a mass of the monomers at 27 283 Da.

Fluorescence-Based Binding Affinity Assay

The dissociation constant (Kd) of the rexinoids binding to apoRXRα LBD was determined in a fluorescence-based binding assay as previously described.24 The fluorescence quenching data were plotted in Origin 7 (OriginLab, LLC.), and nonlinear least-squares curve fitting was performed to obtain an apparent Kd based on the following equation:

$$\%\text{quenching} = 100\,(1 - Z)\,(2R_t) / \{(N_t + R_t + K_d) + [\,(N_t + R_t + K_d)^{2} - 4N_tR_t\,]^{1/2}\}$$

where Rt was the total concentration of the test rexinoid, Nt was the total concentration of apo-RXRα LBD in monomer unit, and Z represented the residual unquenched % fluorescence after the binding site was completely saturated. Nt was determined from the binding curve of UAB111 which had the highest binding affinity. This value was fixed for fitting of UAB30 and UAB110 binding curves.

Differential Scanning Calorimetry

Calorimetry experiments were performed using the VP-Capillary DSC system (Malvern Instruments, Westborough, MA) in 0.130 mL cells at a heating rate that varied between of 0.5 and 4 °C/min. An external pressure of 2.0 atm was maintained to prevent possible degassing of the solutions upon heating. Purified apo-RXRα LBD homodimer freshly eluted from SEC was dialyzed in 2 L of DSC buffer (10 mM sodium phosphate, pH 7.0, 50 mM NaCl, 0.5 mM EDTA, and 1 mM TCEP; sodium phosphate was replaced by sodium borate for pH 8.5−9.5) for >4 h and used within 24 h. Holo-RXRα LBD homodimers were prepared by adding rexinoids from a 100-fold concentrated stock in DMSO into apo-RXRα LBD homodimer. The samples were incubated at 22 °C for 10 min and protected from light. GRIP1 was added into the holo-RXRα LBD homodimers from a 10 mM stock solution in water. To prepare the buffer control, identical amounts of rexinoid and GRIP-1 were added into the dialysis buffer. DSC data analyses were performed using the built-in analysis module in Origin 7 provided by the DSC manufacturer.39 Briefly, after subtraction of the buffer scan, and normalization to molar heat capacity (Cp), a cubic baseline was subtracted from the molar Cp curve to set the pre- and posttransition baselines to zero (Figure S2). The thermal unfolding temperature (Tm) was determined from the maximum of the Cp curve. The calorimetric enthalpy (ΔHc) was obtained by integrating the Cp curve. The apparent van't Hoff enthalpy (ΔHv) was obtained by fitting the curve to a built-in model, MN2STATE, which fit ΔHv independently of ΔHc (Figure S3). Equations for the calculation of thermodynamic parameters are listed in Appendix I of the Supporting Information.

Differential Scanning Fluorimetry

Using the Prometheus NT.48 instrument (NanoTemper Technologies, LLC, South San Francisco, CA) with 48 capillary chambers, each sample was excited at 290 nm, and emission was detected simultaneously at 330 and 350 nm. The first derivative of the fluorescence signal at 350 nm relative to 330 nm (F350/F330) versus temperature produced a DSC-like thermogram. The first derivative of fluorescence intensity at each wavelength exhibited the same thermal unfolding profiles. Because the UV−vis absorption of the rexinoids interfered with the detection of unfolding using F350/F330, DSF data of fluorescence intensity at 350 nm were used to obtain Tm. Sample preparation for DSF was the same as for DSC. Each capillary required 10 μL to load. Duplicate measurements were performed on each sample. Tm of each sample was automatically determined by the built-in analysis software and tabulated in an Excel output file. Global curve fitting of the apo-RXRα LBD DSF data obtained at different scan rates was performed using previously published equations40 written in Origin C.

Circular Dichroism

CD spectra were recorded in an OLIS CD spectrophotometer (OLIS, Athens, GA). Quartz cuvettes with a path-length of 0.02 cm were used. The protein concentration was 12 μM dimer. The CD cell holder was heated using an external water bath to the desired temperatures. CD spectra were recorded from 260 to 190 nm. Buffer baselines were recorded at the same temperatures and subtracted from the protein spectra. Total data collection time was ~5 min for each spectrum. The secondary structural content was determined by the CDNN program (CDNN: CD Spectra Deconvolution, Version 2.1, Universität Böhm, 1997). For the completely denatured

sample in guanidine− HCl, the sample was prepared by adding guanidine−HCl as a solid into the thermally unfolded protein solution to reach a final concentration of 5 M. The sample was then cooled in the cell holder, and the CD spectra were collected at 25 °C. The final protein concentration was adjusted based on the volume change after the addition of the denaturant. Optical interference from the denaturant prevented scans below 210 nm.

Isothermal Titration Calorimetry

ITC experiments were performed on an Auto-iTC200 system (Malvern Instruments, Westborough, MA). The buffer used in ITC was the DSC buffer (pH 7.0) with 1% w/v DMSO. For titration of UAB30 with apo-RXRα LBD, the ITC sample cell contained 5 μM UAB30 (titrand), and the syringe contained 20 μM apo-RXRα LBD homodimer (titrant). For titration of RXRα LBD:rexinoid with GRIP-1, the titrand was 12.5 μM RXRα LBD dimer and 35 μM test rexinoid, and the titrant was 350 μM GRIP-1. Each titration experiment consisted of 16 injections of 2.5 μL of titrant into titrand at 10, 20, or 30 °C. Background mixing heat was determined from injections of titrant into the same buffer without titrand. Data analysis was performed using the built-in analysis module in Origin 7 provided by the ITC manufacturer. Monomeric protein concentration was used for analysis to obtain the stoichiometry of binding to each RXRα LBD monomer.

RESULTS AND DISCUSSION

Thermal Unfolding of Apo-RXRα LBD Homodimers

The ΔG of apo-RXRα LBD unfolding at 30 °C was previously determined by Harder et al.41 using isothermal chemical denaturation. However, the enthalpic

and entropic changes of the unfolding process were not obtained, nor was the unfolding heat capacity change which contributes significantly to the temperature dependence of ΔG.

Partial Reversibility of Transition

To determine the stability of apo-RXRα LBD homodimer at 37 °C and other temperatures, thermal unfolding of this homodimer was measured by DSC from 35 to 70 °C using a scan rate (v) of 4 °C/min.

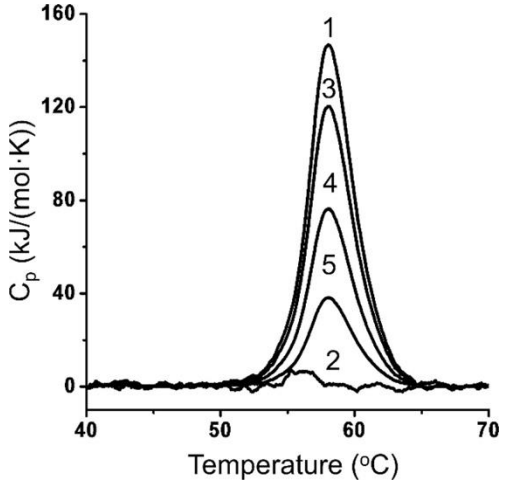

Figure 2. Thermal unfolding of *apo*-RXRα LBD is partially reversible. DSC molar heat capacity profile of 1.5 μM *apo*-RXRα LBD homodimer. (1) First scan; (2) rescan; (3) after heating at 57.3 °C for 1 min; (4) after heating at 58.6 °C for 1 min; and (5) after heating at 60.0 °C for 1 min.

A single endotherm was observed centered at the maximum thermal unfolding temperature (Tm) of 58.2 ± 0.1 °C, with a calorimetric unfolding enthalpy (ΔHc) of 665 ± 4 kJ/mol (Figure 2, trace 1). Upon rescan, no thermal unfolding endotherm was observed, indicating that the unfolding of the homodimer was irreversible when heated to 70 °C (Figure 2, trace 2). To determine whether partial

reversibility occurred during the unfolding process, the extent of reversibility at various points through the DSC endotherm was examined by consecutive scans of the same homodimer sample from 35 °C to various ending temperatures (Figure S4). DSC endotherms were also obtained on homodimers systematically heated for 1 min at various temperatures and then rapidly cooled in an ice bath. When the incubation temperature was 57.3 °C, which corresponded to 25% unfolding [the extent of unfolding at temperature T was determined by the ratio of integrated area from 35 °C to T, divided by the total area under the DSC curve], an endotherm was observed with the same Tm, but with approximately 80% the intensity of the first scan (Figure 2, trace 3). As the incubation temperature was increased to 58.2 °C (50% unfolding), the ΔHc was decreased to 50% (Figure 2, trace 4). The ΔHc was further decreased to 30% when the incubation temperature was increased to 60.0 °C (75% unfolding, Figure 2, trace 5). These data support that the unfolding of the homodimer was partially reversible through the endotherm.

The scan rate dependence of the thermal unfolding of apoRXRa LBD was next examined. The scan rate, v, of the DSC measurement was decreased from 4.0 to 0.5 °C/min. As displayed in Figure 3A and summarized in Table 1, Tm decreased systematically as v decreased, reaching 55.6 ± 0.1 °C when v was 0.5 °C/min. ΔHc remained nearly constant at 670 kJ/mol regardless of v. An apparent van't Hoff enthalpy (ΔHv) was determined by nonlinear least-squares curve fitting to a two-state model, whereby a natively folded protein, N, unfolds reversibly to U: N ↔ U.42 ΔHv systematically increased from 815 ± 13 kJ/mol when v was 4 °C/min to 1208 ± 4 kJ/mol when v was 0.5 °C/min.

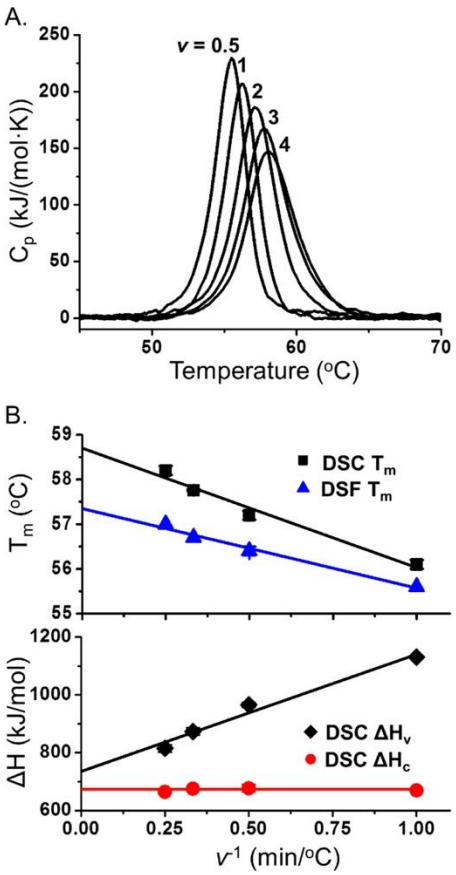

Figure 3. Equilibrium unfolding parameters of apo-RXRα LBD obtained by extrapolation to infinite scan rate. (A) DSC molar heat capacity profiles for 1.5 μM apo-RXRα LBD homodimer at different scan rates, v (from left to right): 0.5, 1.0, 2.0, 3.0, and 4.0 °C/min. (B) Tm, ΔHc, and ΔHv as a function of v−1 . The Tm and ΔHv values were fitted linearly to v −1 . The equilibrium unfolding parameters were obtained by extrapolation to zero v−1 .

scan rate	DSC			DSF[a]
v (°C/min)	T_m (°C)	ΔH_c (kJ/mol)	ΔH_v (kJ/mol)	T_m (°C)
0.5	55.6 ± 0.1	681 ± 4	1208 ± 4	55.2 ± 0.1
1	56.1 ± 0.1	669 ± 1	1133 ± 4	55.6 ± 0.1
2	57.2 ± 0.1	677 ± 13	966 ± 8	56.4 ± 0.1
3	57.8 ± 0.02	677 ± 1	874 ± 13	56.7 ± 0.1
4	58.2 ± 0.1	665 ± 4	815 ± 13	57.0 ± 0.1
infinite[b]	58.7 ± 0.2	673 ± 8	736 ± 25	57.4 ± 0.1

[a] T_m measured from DSF monitored at 350 nm. [b] Extrapolation to v^{-1} is 0 yielded the equilibrium unfolding parameters.

Table 1. Scan Rate Dependence of the Thermal Unfolding Parameters of *apo*-RXRα LBD

The thermal unfolding of apo-RXRα LBD was also monitored by measuring the changes in intrinsic fluorescence at 330 and 350 nm (Figure S5). The changes in tryptophan (Trp) emission intensity at 330 or 350 nm reflected the change in Trp environments during unfolding. The differential scanning fluorimetry (DSF) curves of apo-RXRα LBD, which contains two Trp residues, displayed only one unfolding transition that was similar to the DSC endotherms. The trends in the Tm at different scan rates matched those determined by DSC (Table 1), suggesting that both DSC and DSF detected the same global unfolding event. The Tm values determined by DSF were systematically lower than the Tm measured by DSC by ∼1 °C. The lower Tm measured by DSF relative to those by DSC was observed for other protein unfolding processes.43−45 Trp residues in folded states may sense changes in their local environments at a slightly lower temperature than onset of the global unfolding measured calorimetrically.46 The lack of reversible unfolding transition in DSC rescans and the dependence of Tm on v indicated that the thermal unfolding of RXRα LBD was not in complete equilibrium throughout the heating process. DSC irreversibility is a common phenomenon, especially for multidomain or oligomeric proteins.47 Often protein aggregation occurs at higher temperatures, which prevents reversibility.48 However, these irreversible DSC transitions yield equilibrium data if the unfolding follows the Lumry−Eyring model: whereby N unfolds reversibly to U, which converts to a denatured state (D) slowly and irreversibly: $N \leftrightarrow U \rightarrow D$.49−51 If the irreversible step occurs slower than the rate of protein unfolding and refolding, then thermodynamic data for the reversible step are obtained by extrapolation of measured data to infinite scan

rate.47,50−54 For apo-RXRα LBD, the Tm and ΔHv were plotted versus v−1 (Figure 3B); each thermal parameter was linearly dependent on v−1 for v faster than 0.5 °C/min. The extrapolated equilibrium unfolding parameters (Table 1) were as follows: Tm eq = 58.7 ± 0.2 °C, ΔHv eq = 736 ± 25 kJ/mol, and ΔHc eq = 673 ± 8 kJ/mol (using the average of the apparent ΔHc at different v values).

Two-State Unfolding without Dimer Dissociation

The ratio of the van't Hoff enthalpy to the calorimetric enthalpy, ΔHv eq /ΔHc eq, was essentially 1 using the extrapolated parameters. A cooperative unit of 1 when both ΔHc eq and ΔHv eq were determined based on per mole of dimer indicated that the native dimer was the cooperative unfolding unit. The ratio of 1 for ΔHv/ΔHc was not expected if the dimeric protein dissociated during unfolding: N2 ↔ 2U. For this unfolding equilibrium, the unfolding endotherm is asymmetrical about its midpoint, and the apparent ΔHv/ΔHc is about 0.754 (see Figure S6 for a simulated DSC transition based on the N2 ↔ 2U model, in comparison to the N ↔ U model). The asymmetry and low ΔHv/ΔHc were not observed in any of the DSC traces obtained in this study, suggesting that the native dimer unfolded without significant dissociation to monomers.55−57

To examine this further, native gels were used to determine the aggregation state of the homodimer at three different temperatures: 57 °C which was below Tm, 58.7 °C which was the extrapolated equilibrium Tm, and 65 °C which was above the completion of the endotherm. As displayed in Figure 4, apo-RXRα LBD

homodimer migrated near 50 kDa, consistent with a dimer, whereas the tetramer migrated near 100 kDa.

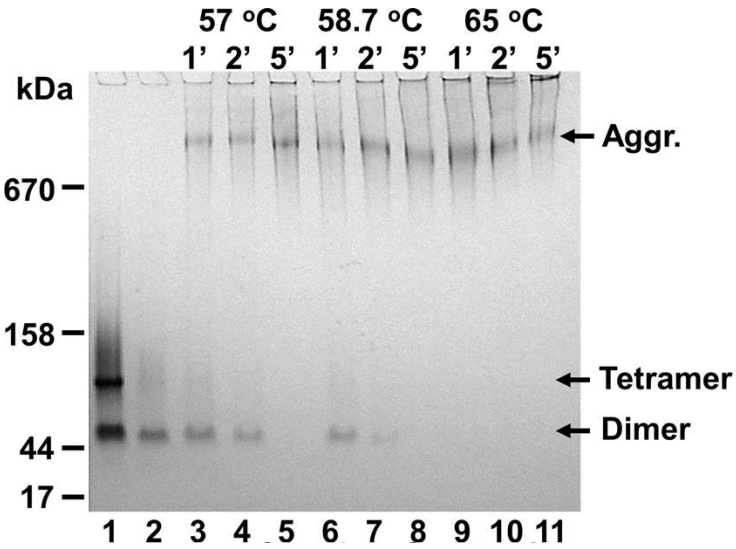

Figure 4. Changes in apo-RXRα LBD aggregation state during thermal unfolding. Native PAGE of 5 μM apo-RXRα LBD homodimer incubated at different temperatures for 1, 2, and 5 min, and then rapidly cooled in an ice bath. Lane 1: Fraction from SEC containing a mixture of tetramer and dimer that was not heated. Lane 2: Fraction from SEC containing only dimer that was not heated. Lanes 3−5: dimer heated at 57 °C (~25% unfolding) for 1, 2, and 5 min. Lanes 6−8: dimer heated at 58.7 °C (50% unfolding) for 1, 2, and 5 min. Lanes 9−11: dimer heated at 65 °C (past 100% unfolding) for 1, 2, and 5 min.

When the dimer was heated at 57 °C for 1, 2, and 5 min and rapidly cooled in an ice bath, the band corresponding to the dimer was observed, but the intensity decreased as heating time increased. In addition, a species that migrated significantly above that of the unheated dimer emerged and increased in intensity, consistent with an aggregate of much higher molecular weight. When the heating temperature increased to 58.7 °C, less dimer and more aggregated species were observed. When heated to 65 °C for these times, the dimer disappeared, and only a highly aggregated species was present in the native gels. A band consistent with monomer was not observed in any lane.

Circular dichroism (CD) and fluorescence spectroscopy were measured at several temperatures to inform on changes in secondary and tertiary structure during the endotherm. The Xray crystal structure of apo-RXRα LBD contained 12 helices composing about 66% of its secondary structure.4,7 The 222 and 208 nm negative CD signals (Figure 5A), which are significant in helical protein s tructures, were present in CD spectra at temperatures up to 56 °C.9 The magnitude of the 208 and 222 nm negative bands decreased ∼20% when heated to temperatures near to Tm measured by DSC. These signals decreased ∼40% when the dimer was heated to 75 °C, slightly higher than the temperature of the end of the DSC endotherm. No further decrease in CD signals was observed when the sample was incubated at 75 °C for 10 more minutes. This indicated that the secondary structure of apo-RXRα LBD was not completely unfolded throughout the DSC endotherm. Based on these CD spectra, the helical content of the native homodimer was 57%, and 33% remained after heating to 75 °C. In contrast, the 222 and 208 nm signals were completely lost for the homodimer in the presence of 5 M guanidine−HCl at 25 °C, which completely denatured and dissociated the dimer into monomers.41

Each monomer of apo-RXRα LBD contains two Trp: W282 in helix 2 and W305 in helix 4, which is near the rexinoid binding site. An intense fluorescence band centered at 335 nm was observed at 35 °C, consistent with the hydrophobic environment of the indole group of the two Trp in a folded state (Figure 5B). Upon heating the protein to higher temperatures, the Trp fluorescence intensity decreased due to thermal quenching,58 and the emission maximum

wavelength (λmax) gradually red-shifted to 344 nm at 70 °C. A red shift of λmax to 355 nm was observed for the completely denatured homodimer in 5 M guanidine−HCl. The much less red-shifted signals for the thermally denatured apo-RXRα LBD indicated that either one or both of the Trp were still in a partially hydrophobic environment when heated to 70 °C. Taken together, these thermodynamic and spectral data are most consistent with the native homodimer being converted to a partially unfolded and aggregated apo-RXRα LBD species above Tm.

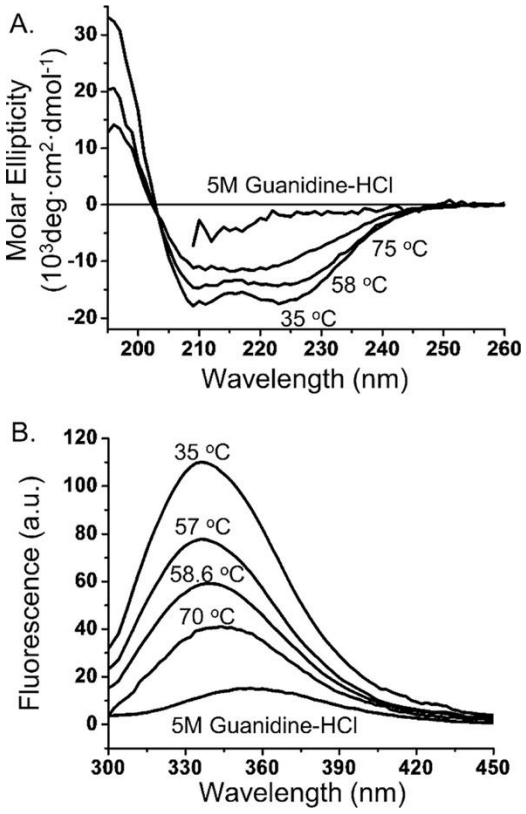

Figure 5. Spectroscopic changes in apo-RXRα LBD during thermal unfolding. (A) Circular dichroic spectra of 12 μM apo-RXRα LBD homodimer at different temperatures and in the presence of 5 M guanidine−HCl at 25 °C. (B) Fluorescence spectra of 0.05 μM apoRXRα LBD homodimer at different temperatures and in the presence of 5 M guanidine−HCl at 25 °C. The excitation wavelength was 280 nm.

Thermodynamic Unfolding Parameters at 37 °C

Using a v of 4 °C/min for DSC measurements, the time needed to unfold the protein was less than 3 min, which minimized the effects of the irreversible processes during the unfolding transition. This is reflected in the fact that the unfolding parameters obtained at 4 °C/min were very similar to the extrapolated equilibrium parameters (Table 1 and Figure S3). Therefore, all subsequent DSC experiments were conducted at 4 °C/min. To modulate unfolding Tm and enthalpy for determining the unfolding heat capacity change (ΔCp u), the pH of the buffer was changed. Due to the rapidity of the measurement and lower sample amounts, DSF was first used to survey a range of pH values between 5 and 9 (Figure S7). DSF showed that apo-RXRα LBD was most stable at pH 7.0, and it required an increase of 2 pH units to induce significant decreases in Tm. DSC was performed on apo-RXRα LBD homodimer at four different pH values: 7.0, 8.6, 9.0, and 9.5 (Figure 6A). To ensure that buffer ionization enthalpy did not contribute to the observed ΔHc, inorganic buffers with low ionization enthalpies were used. Additional DSC experiments were performed using buffers with higher ionization enthalpies. The observed ΔHc displayed no dependence on buffering components (Figure S8). ΔHc obtained in inorganic buffers was fitted linearly to Tm (Figure 6B). From the slope of the line, ΔCp u was determined to be 15 ± 1 kJ/(mol K). Using this ΔCp u and the extrapolated values of Tm eq and ΔHc eq from the DSC measurements (Table 1), ΔH of unfolding for the apo-RXRα LBD homodimer was calculated to be 347 ± 21 kJ/mol at 37 °C. ΔS of unfolding was 1.01 ± 0.06 kJ/(mol K); −TΔS was −314 ± 17 kJ/mol, and ΔG of unfolding was 33 ± 3 kJ/mol at 37 °C.

A ΔG of 32 ± 3 kJ/mol was calculated using parameters obtained at a v of 4 °C/min, which was within experimental error of the ΔG calculated from the extrapolated parameters. Apo-RXRα LBD homodimer was most stable at 20 °C, with a ΔG of 43 ± 3 kJ/ mol.

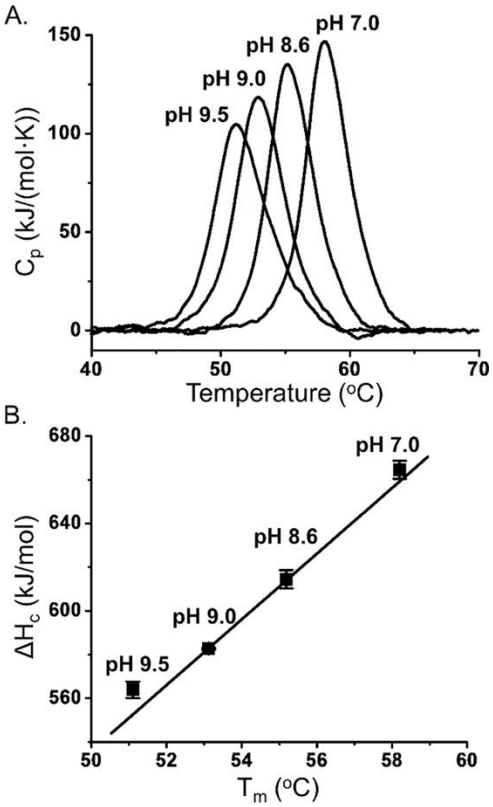

Figure 6. Determination of the unfolding heat capacity change (ΔCp u) of apo-RXRα LBD homodimers. (A) DSC molar heat capacity profiles for 1.5 μM apo-RXR-LBD homodimer using a scan rate of 4 °C/min at different pH values (from left to right): 9.5, 9.0, 8.6, and 7.0. (B) ΔCp u was determined by a linear regression of ΔHc versus Tm. The R value for the linear fit was 0.99.

According to Harder et al.,41 the chemical denaturation of apo-RXRα LBD in guanidine−HCl is reversible and follows a three-state mechanism: N2 ↔ 2I ↔ 2U, wherein “I” is a monomeric, partially unfolded, intermediate. Although the ΔG change of the first step accounts for ∼80% of the total unfolding ΔG, spectroscopy data support that the monomeric intermediate retains significant native secondary

structure, and the two Trp residues remain partially buried. It is during the second step of unfolding where this unfolding intermediate, I, loses all secondary structures, and the Trp are completely solvent exposed. The authors estimate that the ΔG of chemical denaturation for the first step is 35 ± 0.8 kJ/mol at 30 °C. From our study, the estimated thermal unfolding ΔG for apoRXRα LBD homodimers at 30 °C was 39 ± 2 kJ/mol. Likewise, the spectral data on the thermally unfolded protein (Figure 5) are similar to those estimated for the monomeric intermediate in guanidine−HCl. Guanidine−HCl is wellknown for its capability to prevent aggregation of partially or fully unfolded proteins because of its chaotropic and ionic properties.59−61 It is possible that, in our study, DSC detected the unfolding of the native dimer to a partially unfolded intermediate very similar to that detected by Harder et al. However, because of the lack of chaotropes such as guanidine−HCl to stabilize a monomer, the unfolded state was thermally aggregated without a significant heat signature.

The data presented strongly support the model N2 ↔ I2 → D, where I2 is a partially unfolded, dimeric intermediate. This model40 was used to globally fit a set of four DSF data at different scan rates (1 to 4 °C/min, Figure S5). The best fitted parameters for the reversible first step were Tm = 57.5 °C and ΔHv = 710 kJ/mol. These values were very similar to those obtained by extrapolation to infinite scan rate (Table 1). The second, irreversible step was best fitted with a single rateconstant, k, of 2.1 min−1 . To gain more understanding on how the rate of the irreversible step affects the extrapolated thermodynamic parameters obtained by fitting the DSC to a reversible model, a series of simulations were

performed using k values of 0.5, 2.1, and 8 min−1 (Figure S9A). The simulated curves were fitted to the two-state reversible model, N2 ↔ I2, and the resulting thermodynamic parameters, Tm, ΔHv, and ΔHc, were plotted against v−1 (Figure S9B). When k was 0.5 min−1 , which was relatively slow compared to the scan rates, the extrapolated Tm eq and ΔHv eq were essentially identical to the input values for the simulation (Figure S9B, green circles on the axes). When k was 8 min−1 , which was relatively fast compared to the scan rates, Tm eq and ΔHv eq were different from the input values. Tm eq was 1.5 °C lower, and ΔHv eq was 23% higher. In contrast, the observed ΔHc value was constant and equal to the input value. When k was 2.1 min−1 , which was our fitted value using the Lumry−Eyring model, Tm eq was lower by only 0.5 °C, and ΔHv eq was higher by 9%. Again, ΔHc was scan-rate-independent and equal to the input value. In short, if partial reversibility was established, and the rate of the irreversible step was no faster than the highest scan rate, then Tm eq obtained by extrapolation to infinity v was within 1% of the input value. ΔHv eq could be different from the input value, but ΔHc eq was equal to the input value. Therefore, ΔHc eq became the logical choice to use for the calculation of other thermodynamic parameters, such as ΔG.

The ΔG of unfolding for apo-RXRα LBD was unusually low compared to other dimeric proteins, which may suggest a weak dimeric interface ready to dissociate into monomers at submicromolar concentrations to facilitate the formation of heterodimers with other receptors.41 However, our thermal unfolding data indicated that the dimer interface was relatively stable as it did

not dissociate throughout the unfolding endotherm. This was more consistent with the DNA binding properties and transcriptional activities observed for the fulllength RXR homodimer.3,62 Moreover, the thermal unfolding of apo-RXRα LBD homodimer was accompanied by a relatively low unfolding ΔHc of 673 kJ/mol at Tm, i.e., a low specific heat of 12.5 J/g, which was substantially lower than the specific heat of a typical soluble globular protein at the same Tm (29−38 J/g according to Murphy and Freire55). The low specific heat may be caused by three factors. First, it may be due to incomplete unfolding as demonstrated by the CD and fluorescence spectroscopy data on the thermally unfolded protein. Second, it may be due to homodimers generally unfolding with lower specific heats than single domain proteins.63 Third, it may indicate that the native apo-homodimer is less compactly folded and more dynamic than typical, well-folded globular proteins. Such structural fluidity likely relates to the lack of rexinoid bound to its hydrophobic pocket and the dynamic helix 12 region of the domain.8,9

Thermal Unfolding of Holo-RXRα LBD Homodimers Bound with Rexinoids

The stability of RXRα LBD bound with rexinoid (holo-RXRα LBD) was examined next to determine the relationship between the rexinoid structure and holo-RXRα LBD unfolding energetics. Rexinoids UAB30, UAB110, and UAB111 quenched more than 90% of the protein fluorescence signal of apo-RXRα-LBD at 337 nm at 25 °C when the ratio of the protein to the rexinoids reached 1:1. The dissociation constants (Kd) determined from the binding

isotherm based on fluorescence quenching was 38 ± 14 nM for UAB30, 22 ± 6 nM for UAB110, and 2.4 ± 0.4 nM for UAB111.

DSF was first used to determine the rexinoid concentration required to saturate the binding sites at Tm because Kd was expected to be dependent on temperature. For UAB30, the DSF unfolding curve continuously shifted to higher Tm (Figure S10A) when the ligand concentration was increased from 1.25 to 25 μM using a dimer protein concentration of 2.5 μM. There was no measurable increase in Tm when the rexinoid concentration was doubled to 50 μM, indicating that effective saturation was reached at rexinoid concentrations above 25 μM (5:1 molar ratio, based on one binding site/monomer). An increase in Tm of 4.4 ± 0.1 °C in the presence of UAB30 at a 2:1 rexinoid/monomer molar ratio was consistent with UAB30 strongly binding to the native homodimer at 25 °C and at elevated temperatures. For UAB110 and UAB111, the shifts in Tm in the presence of rexinoids at a 2:1 rexinoid/monomer molar ratio were 7 and 7.5 °C, respectively, which were substantially higher than the shifts caused by UAB30 (Figure S10B) and consistent with their higher binding affinities.

DSF was also used to examine the effect of scan rate on the Tm of the holo-RXRα LBD homodimer bound with each rexinoid. The linear regression of Tm values of each complex with respect to v−1 yielded slopes almost identical to that of apo-RXRα LBD (Figure 7). This suggested that the rate of the irreversible step in the Lumry−Eyring unfolding model was similar for both holo-homodimers and the apo-homodimer.

To gather thermodynamic data on holo-RXRα LBD dimers, DSC was performed. The effect of DMSO, a cosolvent necessary for solubilizing the rexinoids, was first examined. Using a v of 4 °C/min, the Tm, ΔHc, and ΔHv values of apoRXRα LBD homodimer determined by DSC in the presence of 1% w/v DMSO (Table 2) were within experimental errors of those values obtained in the absence of DMSO (Table 1). This sample was used as the point of reference (DMSO control) for comparison with holo-RXRα LBD dimers containing rexinoids.

Rexinoid concentrations that caused maximum increases in Tm determined by DSF (30 μM for UAB30, and 10 μM for either UAB110 or UAB111) were used in DSC to minimize unwanted effects of the rexinoids at high concentrations (Figure S11). Similar to apo-RXRα LBD homodimer, only one DSC unfolding transition was observed in the presence of rexinoids (Figure 8), and the Tm of each holo-RXRα LBD increased due to the shift of unfolding equilibrium toward the native state caused by rexinoid binding to the native apo-dimer. To verify that the unfolding parameters obtained at a v of 4 °C/min for the holo-RXRα LBD homodimers were good approximations of the equilibrium parameters, the scan-rate dependence of the DSC endotherms of RXRα LBD:UAB30 (holo-RXRα LBD homodimer bound with UAB30) was examined (Figure S12 and Table S1). Similar to apo-RXRα LBD, a linear relationship existed between each unfolding parameter and v −1 (Figure S12B). The extrapolated equilibrium unfolding parameters for RXRα LBD:UAB30 were Tm eq = 63.5 ± 0.1 °C, ΔHv eq = 761 ± 38 kJ/mol, and ΔHc eq = 798 ± 8 kJ/mol

(Table S1). The unfolding parameters obtained at a v of 4 °C/min were very similar to these extrapolated values. The ratio of ΔHv eq to ΔHc eq was close to 1, as found for the apo-homodimer.

An unfolding Tm of 66.6 ± 0.5 °C was obtained for RXRα LBD:UAB110 at a v of 4 °C/min, which was 3 °C higher than the Tm of RXRα LBD:UAB30 (Figure 8 and Table 2). The ΔHc was 849 ± 13 kJ/mol, which was approximately 260 kJ/ mol higher than the apo-homodimer in 1% DMSO. RXRα LBD:UAB111 displayed similar unfolding parameters as UAB110:RXRα LBD, with a Tm of 66.9 ± 0.3 °C and a ΔHc of 840 ± 21 kJ/mol. Both RXRα LBD:UAB110 and RXRα LBD:UAB111 also exhibited a ΔHv/ΔHc ratio close to unity, consistent with the holo-RXRα LBD homodimers being the cooperative unfolding unit.

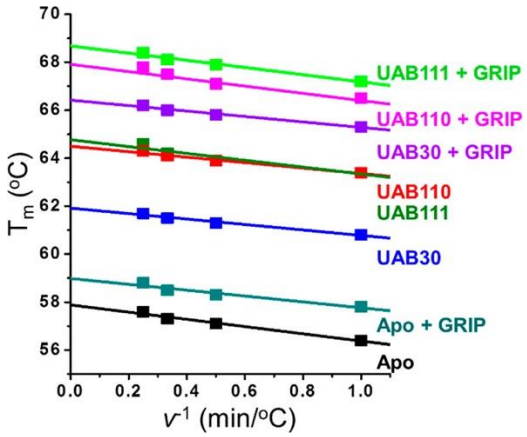

Figure 7. DSF Tm values as a function of v−1 for RXRα LBD homodimers with and without rexinoids or coactivator peptide. DSF Tm values of 2.5 μM RXRα LBD homodimer at pH 7.0, in the presence of no rexinoid or GRIP-1 (Apo), 0.4 mM GRIP-1 (Apo + GRIP), 30 μM UAB30 (UAB30), 30 μM UAB30 and 0.4 mM GRIP1 (UAB30 + GRIP), 10 μM UAB110 (UAB110), 10 μM UAB110 and 0.4 mM GRIP-1 (UAB110 + GRIP), 10 μM UAB111 (UAB111), or 10 μM UAB111 and 0.4 mM GRIP-1 (UAB111 + GRIP). The scan rate, v, was 4.0 °C/min. The lines are linear regressions of Tm values with respect to v−1 . All samples contained 1% DMSO.

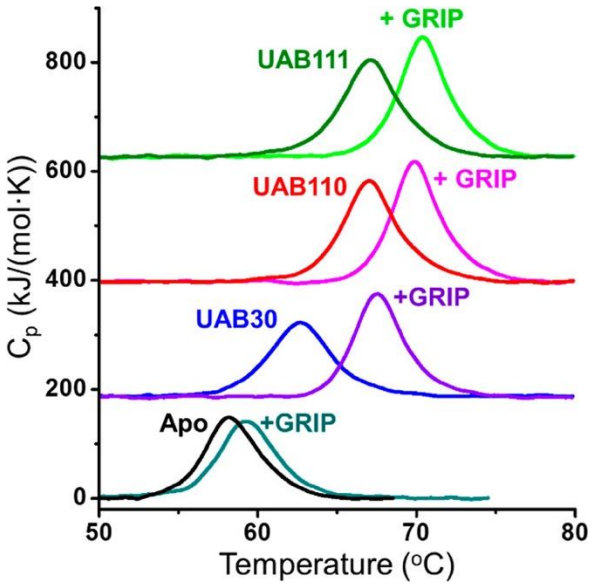

Figure 8. RXRα LBD is strongly stabilized by rexinoid binding and coactivator peptide GRIP-1. DSC molar heat capacity profiles of 1.5 μM RXRα LBD at pH 7.0, in the presence of no rexinoid or GRIP-1 (Apo), 0.4 mM GRIP-1 (+GRIP), 30 μM UAB30 (UAB30), 30 μM UAB30 and 0.4 mM GRIP-1 (UAB30 + GRIP), 10 μM UAB110 (UAB110), 10 μM UAB110 and 0.4 mM GRIP-1 (UAB110 + GRIP), 10 μM UAB111 (UAB111), or 10 μM UAB111 and 0.4 mM GRIP-1 (UAB111 + GRIP). The scan rate, v, was 4.0 °C/min. All samples contained 1% DMSO.

	T_m (°C)	ΔH_c (kJ/mol)	ΔH_v (kJ/mol)	ΔC_p^u (kJ/(mol K))	ΔH (37 °C) (kJ/mol)	$-T\Delta S$ (37 °C) (kJ/mol)	ΔG (37 °C) (kJ/mol)
apo-RXR*α* LBD[a]	58.7 ± 0.2	673 ± 8	736 ± 25	15 ± 1	347 ± 21	−314 ± 17	33 ± 3
DMSO control[b]	57.9 ± 0.4	690 ± 8	803 ± 4	15 ± 1	376 ± 17	−342 ± 17	33 ± 2
+GRIP-1	59.3 ± 0.2	690 ± 29	811 ± 13	14 ± 2	389 ± 52	−353 ± 48	36 ± 7
+UAB30	63.6 ± 0.1	803 ± 4	836 ± 13	17 ± 1	371 ± 26	−326 ± 23	45 ± 4
+UAB110	66.6 ± 0.5	849 ± 13	811 ± 17	16 ± 2	362 ± 37	−310 ± 32	52 ± 8
+UAB111	66.9 ± 0.3	840 ± 21	823 ± 21	17 ± 1	362 ± 24	−309 ± 20	53 ± 5
+UAB30/GRIP-1	67.5 ± 0.3	932 ± 33	924 ± 25	17 ± 1	374 ± 35	−317 ± 30	58 ± 8
+UAB110/GRIP-1	69.9 ± 0.5	995 ± 17	924 ± 8	18 ± 1	393 ± 35	−327 ± 30	66 ± 8
+UAB111/GRIP-1	70.4 ± 0.2	991 ± 29	928 ± 8	20 ± 2	380 ± 35	−314 ± 30	66 ± 9

[a]Equilibrium unfolding parameters obtained by extrapolating to v^{-1} is zero, in the absence of DMSO. [b]DMSO control was *apo*-RXR*α* LBD containing 1% w/v DMSO. Data for the DMSO control and all others were obtained at a *v* of 4 °C/min and in the presence of 1% DMSO.

Table 2. Thermodynamic Parameters of Unfolding of Apo-RXRα LBD and Holo-RXRα LBD with and without GRIP-1

To determine the ΔCp u values of the holo-RXRα LBD homodimers, Tm and ΔHc were measured at pH 8.8 and 9.5. In a similar manner to apo-RXRα LBD homodimers, DSF was first used to evaluate whether pH modulates the degrees of stabilization caused by the presence of rexinoids (Figure S13 and Table S2). The

shifts in Tm caused by rexinoid were within experimental errors at all three pH values. Using DSC, the measured Tm values and enthalpies were lower as pH decreased, but the relative positions and magnitudes of all DSC endotherm remained the same (Figure S14). The ΔHc value of each holo-homodimer was fitted linearly with respect to Tm to determine ΔCp u values (Table 2).

Using ΔCp u , Tm, and ΔHc from DSC measurements at a v of 4 °C/min, ΔH, ΔS, and ΔG of unfolding at 37 °C for each holo-RXRα LBD homodimer were calculated (Table 2). Compared to the apo-RXRα LBD homodimer DMSO control, the holo-RXRα LBD homodimers had significantly higher ΔG values consistent with tight binding and strong stabilization of the native state by the rexinoids. The degrees that UAB110 and UAB111 stabilized the native apo-RXRα LBD homodimer (ΔΔG = 19 and 20 kJ/mol, respectively) were notably higher than UAB30 (ΔΔG = 12 kJ/mol), which was consistent with the improved binding affinities of UAB110 and UAB111 over that of UAB30. The difference in ΔH between the DMSO control and holoRXRα LBD homodimers (ΔΔH) at 37 °C was essentially zero for each of the three rexinoids. A near-zero value for ΔΔH suggested that the binding of rexinoid to apo-RXRα LBD at physiological temperatures was accompanied by a small binding enthalpy. In order to gather information on the thermodynamics of rexinoid binding to apo-RXRα LBD, ITC measurements were performed on UAB30 between 10 and 30 °C. No ITC isotherms were obtained due to low solubility of the rexinoid in water. When reverse titrations were performed at these temperatures, the measured heat changes were within the noise levels (Figure S15), which suggested a low-enthalpy binding

reaction at these temperatures, consistent with the DSC results. The ligand binding pocket (LBP) of RXRα LBD containing UAB30 is lined with 16 hydrophobic residues contributed by 4 protein helices that surround the UAB rexinoids.8,9,13,14 The main forces that stabilize the interactions between the rexinoids and LBD residues are the ionic interaction between the carboxylate group and Arg316, and numerous hydrophobic contacts throughout the binding pocket. Burying nonpolar atoms upon ligand binding leads to a negative heat capacity change (ΔCp a).9,37 Exposing these buried nonpolar surface areas upon protein unfolding and ligand dissociation increases the unfolding ΔCp u . The ΔCp u of each of the three holo-RXRα LBD homodimers was slightly higher than that of the apoRXRα LBD homodimer in 1% DMSO (+1 to 2 kJ/(mol K)). The − TΔS values of the holo-RXRα LBD homodimers were each less negative than that of the apo-RXRα LBD homodimer in DMSO (+17 to 31 kJ/mol), which contributed favorably to the ΔG values. Therefore, rexinoid binding to apo-RXRα LBD appeared to be entropically driven at physiological temperatures. Crystallographic data indicate that, upon binding to UAB110 or UAB111, the size of the LBP expanded nearly 20% (compared to LBP in the presence of UAB30) to accommodate the two larger rexinoids (Figure 1E).14 The contact surface areas of these two rexinoids were about 100 Å2 larger than those observed for UAB30. Burying more hydrophobic surfaces likely resulted in more favorable entropy changes during the binding process and, hence, the more favorable ΔG of folding for holo-RXRα LBD homodimers bound to UAB110 or UAB111. In addition, the increase in stability of the holo-RXRα LBD homodimers could also arise from

reduced dynamics due to rexinoid binding. HDX MS studies have revealed that the dynamics of helices 3 and 11 are significantly decreased when UAB30 is bound to the homodimer8 and reduced even further in the presence of UAB110 and UAB111 whose binding affinities were higher than that of UAB30 (unpublished data). In summary, the LBP was expanded but more thermodynamically stable when bound with UAB110 or UAB111. How these conformational changes affect coactivator binding was examined next.

Thermal Unfolding of Holo-RXRα LBD Homodimers Bound with Rexinoids and a Coactivator Peptide

It was previously shown by using ITC measurements that the 13-mer coactivator peptide, GRIP-1 (Figure 1C), binds to holo-RXRα LBD complexes with a micromolar Kd at 25 °C in an exothermic reaction with binding enthalpies in the range from −36 to −42 kJ/mol per monomer.8,14 Because the binding affinity is expected to be weaker at Tm, DSF was first used to determine the GRIP-1 concentration required to saturate the peptide binding site at Tm (Figure S16). The Tm of UAB30:RXRα-LBD:GRIP-1 unfolding incrementally increased when GRIP-1 concentration was increased from 12.5 to 800 μM using a dimer protein concentration of 2.5 μM and 15 μM UAB30. A concentration of 400 μM GRIP-1 was chosen for the collection of thermodynamic data on RXRα LBD homodimer bound with rexinoid and GRIP-1.

DSF was used to examine the dependence of Tm on v (Figure 7). In the absence of rexinoids, GRIP-1 increased the Tm of apo-RXRα LBD by ∼1 °C, consistent with its low affinity to the apo-homodimer at 25 °C.9 A much larger

increase in Tm was observed in the presence of each rexinoid. All Tm values appeared linearly dependent on v−1 , and the slopes of the linear fits were similar to those obtained in the absence of GRIP-1. This again suggested that the rates of the irreversible step of the Lumry−Eyring unfolding mechanism were similar in the presence or absence of rexinoids or GRIP-1. The RXRα LBD:UAB111:GRIP-1 complex displayed the highest extrapolated Tm of 68.7 ± 0.1 °C, nearly 11 °C higher than that of the apo-homodimer. The RXRα LBD:UAB110:GRIP-1 complex had an extrapolated Tm of 67.9 ± 0.2 °C, and the RXRα LBD:UAB30:GRIP-1 complex had an extrapolated Tm of 66.4 ± 0.1 °C. Using DSC (Figure 8 and Table 2), similar increases in Tm were observed for the ternary complexes.

The ΔCp u values of holo-RXRα LBD homodimers in complex with GRIP-1 were determined from the linear dependence of ΔHc on Tm and listed in Table 2. The unfolding parameters of apo-RXRα LBD homodimer in the presence of 400 μM GRIP-1 were similar to the apohomodimer with only slightly increased Tm and ΔHc, and almost identical ΔCp u . This indicated that significant dissociation of GRIP-1 likely occurred before the apohomodimer unfolded because of low binding affinity at Tm. For two of the three RXRα LBD:rexinoid:GRIP-1 complexes, ΔCp u increased with respect to their corresponding holohomodimer without GRIP-1, while there was little observed change in ΔCp u for RXRα LBD:UAB30:GRIP-1. The largest increase in ΔCp u was 3 kJ/(mol K) for RXRα LBD:UAB111:- GRIP-1, which was within the experimental errors of the ΔCp u measurement. Therefore, an average ΔCp u value of 18 ± 2 kJ/ (mol K) was

calculated from the experimentally determined values for the three ternary complexes.

Using the above average ΔCp u value and the Tm and ΔHc values from DSC measurements at 4 °C/min, ΔH, ΔS, and ΔG of unfolding at 37 °C for the holo-RXRα LBD homodimers bound with GRIP-1 peptide were calculated (Table 2). Binding of GRIP-1 increased ΔG compared to measurements obtained in the absence of the coactivator peptide: 13 ± 4 kJ/ mol for RXRα LBD:UAB30, 14 ± 3 kJ/mol for RXRα LBD:UAB110, and 13 ± 3 kJ/mol for RXRα LBD:UAB111. Using eq 5 in Appendix I (Supporting Information) based on the shifts in Tm, the estimated Kd of GRIP-1 binding at Tm was 22 μM for RXRα LBD:UAB30, 26 μM for RXRα LBD:UAB110, and 24 μM for RXRα LBD:UAB111.

In our previous analysis using ITC,8 the binding enthalpy of GRIP-1 to RXRα LBD:UAB30 was determined to be −44.6 ± 0.1 kJ/mol per monomer at 30 °C, with a binding heat capacity change (ΔCp a) of −1.5 ± 0.1 kJ/(mol K). Using these values, binding enthalpy at 67.5 °C (Tm of the RXRα LBD:UAB30:- GRIP-1 ternary complex) was calculated to be −100 kJ/mol per monomer or −200 kJ/mol per dimer, which was similar to the measured value of −129 ± 35 kJ/mol. Based on the van't Hoff equation (eq 6 in Appendix I of Supporting Information), and a Kd of 26 μM at Tm, the Kd at 25 °C was calculated to be 0.74 μM, in close agreement with the Kd determined by ITC at this temperature.8

To obtain an accurate measurement of the ΔCp a values for GRIP-1 binding to RXRα LBD:UAB110 or RXRα LBD:UAB111, ITC was performed between 10 and 30 °C (Table S3). As observed for the RXRα LBD:UAB30 complex, the

binding stoichiometry was nearly 1:1 (coactivator peptide/ RXRα LBD monomer unit). The free energy change of GRIP1 binding to RXRα LBD:rexinoid complexes was driven strongly by a large negative enthalpy change. The ΔCp a was determined to be 1.19 ± 0.01 kJ/(mol K) for GRIP-1 binding to RXRα LBD:UAB110, and 1.11 ± 0.07 kJ/(mol K) for GRIP-1 binding to RXRα LBD:UAB111 (per monomer unit). The Kd at 25 °C was calculated to be 1.5 μM for RXRα LBD:UAB110 and 1.8 μM for RXRα LBD:UAB110, also in close agreement with the Kd determined by ITC at this temperature.14

In summary, we report here the thermal unfolding of three species of RXRα LBD homodimers: (1) the apo-homodimer alone, N2, which reversibly unfolded to a dimeric intermediate, I2, that irreversibly denatured to D with a rate constant, k; (2) the holo-homodimer bound with a rexinoid to each monomer, N2R2; and (3) the ternary complex of the homodimer bound with a rexinoid and a coactivator peptide GRIP-1 to each monomer, N2R2P2

$$N_2 \leftrightarrow I_2 \rightarrow D$$

$$\Delta G(37\ ^\circ C) = 33 kJ / mol;\ k\ (I_2 \rightarrow D) = 2.1\ min^{-1} \qquad (2)$$

$$N_2R_2 \leftrightarrow N_2 \rightarrow 2R$$

$$\Delta\Delta G(37\ ^\circ C) = 12 - 20\ kJ / mol\ (rexinoid\text{-}dependent) \qquad (3)$$

$$N_2R_2P_2 \leftrightarrow N_2\ R_2 \rightarrow 2P$$

$$\Delta\Delta G(37\ ^\circ C) = 14\ kJ / mol\ (rexinoid\text{-}independent) \qquad (4)$$

From the analyses of DSC endotherms of N2 at different scan rates, we estimated that N2 was 33 kJ/mol more stable than I2 at 37 °C. Relative to this

equilibrium, the analyses of DSC endotherms of N2R2 bound with three different UAB rexinoids indicated that N2 was stabilized by an additional 12− 20 kJ/mol, depending on the structure of the rexinoid. This stabilization was consistent with our reported 9−35 nM binding affinity of UAB rexinoids determined by fluorescence quenching assays.14 The ΔΔG of stabilization caused by each rexinoid positively correlated with their binding affinities, with UAB111 being the tightest binder. The DSC analyses of N2R2P2 revealed that GRIP-1 binding further stabilized the complex by an additional 14 kJ/mol at 37 °C. Unlike rexinoid binding, this additional stabilization was nearly identical for the homodimers bound with three different rexinoids, which was in close agreement with the Kd values of GRIP-1 release obtained by ITC.14 Even though GRIP-1 binding stabilized N2R2 the same, N2R2P2 bound with UAB110 or UAB111 was 8 kJ/mol more stable than this complex with UAB30.

The equilibrium ΔΔG of binding was determined in this study even with the apo-homodimer unfolding irreversibly. Rexinoid binding to each monomer of N2 shifted the population of N2 to N2R2, causing the equilibrium N2 ↔ I2 to require higher temperature to reach 50% unfolding. GRIP-1 binding further shifted the population to N2R2P2, thus requiring even higher temperature to produce unfolding. As long as the rexinoid/coactivator binding processes are in equilibrium, the thermodynamic parameters of binding determined from ΔΔG (Tm) and extrapolated to 37 °C using measured ΔCp will be reasonable. These measurements could be compromised if the ligand-bound species, N2R2 and/ or N2R2P2, irreversibly unfold to new denatured species with different rates. This

does not appear to be the case for this study since, as shown in Figure 7, the Tm vs v−1 plots display linear relationships with nearly identical slopes, suggesting that the rate constant and the activation energy for the irreversible step are similar for each native species.

CONCLUSIONS

In this study we demonstrated that apo-RXRα LBD homodimer is favored in the folded state by at least 33 kJ/ mol in free energy change at 37 °C, driven by a favorable enthalpy change. On a per residue basis, the enthalpy value is almost 50% less than other small globular proteins, most likely due to two factors: (1) thermal unfolding which produced an incompletely unfolded state and (2) the less compact nature of the apo-homodimer that contains a large unfilled hydrophobic rexinoid binding pocket and a dynamic c-terminal end. Upon rexinoid binding, the hydrophobic pocket is filled, stabilized by numerous hydrophobic and hydrophilic interactions between the rexinoids and binding pocket residues. These interactions also help bridge the helices interacting with the rexinoids to those at the terminal end where the coactivator peptide binds. We clearly demonstrate here for the first time that rexinoid binding to apo-RXRα LBD is entropically driven at physiological temperatures with negligible enthalpy change. The rexinoids enhanced the stability of the homodimer complex by 12−20 kJ/mol, depending on their structure. The ΔΔG of stabilization is 8 kJ/mol less for UAB30 than the larger and more hydrophobic UAB110 or UAB111. The binding of coactivator peptide results in an additional stabilization to the homodimer complex of approximately 14 kJ/mol. The incremental increase in free energy is the same for each of the three

rexinoids studied. Our data on GRIP-1 binding to apo-RXRα LBD also indicate that a bound rexinoid is required for coactivator peptide binding. Structurally, the homodimer complexes with GRIP-1 are essentially identical. It seems as if GRIP-1 does not sense the subtle differences in the LBP conformation caused by different rexinoids as long as the LBP is occupied by an agonist of sufficient size and hydrophobicity to promote GRIP-1 binding to its site on the surface of the domain. These results suggest that, for future studies on RXR heterodimers, we would want to investigate RXR heterodimer interactions in addition to differential coactivator affinity. Alternatively, we may find that different RXR coactivator LXXLL motifs have unique binding characteristics with unique RXR ligands.

Finally, even though the GRIP-1 binding thermodynamics are the same for each of the three holo-homodimers, the complexes of UAB110 and UAB111 are each more stable than the UAB30 complex (8 kJ/mol) not due to enhanced coactivator interactions but due to hydrophobic interactions of the rexinoid in its interior binding pocket. The enhanced stability of UAB110 and UAB111 correlates well with in vitro transcriptional assays14 that clearly demonstrate that UAB111 is one of the most potent RXRα agonists discovered to date (40-fold more potent than UAB30). As reported here, despite the essentially identical X-ray crystal structures of the homodimer complexes, the two homodimer complexes with UAB110 or UAB111 are clearly more stable than the complex with UAB30. This demonstrates the value in thermodynamic measurements in predicting agonist potency. The gathering of this information was made more complicated by an irreversible step in the thermal unfolding of apo-RXRα LBD dimers. The comprehensive analyses

presented here not only yield specific thermodynamic information on the rexinoids studied but also provide a general method of how to deal with this complication. These studies lay the groundwork for future thermodynamic studies on RXR agonists and antagonists, as well as RXR heterodimers and other coactivators.

SUPPORTING INFORMATION

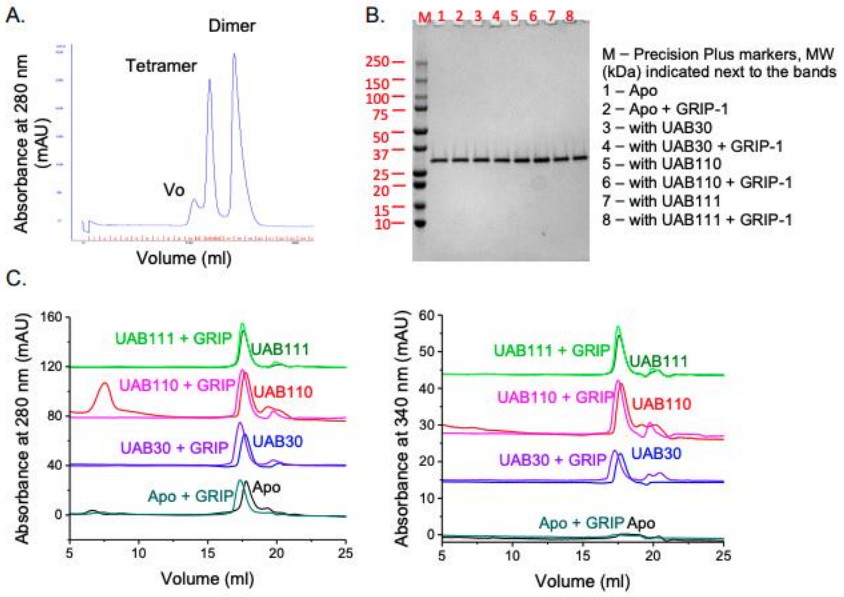

Figure S1. Size exclusion chromatography and SDS-PAGE A) Size exclusion chromatography (SEC) of affinity purified apo-RXRα LBD on a HiLoad Superdex 75 26/60 column. B) SDS-PAGE of apo-RXRα LBD and its complexes with rexinoids and/or GRIP-1 used in this study. C) SEC of apo-RXRα LBD and its complexes with rexinoids and/or GRIP-1 on a Superose 6 Increase 10/300 GL column. Left panel, absorbance at 280 nm. Right panel, absorbance at 340 nm, which was near the absorption maxima of the UAB rexinoids. Data indicated that the rexinoids formed tight complexes with the protein and co-eluted with the protein in SEC.

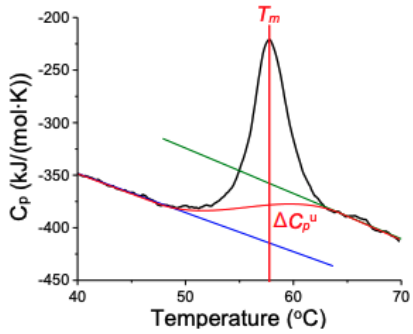

Figure S2. A typical DSC endotherm and the cubic baseline DSC molar heat capacity profile of 1.5 μM RXRα LBD at pH 7.0 prior to subtraction of a cubic baseline. The scan rate, v, was 3.0 oC/min. The blue line is the linear regression of the pre-transitional baseline between 40 and 47 oC. The green line is the linear regression of the post-transitional baseline between 64 and 70 oC. The red line is the cubic baseline determined by the software that approximates the gradual change of heat capacity from the native state to the unfolded state. An apparent ΔCp u of 57.1 kJ/(mol·K)), which was very different from the value determined in Fig. 6, was estimated from the difference between the two linear baselines at Tm.

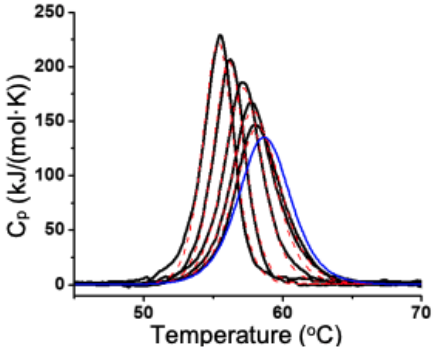

Figure S3. Two-state fits of the DSC endotherms and extrapolation to infinite scan-rate. DSC molar heat capacity profiles (solid black lines) for 1.5 μM apo-RXRα LBD homodimer at different scan rates, v (from left to right): 0.5, 1.0, 2.0, 3.0, and 4.0 oC/min. The dashed red lines are the "MN2state" fits of the DSC data (see Materials and Methods). The blue solid line is the simulated DSC endotherm using the equilibrium unfolding parameters obtained by extrapolation to zero v -1 .

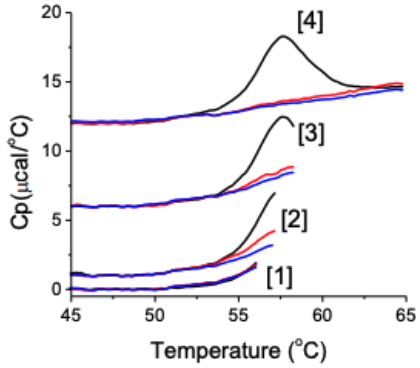

Figure S4. Partial reversibility in DSC Three consecutive DSC scans of the same apo-RXRα LBD homodimer sample. Black, First scans; red, second scans; blue, third scans. Total protein concentration was 1.5 μM. Scan rate was 2°C/min. Scans were grouped by their end temperatures: [1] 56.1 oC, 25% unfolding; [2] 57.2 oC, 50% unfolding; [3] 58.3 oC, 75% unfolding; [4] 64.8 oC, 100% unfolding. A linear regression of the pre-transitional baseline (between 45 and 50 oC) was subtracted from each curve to floor the pre-transition region. Curves were also Y-shifted for clarity.

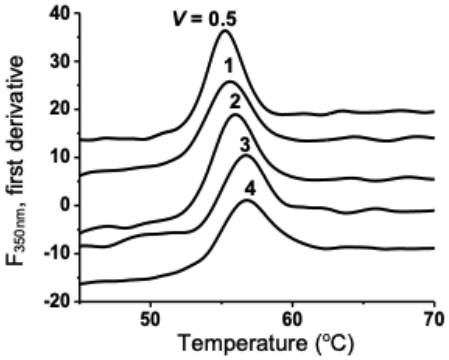

Figure S5. Scan-rate dependence of DSF unfolding transitions of apo-RXRα LBD First derivative of the intrinsic fluorescence intensity of 2.5 μM apo-RXRα LBD homodimer at 350 nm (F350nm) as a function of temperature at different scan rates (v): 0.5, 1.0, 2.0, 3.0, and 4.0 oC/min. Curves are Y-shifted for clarity. The excitation wavelength (λex) was 290nm.

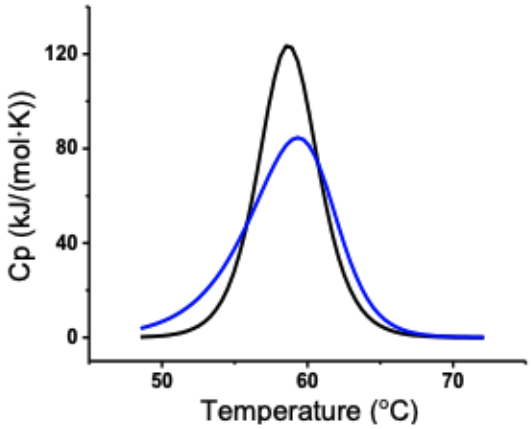

Figure S6. Simulated DSC unfolding transitions of a hypothetical dimeric protein using two-state models with or without dimer dissociation Black line: using the N ↔ U model (Model I) with Tm = 58.7 oC, and ΔHc = 673 kJ/mol. Blue line: using the N2 ↔ 2U model (Model II) with Tm = 58.7 oC, and ΔHc = 673 kJ/mol. Note that the definition of Tm for Model I is that the unfolding equilibrium constant, Ku, at Tm is 1; whereas for Model II, the Ku at Tm is 2Pt where Pt is the total protein concentration in terms of the dimer. When the blue curve was fitted using a nondissociative model, the apparent ΔHv/ΔHc was 0.69.

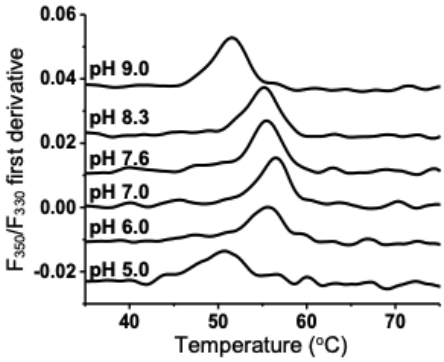

Figure S7. pH dependence of DSF unfolding transitions First derivative of the fluorescence ratio (F350nm/F330nm) of 1.5 μM apo-RXRα LBD homodimer as a function of temperature at different pH values: 9.0, 8.3, 7.6, 7.0, 6.0, and 5.0. The scan rate was 4 oC/min. Curves are Y-shifted for clarity.

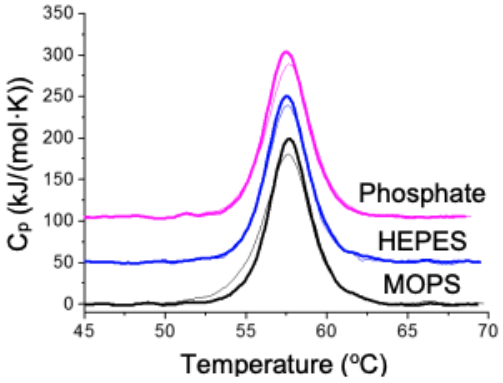

Figure S8. DSC of apo-RXRα LBD at pH 7.0 in different buffers

DSC molar heat capacity profiles of 1.5 μM RXRα LBD at pH 7.0 in MOPS (black), HEPES (blue), or phosphate (pink). The scan rate, v, was 2.0 oC/min. Two DSC experiments (thick line and thin line) were performed in each buffer. The average ΔHc was 678 ± 9 kJ/mol in MOPS, 670 ± 11 kJ/mol in HEPES, and 682 ± 13 kJ/mol in phosphate. The buffers contained 10 mM sodium salt of the buffering component, 50 mM NaCl, 0.5 mM EDTA, and 1 mM TCEP.

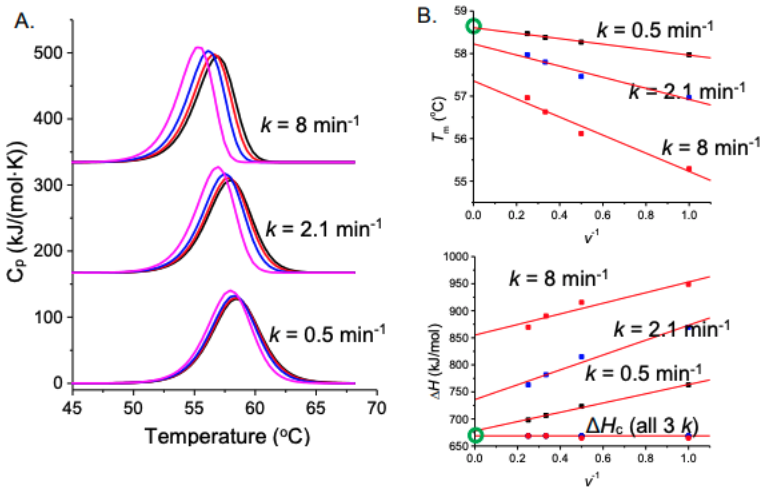

Figure S9. Effect of rate constant of the irreversible step on DSC Tm and ΔH

A) Simulated DSC endotherms based on the model N2 ↔ I2 → D (see Materials and Methods). The input parameters for the reversible step, N2 ↔ I2, were Tm = 58.7 oC, ΔHv = ΔHc = 673 kJ/mol. The input parameters for the irreversible step, I2 → D, were k = 0.5, 2.1, or 8 min-1 , and enthalpy = 0. The scan rates were 1 oC/min (pink), 2 oC/min (blue), 3 oC/min (red), and 4 oC/min (black). B) Scan rate dependence of the apparent Tm, ΔHv, and ΔHc of the DSC endotherms in panel A, obtained by fitting to a two-state reversible model. The green circles on the axes indicate the input Tm and ΔH values.

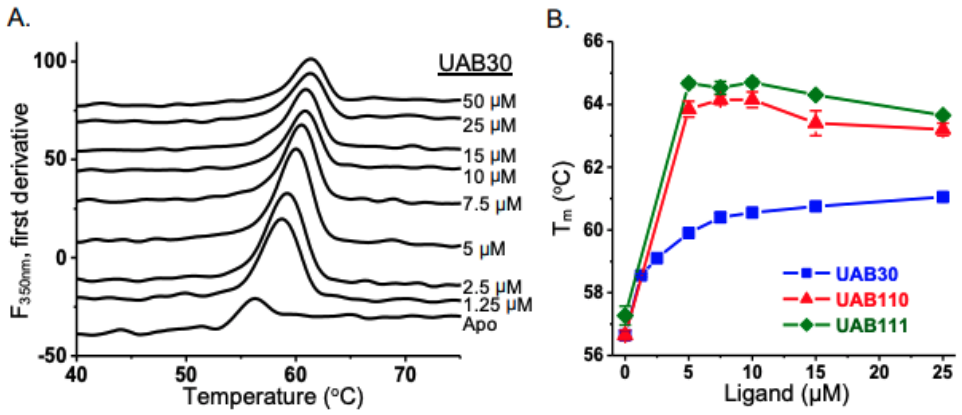

Figure S10. Determination of saturating rexinoid concentrations at Tm

A) First derivative of the intrinsic fluorescence intensity of 2.5 μM RXRα LBD homodimer at 350 nm (F350nm) as a function of temperature, in the presence of increasing concentrations of UAB30 from 0 to 50 μM. Curves are Y-shifted for clarity. B) DSF Tm of 2.5 μM RXRα LBD homodimer in the presence of increasing rexinoids, determined from DSF curves as those shown in panel A. For UAB110 and UAB111, as rexinoid concentration increased beyond 2:1 ligand/monomer molar ratio, the Tm decreased. In addition, the magnitude of the fluorescence unfolding peak diminished significantly. No unfolding transition was observable by DSF at 50 μM (Fig. S11A, see below). To explore if the loss of the fluorescence unfolding signal was caused by quenching of Trp fluorescence by rexinoids, which absorb in the 320-350 nm range [Atigadda et al., 2003], the effect of rexinoids on the unfolding of a control protein, B. subtilis NAD synthetase (NADS), was investigated (Fig. S11B). NADS is a 60-kDa homodimeric enzyme, of which thermal unfolding mechanism and substrate binding properties have been determined previously (see reference #54 in main text). The DSF curves of NADS did not shift to higher Tm in the presence of rexinoids, indication of no specific interaction between this 0 5 10 15 20 25 56 58 60 62 64 66 UAB30 UAB110 UAB111 T m (oC) Ligand (μM) B. 40 50 60 70 -50 0 50 100 F350nm, first derivative Temperature (oC) 50 μM 25 μM 15 μM 10 μM 7.5 μM 5 μM 2.5 μM 1.25 μM Apo A. UAB30 S8 protein and the rexinoids. However, similar decreases in both NADS Tm and the magnitude of DSF unfolding peak were observed with higher concentrations of UAB110 or UAB111, as well as the loss of unfolding signal at 50 μM. Additionally, light scattering of the DSF samples during unfolding indicated precipitation of UAB110 and UAB111 at concentrations above 15 μM (Fig. S11D), whereas UAB30 was soluble up to 50 μM (Fig. S11C). Therefore, the destabilizing effects at high rexinoid concentrations were nonspecific and possibly linked to their low water-solubility.

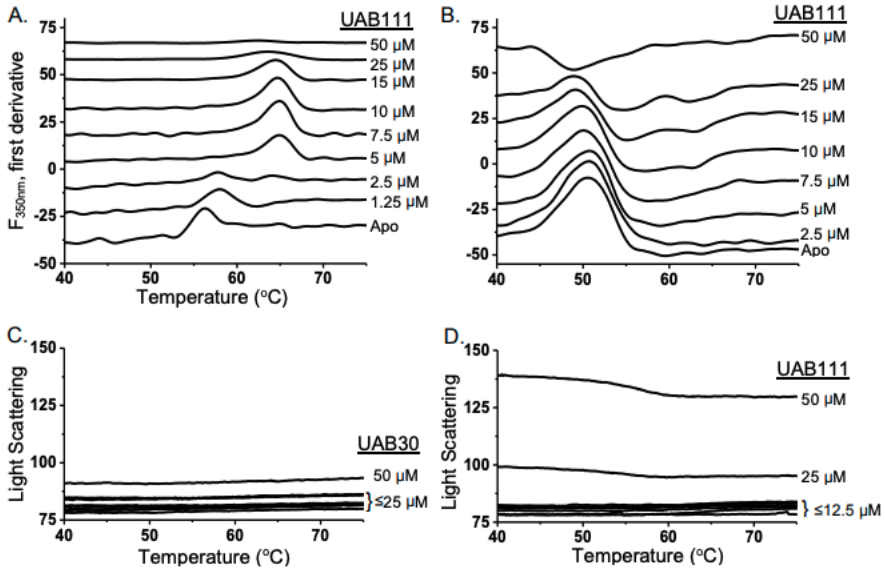

Figure S11. Nonspecific protein destabilization by UAB110 and UAB111 at high concentrations A) First derivative of the intrinsic fluorescence intensity of 2.5 μM RXRα LBD homodimer at 350 nm as a function of temperature in the presence of increasing concentrations of UAB111 from 0 to 50 μM. Curves are Y-shifted for clarity. B) First derivative of the intrinsic fluorescence intensity of 2.5 μM NAD synthetase homodimer (used as a control protein) at 350 nm as a function of temperature in the presence of increasing concentrations of UAB111 from 0 to 50 μM. Curves are Y-shifted for clarity. C) Light scattering intensity of the UAB30 samples in Fig. S10A recorded during DSF experiments. D) Light scattering intensity of the UAB111 samples in Fig. S11A recorded during DSF experiments.

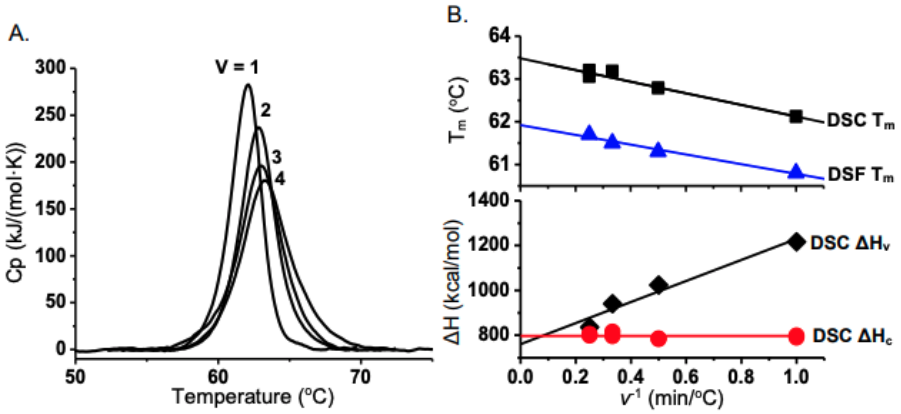

Figure S12. Equilibrium unfolding parameters of RXRα LBD:UAB30 obtained by extrapolation to infinite scan-rate

A) DSC molar heat capacity profiles for 1.5 μM RXRα LBD dimer in the presence of 30 μM UAB30 at different scan rates (v): 1.0, 2.0, 3.0, and 4.0 oC/min. B) Tm, ΔHc, and

ΔHv as a function of v -1 . Extrapolation to v -1 = 0 yielded the equilibrium unfolding parameters (see Table S1). The red line is the average of the ΔHc values at different v.

Scan Rate	DSC			DSF
v (°C/min)	T_m (°C)	ΔH_c (kJ/mol)	ΔH_v (kJ/mol)	T_m (°C)
1	62.1 ± 0.1	794 ± 4	1212 ± 4	60.80 ± 0.05
2	62.7 ± 0.1	786 ± 4	1028 ± 4	61.3 ± 0.1
3	63.0 ± 0.1	807 ± 13	945 ± 4	61.5 ± 0.1
4	63.1 ± 0.1	803 ± 4	836 ± 17	61.7 ± 0.2
Infinite	63.5 ± 0.1	798 ± 8	761 ± 38	61.9 ± 0.1

Table S1. DSC parameters of RXRα LBD:UAB30 at different scan-rates and extrapolated to infinite scan-rate

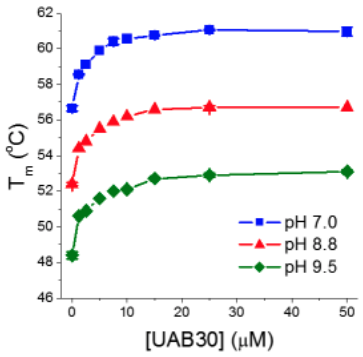

Figure S13. DSF Tm of RXRα LBD bound with UAB30 at different pH values

DSF Tm of 2.5μM RXRα LBD homodimer in the presence of increasing UAB30 at three different pH values, determined from the first derivatives of fluorescence at 350 nm as a function of temperature. Buffer conditions were: 10mM sodium phosphate, pH 7.5, 10mM sodium borate, pH 8.8, or 10 mM sodium borate, pH 9.5, with 50 mM NaCl, 0.5 mM EDTA, and 1 mM TCEP.

	DSC T_m shift (°C)		
pH	25 μM UAB30	10 μM UAB110	10 μM UAB111
7.0	4.5 ± 0.2	7.6 ± 0.4	8.1 ± 0.3
8.8	4.3 ± 0.2	7.8 ± 0.2	8.1 ± 0.2
9.5	4.5 ± 0.3	7.5 ± 0.4	8.0 ± 0.4

Table S2. DSF Tm-shifts of holo-RXRα LBD at different pH values

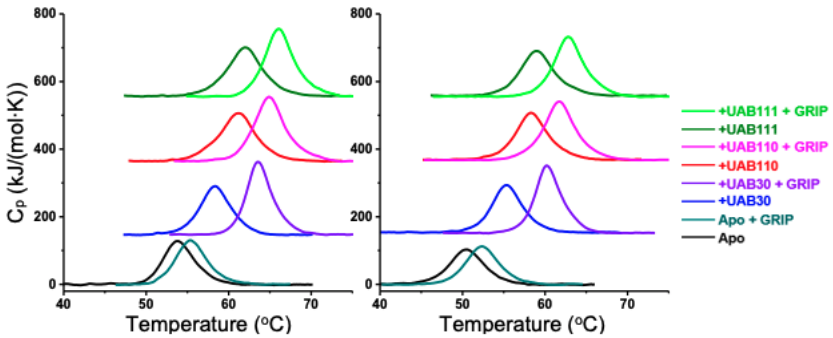

Figure S14. DSC of apo-RXRα LBD, holo-RXRα LBD with and without GRIP-1 at pH 8.8 and pH 9.5

DSC molar heat capacity profiles of 1.5 μM RXRα LBD at pH 8.8 (left panel) or pH 9.5 (right panel), in the presence of no rexinoid or GRIP-1 (Apo), 0.4 mM GRIP-1 (Apo + GRIP), 30 μM UAB30 (UAB30), 30 μM UAB30 and 0.4 mM GRIP-1 (UAB30 + GRIP), 10 μM UAB110 (UAB110), 10 μM UAB110 and 0.4 mM GRIP-1 (UAB110 + GRIP), 10 μM UAB111 (UAB111), or 10 μM UAB111 and 0.4 mM GRIP-1 (UAB111 + GRIP). The scan rate, v, was 4.0 oC/min. All samples contained 1% DMSO.

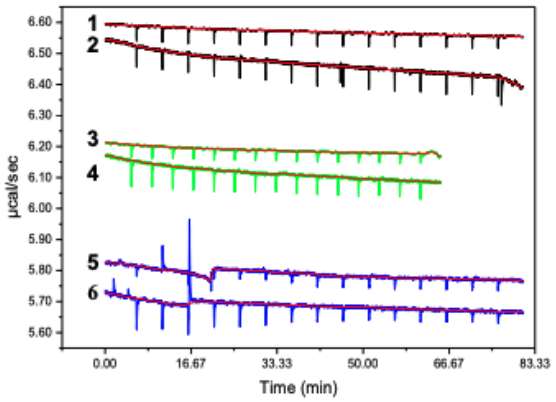

Figure S15. ITC of apo-RXRα LBD and UAB30 at different temperatures

ITC titrations of 20 µM apo-RXRα LBD homodimer to 5 µM UAB30 at 10 oC (trace 2), 20 oC (trace 4), and 30 oC (trace 6). Traces 1, 3, and 5 represent the mixing heat at each temperature where 20 µM apo-RXRα LBD homodimer was titrated to the same buffer without UAB30.

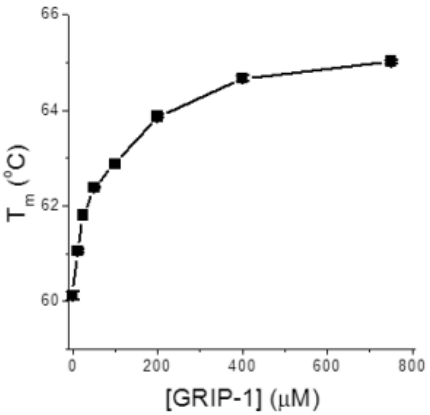

Figure S16. DSF Tm of UAB30:RXRα LBD as a function of GRIP-1 concentration

DSF Tm of 2.5μM RXRα LBD homodimer in the presence of 15 μM UAB30 and increasing GRIP-1, determined from the first derivatives of fluorescence at 350 nm as a function of temperature.

Temperature (°C)	K_d (μM)	ΔH_a (kJ/mol)	$-T\Delta S_a$ (kJ/mol)	ΔG_a (kJ/mol)	n	ΔC_p[a] kJ/(mol·K)
UAB110						
10	3.8	-11.7	-18.4	-29.3	1.05	
20	3.3	-23.4	-7.5	-30.9	1.10	
30	5.6	-35.1	4.6	-30.5	1.18	-1.19 ± 0.01
UAB111						
15	7.9	-11.7	-16.3	-28.0	1.16	
20	2.4	-18.4	-13.4	-31.8	1.05	
30	3.2	-27.6	-4.2	-31.8	1.25	-1.11 ± 0.07

Table S3. Summary of ITC measurements of GRIP-1 to RXRα LBD:rexinoid complexes

Appendix I.

Equations for calculation of thermodynamic parameters

Calculation of unfolding thermodynamic parameters at temperatures other than Tm. The following equations were used to calculate ΔG, ΔH, and ΔS of unfolding as a function of T from the experimentally determined Tm, ΔHc, and ΔCp u : ΔH(T) = ΔHc(Tm) + ΔCp u (T - Tm) (1) ΔS(T) = ΔS(Tm) + ΔCp u [ln(T/Tm)] (2) ΔG(T) = ΔH – T ΔS (3) Since ΔG(Tm) is 0 at Tm, ΔS(Tm) = ΔHc(Tm)/Tm (4) Calculation of rexinoid binding constant. Binding constant (Ka) of rexinoid to apo-RXRα LBD at the unfolding temperature was calculated from the increase in unfolding temperature of apo-RXRα LBD in the presence of rexinoids based on the following equation (1): Ka(Tn) = Ka(Tn)

= (1/Lf)exp{(-ΔHc/R)(1/Tn-1/Tm) + (ΔCpu/R)[ln(Tn/Tm) + Tm/Tn-1]} (5) where Tn was the unfolding temperature of apo-RXRα LBD in the presence of rexinoid, Tm was the unfolding temperature in the absence of rexinoid, R was the universal gas constant, ΔHc was the calorimetric unfolding enthalpy of apo-RXRα LBD in the absence of rexinoid at Tm, ΔCp u was the unfolding heat capacity change in the absence of rexinoid, and Lf was the free rexinoid concentration at Tn, which equaled to total rexinoid concentration minus half of the total protein concentration. Calculation of Ka was performed on a per monomer basis assuming the two binding sites of the homodimer (one in each monomer) are identical and noncooperative. To minimize unwanted processes due to great excesses of ligand (2), Ka was calculated based on the shift in Tm at 1:1 rexinoid/monomer molar ratio. Calculation of GRIP-1 binding constant. Ka of GRIP-1 binding at the unfolding temperature was calculated from the increase in unfolding temperature of holo-RXRα LBD in the presence of GRIP-1 based on Equation (5), where Tn was the unfolding temperature of holo-RXRα LBD in the presence of GRIP1, Tm was the unfolding temperature in the absence of GRIP-1, ΔHc was the calorimetric unfolding enthalpy of holo-RXRα LBD in the absence of GRIP-1 at Tm, ΔCp u was the unfolding heat capacity change in the absence of GRIP-1, and Lf was the free GRIP-1 concentration at Tn, which equaled to total GRIP-1 concentration minus half of the total protein concentration. Ka of GRIP-1 binding at other temperatures was calculated based on the integrated van't Hoff equation: Ka(T) = Ka(Tn)·exp{(-ΔHa/R)(1/T -1/Tn) + (ΔCpa/R)[ln(T/Tn) + Tn/T -1]} (6) where R was the universal gas constant, Tn was the unfolding temperature of holo-RXRα LBD in the presence of GRIP-1, ΔHa was the GRIP-1 binding enthalpy at Tn, and ΔCp a was the binding heat capacity change.

ACKNOWLEDGEMENTS

The authors would like to thank Dr. Christie Brouillette for her helpful comments on the manuscript. Access to the VPCapillary DSC, Auto-iTC200, and Prometheus NT.48 instruments was provided by the Biocalorimetry Lab supported by the NIH Shared Instrumentation Grant 1S10RR026478 and Shared Facility Program of the UAB Comprehensive Cancer Center, Grant 316851.

FUNDING

NIH Grant P01 CA210946

COMPETING INTERESTS

The authors declare no competing financial interest.

ABBREVIATIONS

RXRα LBD, retinoid X receptor-alpha ligand binding domain; LBP, ligand binding pocket; 9cRA, 9-cis retinoic acid; GRIP-1, glucocorticoid receptor interacting protein-1; RXRα LBD:UAB30, RXRα LBD bound to UAB30; RXRα LBD:UAB30:GRIP-1, RXRα LBD bound to UAB30 and GRIP-1; RXRα LBD:UAB110, RXRα LBD bound to UAB110; RXRα LBD:UAB110:GRIP-1, RXRα LBD bound to UAB110 and GRIP-1; RXRα LBD:UAB111, RXRα LBD bound to UAB111; RXRα LBD:UAB111:GRIP-1, RXRα LBD bound to UAB111 and GRIP-1; SRC, steroid receptor coactivator; DSC, differential scanning calorimetry; v, scan or heating rate; Tm, thermal unfolding temperature; ΔHv, van’t Hoff enthalpy of unfolding; ΔHc, calorimetric enthalpy; ΔG,

Gibbs free energy of unfolding; ΔS, entropy of unfolding; ΔCp u , unfolding heat capacity change; Ku, unfolding equilibrium constant; DSF, differential scanning fluorimetry; F350/F330, ratio of fluorescence intensity at 350 nm divided by fluorescence intensity at 330 nm; λex, excitation wavelength for fluorescence measurements; CD, circular dichroism; ITC, isothermal titration calorimetry; ΔHa, binding enthalpy; ΔCp a , binding heat capacity change; Ka, ligand binding constant; Kd, ligand dissociation constant; HDX-MS, hydrogen−deuterium exchange mass spectrometry; N, native folded protein; U, reversibly unfolded protein; D, irreversibly denatured protein; I, partially unfolded intermediate; k, rate constant of irreversible step; R, rexinoid; P, coactivator peptide GRIP-1; N2, native folded apo-RXRα LBD homodimer protein; I2, partially unfolded apo-RXRα LBD dimeric intermediate; N2R2, native folded holo-RXRα LBD homodimer bound with rexinoids; N2R2P2, native folded holo-RXRα LBD homodimer bound with rexinoids and GRIP-1

REFERENCES

(1) Dawson, M. I., and Xia, Z. (2012) The retinoid X receptors and their ligands. Biochim. Biophys. Acta, Mol. Cell Biol. Lipids 1821, 21− 56.

(2) Mangelsdorf, D. J., Thummel, C., Beato, M., Herrlich, P., Schutz, G., Umesono, K., Blumberg, B., Kastner, P., Mark, M., Chambon, P., and Evans, R. M. (1995) The nuclear receptor superfamily: the second decade. Cell 83, 835−839.

(3) Zhao, Q., Chasse, S. A., Devarakonda, S., Sierk, M. L., Ahvazi, B., and Rastinejad, F. (2000) Structural basis of RXR-DNA interactions. J. Mol. Biol. 296, 509−520.

(4) Bourguet, W., Ruff, M., Chambon, P., Gronemeyer, H., and Moras, D. (1995) Crystal structure of the ligand-binding domain of the human nuclear receptor RXR-alpha. Nature 375, 377−382.

(5) Egea, P. F., Mitschler, A., Rochel, N., Ruff, M., Chambon, P., and Moras, D. (2000) Crystal structure of the human RXRalpha ligandbinding domain bound to its natural ligand: 9-cis retinoic acid. EMBO J. 19, 2592−2601.

(6) Egea, P. F., Mitschler, A., and Moras, D. (2002) Molecular recognition of agonist ligands by RXRs. Mol. Endocrinol. 16, 987−997.

(7) Eberhardt, J., McEwen, A. G., Bourguet, W., Moras, D., and Dejaegere, A. (2019) A revisited version of the apo structure of the ligand-binding domain of the human nuclear receptor retinoic X receptor alpha. Acta Crystallogr., Sect. F: Struct. Biol. Commun. 75, 98− 104.

(8) Boerma, L. J., Xia, G., Qui, C., Cox, B. D., Chalmers, M. J., Smith, C. D., Lobo-Ruppert, S., Griffin, P. R., Muccio, D. D., and Renfrow, M. B. (2014) Defining the communication between agonist and coactivator binding in the retinoid X receptor alpha ligand binding domain. J. Biol. Chem. 289, 814−826.

(9) Xia, G., Boerma, L. J., Cox, B. D., Qiu, C., Kang, S., Smith, C. D., Renfrow, M. B., and Muccio, D. D. (2011) Structure, energetics, and dynamics of binding coactivator peptide to the human retinoid X receptor alpha ligand binding domain complex with 9-cis-retinoic acid. Biochemistry 50, 93−105.

(10) Nahoum, V., Perez, E., Germain, P., Rodriguez-Barrios, F., Manzo, F., Kammerer, S., Lemaire, G., Hirsch, O., Royer, C. A., Gronemeyer, H., de Lera, A. R., and Bourguet, W. (2007) Modulators of the structural dynamics of the retinoid X receptor to reveal receptor function. Proc. Natl. Acad. Sci. U. S. A. 104, 17323−17328.

(11) Zhang, H., Li, L., Chen, L., Hu, L., Jiang, H., and Shen, X. (2011) Structure basis of bigelovin as a selective RXR agonist with a distinct binding mode. J. Mol. Biol. 407, 13−20.

(12) Lippert, W. P., Burschka, C., Gotz, K., Kaupp, M., Ivanova, D., Gaudon, C., Sato, Y., Antony, P., Rochel, N., Moras, D., Gronemeyer, H., and Tacke, R. (2009) Silicon analogues of the RXR-selective retinoid agonist SR11237 (BMS649): chemistry and biology. ChemMedChem 4, 1143−1152.

(13) Atigadda, V. R., Xia, G., Desphande, A., Boerma, L. J., LoboRuppert, S., Grubbs, C. J., Smith, C. D., Brouillette, W. J., and Muccio, D. D. (2014) Methyl substitution of a rexinoid agonist improves potency and reveals site of lipid toxicity. J. Med. Chem. 57, 5370− 5380.

(14) Atigadda, V. R., Xia, G., Deshpande, A., Wu, L., Kedishvili, N., Smith, C. D., Krontiras, H., Bland, K. I., Grubbs, C. J., Brouillette, W. J., and Muccio, D. D. (2015) Conformationally Defined Rexinoids and Their Efficacy in the Prevention of Mammary Cancers. J. Med. Chem. 58, 7763−7774.

(15) Heery, D. M., Kalkhoven, E., Hoare, S., and Parker, M. G. (1997) A signature motif in transcriptional co-activators mediates binding to nuclear receptors. Nature 387 (6634), 733−736.

(16) Yan, X., Broderick, D., Leid, M. E., Schimerlik, M. I., and Deinzer, M. L. (2004) Dynamics and ligand-induced solvent accessibility changes in human retinoid X receptor homodimer determined by hydrogen deuterium exchange and mass spectrometry. Biochemistry 43, 909−917.

(17) Chalmers, M. J., Busby, S. A., Pascal, B. D., He, Y., Hendrickson, C. L., Marshall, A. G., and Griffin, P. R. (2006) Probing protein ligand interactions by automated hydrogen/ deuterium exchange mass spectrometry. Anal. Chem. 78, 1005−1014.

(18) Lu, J., Cistola, D. P., and Li, E. (2006) Analysis of ligand binding and protein dynamics of human retinoid X receptor alpha ligand-binding domain by nuclear magnetic resonance. Biochemistry 45, 1629−1639.

(19) Chandra, V., Huang, P., Hamuro, Y., Raghuram, S., Wang, Y., Burris, T. P., and Rastinejad, F. (2008) Structure of the intact PPARgamma-RXR- nuclear receptor complex on DNA. Nature 456, 350− 356.

(20) Chandra, V., Wu, D., Li, S., Potluri, N., Kim, Y., and Rastinejad, F. (2017) The quaternary architecture of RARbeta-RXRalpha heterodimer facilitates domain-domain signal transmission. Nat. Commun. 8, 868.

(21) Zhang, J., Chalmers, M. J., Stayrook, K. R., Burris, L. L., GarciaOrdonez, R. D., Pascal, B. D., Burris, T. P., Dodge, J. A., and Griffin, P. R. (2010) Hydrogen/deuterium exchange reveals distinct agonist/ partial agonist receptor dynamics within vitamin D receptor/retinoid X receptor heterodimer. Structure 18, 1332−1341.

(22) Lou, X., Toresson, G., Benod, C., Suh, J. H., Philips, K. J., Webb, P., and Gustafsson, J. A. (2014) Structure of the retinoid X receptor alpha-liver X receptor beta (RXRalpha-LXRbeta) heterodimer on DNA. Nat. Struct. Mol. Biol. 21, 277−281.

(23) Kojetin, D. J., Matta-Camacho, E., Hughes, T. S., Srinivasan, S., Nwachukwu, J. C., Cavett, V., Nowak, J., Chalmers, M. J., Marciano, D. P., Kamenecka, T. M., Shulman, A. L., Rance, M., Griffin, P. R., Bruning, J. B., and Nettles, K. W. (2015) Structural mechanism for signal transduction in RXR nuclear receptor heterodimers. Nat. Commun. 6, 8013.

(24) Grubbs, C. J., Lubet, R. A., Atigadda, V. R., Christov, K., Deshpande, A. M., Tirmal, V., Xia, G., Bland, K. I., Eto, I., Brouillette, W. J., and Muccio, D. D. (2006) Efficacy of new retinoids in the prevention of mammary cancers and correlations with short-term biomarkers. Carcinogenesis 27, 1232−1239.

(25) Muccio, D. D., Atigadda, V. R., Brouillette, W. J., Bland, K. I., Krontiras, H., and Grubbs, C. J. (2017) Translation of a TissueSelective Rexinoid, UAB30, to the Clinic for Breast Cancer Prevention. Curr. Top. Med. Chem. 17, 676−695.

(26) Garner, E. F., Stafman, L. L., Williams, A. P., Aye, J. M., Goolsby, C., Atigadda, V. R., Moore, B. P., Nan, L., Stewart, J. E., Hjelmeland, A. B., Friedman, G. K., and Beierle, E. A. (2018) UAB30, a novel RXR agonist, decreases tumorigenesis and leptomeningeal disease in group 3 medulloblastoma patient-derived xenografts. J. Neuro-Oncol. 140, 209−224.

(27) Chou, C. F., Hsieh, Y. H., Grubbs, C. J., Atigadda, V. R., Mobley, J. A., Dummer, R., Muccio, D. D., Eto, I., Elmets, C. A., Garvet, W. T., and Chang, P. L. (2018) The retinoid X receptor agonist, 9-cis UAB30, inhibits cutaneous T-cell lymphoma proliferation through the SKP2-p27kip1 axis. J. Dermatol. Sci. 90, 343−356.

(28) Gniadecki, R., Assaf, C., Bagot, M., Dummer, R., Duvic, M., Knobler, R., Ranki, A., Schwandt, P., and Whittaker, S. (2007) The optimal use of bexarotene in cutaneous T-cell lymphoma. Br. J. Dermatol. 157, 433−440.

(29) Muccio, D. D., Brouillette, W. J., Breitman, T. R., Taimi, M., Emanuel, P. D., Zhang, X., Chen, G., Sani, B. P., Venepally, P., Reddy, L., Alam, M., Simpson-Herren, L., and Hill, D. L. (1998) Conformationally defined retinoic acid analogues. 4. Potential new agents for acute promyelocytic and juvenile myelomonocytic leukemias. J. Med. Chem. 41, 1679−1687.

(30) Atigadda, V. R., Vines, K. K., Grubbs, C. J., Hill, D. L., Beenken, S. L., Bland, K. I., Brouillette, W. J., and Muccio, D. D. (2003) Conformationally defined retinoic acid analogues. 5. Large-scale synthesis and mammary cancer chemopreventive activity for (2E,4E,6Z,8E)-8-(3′,4′-dihydro-1′(2′H)-naphthalen-1′-ylidene)-3,7- dimethyl-2,4,6-octatrienoic acid (9cUAB30). J. Med. Chem. 46, 3766−3769.

(31) Kolesar, J. M., Hoel, R., Pomplun, M., Havighurst, T., Stublaski, J., Wollmer, B., Krontiras, H., Brouillette, W. J., Muccio, D. D., Kim, K., Grubbs, C. J., and Bailey, H. E. (2010) A pilot, first-in-human, pharmacokinetic study of 9cUAB30 in healthy volunteers. Cancer Prev. Res. 3, 1565−1570.

(32) Kolesar, J. M., Andrews, S., Green, H., Havighurst, T. C., Wollmer, B. W., DeShong, K., Laux, D. E., Krontiras, H., Muccio, D. D., Kim, K., Grubbs, C. J., House, M. G., Parnes, H. L., HeckmanStoddard, B. M., and Bailey, H. H. (2019) A Randomized, PlaceboControlled, Double-Blind, Dose Escalation, Single Dose, and SteadyState Pharmacokinetic Study of 9cUAB30 in Healthy Volunteers. Cancer Prev. Res. 12, 903−912.

(33) Desphande, A., Xia, G., Boerma, L. J., Vines, K. K., Atigadda, V. R., Lobo-Ruppert, S., Grubbs, C. J., Moeinpour, F. L., Smith, C. D., Christov, K., Brouillette, W. J., and Muccio, D. D. (2014) Methylsubstituted conformationally constrained rexinoid agonists for the retinoid X receptors demonstrate improved efficacy for cancer therapy and prevention. Bioorg. Med. Chem. 22, 178−185.

(34) Doyle, M. L. (1997) Characterization of binding interactions by isothermal titration calorimetry. Curr. Opin. Biotechnol. 8, 31−35.

(35) Ward, W. H., and Holdgate, G. A. (2001) Isothermal titration calorimetry in drug discovery. Prog. Med. Chem. 38, 309−376.

(36) Brandts, J. F., and Lin, L. N. (1990) Study of strong to ultratight protein interactions using differential scanning calorimetry. Biochemistry 29, 6927−6940.

(37) Waldron, T. T., and Murphy, K. P. (2003) Stabilization of proteins by ligand binding: application to drug screening and determination of unfolding energetics. Biochemistry 42, 5058−5064.

(38) Schimerlik, M. I., Peterson, V. J., Hobbs, P. D., Dawson, M. I., and Leid, M. (1999) Kinetic and thermodynamic analysis of 9-cisretinoic acid binding to retinoid X receptor alpha. Biochemistry 38, 6732−6740.

(39) Yang, Z., and Brouillette, C. G. (2016) A Guide to Differential Scanning Calorimetry of Membrane and Soluble Proteins in Detergents. Methods Enzymol. 567, 319−358.

(40) Protasevich, I. R., Yang, Z., Wang, C., Atwell, S., Zhao, X., Emtage, S., Wetmore, D., Hunt, J. F., and Brouillette, C. G. (2010) Thermal unfolding studies show the disease causing F508del mutation in CFTR thermodynamically destabilizes nucleotide-binding domain 1. Pro. Sci. 19, 1917−1931.

(41) Harder, M. E., Malencik, D. A., Yan, X., Broderick, D., Leid, M., Anderson, S. R., Deinzer, M. L., and Schimerlik, M. I. (2009) Equilibrium unfolding of the retinoid X

receptor ligand binding domain and characterization of an unfolding intermediate. Biophys. Chem. 141, 1−10.

(42) Privalov, P. L. (1979) Stability of proteins: small globular proteins. Adv. Protein Chem. 33, 167−241.

(43) Garidel, P., Hegyi, M., Bassarab, S., and Weichel, M. (2008) A rapid, sensitive and economical assessment of monoclonal antibody conformational stability by intrinsic tryptophan fluorescence spectroscopy. Biotechnol. J. 3, 1201−1211.

(44) Zelent, B., Sharp, K. A., and Vanderkooi, J. M. (2010) Differential scanning calorimetry and fluorescence study of lactoperoxidase as a function of guanidinium-HCl, urea, and pH. Biochim. Biophys. Acta, Proteins Proteomics 1804, 1508−1515.

(45) Yin, S. W., Tang, C. H., Yang, X. Q., and Wen, Q. B. (2011) Conformational study of red kidney bean (Phaseolus vulgaris L.) protein isolate (KPI) by tryptophan fluorescence and differential scanning calorimetry. J. Agric. Food Chem. 59, 241−248.
(46) Thiagarajan, G., Semple, A., James, J. K., Cheung, J. K., and Shameem, M. (2016) A comparison of biophysical characterization techniques in predicting monoclonal antibody stability. MAbs 8, 1088−1097.

(47) Freire, E., van Osdol, W. W., Mayorga, O. L., and Sanchez-Ruiz, J. M. (1990) Calorimetrically determined dynamics of complex unfolding transitions in proteins. Annu. Rev. Biophys. Biophys. Chem. 19, 159−188.

(48) Senisterra, G. A., Markin, E., Yamazaki, K., Hui, R., Vedadi, M., and Awrey, D. E. (2006) Screening for ligands using a generic and high-throughput light-scattering-based assay. J. Biomol. Screening 11, 940−948.

(49) Lumry, R., and Eyring, H. (1954) Conformation Changes of Proteins. J. Phys. Chem. 58, 110−120.

(50) Sanchez-Ruiz, J. M. (1992) Theoretical analysis of LumryEyring models in differential scanning calorimetry. Biophys. J. 61, 921−935.

(51) Lepock, J. R., Ritchie, K. P., Kolios, M. C., Rodahl, A. M., Heinz, K. A., and Kruuv, J. (1992) Influence of transition rates and scan rate on kinetic simulations of differential scanning calorimetry profiles of reversible and irreversible protein denaturation. Biochemistry 31, 12706−12712.

(52) Tello-Solis, S. R., and Hernandez-Arana, A. (1995) Effect of irreversibility on the thermodynamic characterization of the thermal denaturation of Aspergillus saitoi acid proteinase. Biochem. J. 311, 969−974.

(53) Vogl, T., Jatzke, C., and Hinz, H. (1997) Thermodynamic stability of annexin v e17g: equilibrium parameters from an irreversible unfolding reaction. Biochemistry 36, 1657−1668.

(54) Yang, Z. W., Tendian, S. W., Carson, W. M., Brouillette, W. J., Delucas, L. J., and Brouillette, C. G. (2004) Dimethyl sulfoxide at 2.5% (v/v) alters the structural cooperativity and unfolding mechanism of dimeric bacterial NAD+ synthetase. Protein Sci. 13, 830−841.

(55) Murphy, K. P., and Freire, E. (1992) Thermodynamics of structural stability and cooperative folding behavior in proteins. Adv. Protein Chem. 43, 313−361.

(56) Nevzorov, I., Redwood, C., and Levitsky, D. (2008) Stability of two beta-tropomyosin isoforms: effects of mutation Arg91Gly. J. Muscle Res. Cell Motil. 29, 173−176.

(57) Yang, Z., Zhou, Q., Mok, L., Singh, A., Swartz, D. J., Urbatsch, I. L., and Brouillette, C. G. (2017) Interactions and cooperativity between P-glycoprotein structural domains determined by thermal unfolding provides insights into its solution structure and function. Biochim. Biophys. Acta, Biomembr. 1859, 48−60.

(58) Robbins, R. J., Fleming, G. R., Beddard, G. S., Robinson, G. W., Thistlethwaite, P. J., and Woolfe, G. J. (1980) Photophysics of aqueous tryptophan: pH and temperature effects. J. Am. Chem. Soc. 102, 6271−6279.

(59) Watlaufer, D. B., Malik, S. K., Stoller, L., and Coffin, R. L. (1964) Nonpolar Group Participation in the Denaturation of Proteins by Urea and Guanidinium Salts. Model Compound Studies. J. Am. Chem. Soc. 86, 508−514.

(60) Nozaki, Y., and Tanford, C. (1970) The solubility of amino acids, diglycine, and triglycine in aqueous guanidine hydrochloride solutions. J. Biol. Chem. 245, 1648−1652.
(61) Venkatesu, P., Lee, M. J., and Lin, H. M. (2007) Thermodynamic characterization of the osmolyte effect on protein stability and the effect of GdnHCl on the protein denatured state. J. Phys. Chem. B 111, 9045−9056.

(62) Heery, D. M., Pierrat, B., Gronemeyer, H., Chambon, P., and Losson, R. (1994) Homo- and heterodimers of the retinoid X receptor (RXR) activated transcription in yeast. Nucleic Acids Res. 22, 726−731.

(63) Privalov, P. L. (1982) Stability of proteins. Proteins which do not present a single cooperative system. Adv. Protein Chem. 35, 1− 104.

DISCUSSION

This thesis opens up new avenues to elucidate rexinoid and coactivator binding structural mechanisms in nuclear receptors. X-ray crystallography is a helpful technique as the first step in providing a 3D structure of a protein. However to understand a protein's mechanism of action the structure, function and dynamics need to be analyzed. X-ray crystal structures are a static snap-shot of proteins, but proteins are not frozen in time, they are dynamic and exist as an ensemble of multiple states.. This work aids in the understanding of the RXRα LBD that has previously been seen in the X-ray crystal structure bound to rexinoids and coactivator (GRIP-1). More importantly, this body of work allows for the understanding of what occurs in structures that have not been able to be crystallized such as RXR with rexinoid bound (no coactivator). The LBD domain is the focus of this work due to ligand binding inducing conformation changes that allow for coactivator recruitment, thus being the site of transcriptional activation.

There are more than 800 sets of LBD sequences analyzed across organisms in the Protein Data Bank. Comparison of these LBDs revealed the conservation of the canonical α-helical fold [98]. Due to the evolutional conservation of the fold in the LBDs, there is an indication of strong structure-function constraints. The majority of NRs had a π-motif but it seems evolution has removed the motif over time [98]. The only NRs that maintained the motif are RXR and HNF-4. The π-motif is found in helix 7 and creates a wider loop within the helix. The extension of the loop allows for a salt bridge to form within the dimerization interface in RXR homodimers. Throughout evolution the π-motif has remained in RXR indicating that the RXR homodimer is biologically significant even

if the function has yet to be conclusively elucidated. Figure 10 displays helix 7 with the motif labeled in magenta.

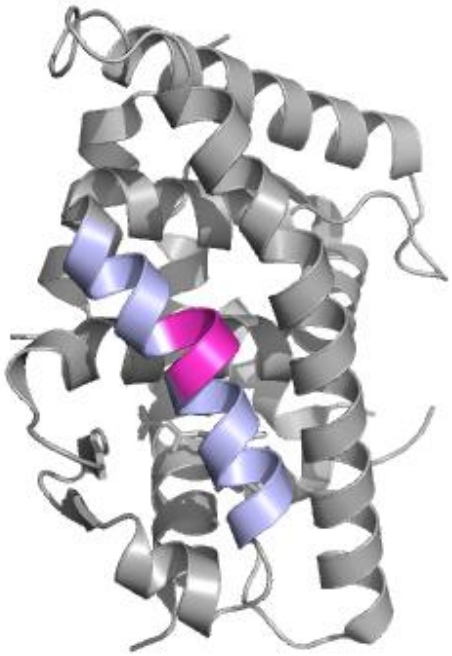

Figure 10. RXR π-motif located on helix 7. X-ray crystal structure of RXR in complex with 6mUAB30. Helix 7 is labeled in purple with the π-motif displayed in magenta.

In Chapter III, the thermal stability results of rexinoid and coactivator binding correlated with the HDX MS results in that coactivator binding did not have unique effects on RXR. All three ternary structures had the same GRIP-1 binding thermodynamics. The main distinction of a rexinoids effect on RXR's thermal stability and dynamics were revealed upon rexinoid binding. Binding of the various rexinoids induced unique differences in thermal stability. We focused on the interaction of RXR with coactivator peptide, GRIP-1, which does bind in the coactivator binding site of RXR (helices 3, 4, and 12). The full length structure of GRIP-1 involves three LxxLL motifs.

In our current work we use a GRIP-1 peptide that consists of one LxxLL. For a future direction to this work, I would investigate both the thermal stability and dynamic analysis of full length GRIP-1 in the ternary complexes. The results could shed light on if by having all three motifs we would be able to identify distinct differences in coactivator binding that were not previously seen in the CoA peptide. The main focus of most nuclear receptor structural literature tends to focuses on the coactivator binding pocket. Through our work we have shown that rexinoid binding is equally important if not more important than analyzing coactivator binding.

The structural dynamics of rexinoid binding can be placed within two responses. To my knowledge, this is one of the first description of RXR's two responses of binding. The first response being the reduction in deuterium incorporation (decreased dynamics) in regions associated with the LBP, specifically helices 3 and 5. Rexinoids that induce a decrease in dynamics in these regions correlate with their potency profiles. This response not only is exhibited in RXR but Belorusova et al. identified the profile in liver X receptor (LXR) [64]. They were able to correlate the decreased dynamics in helices 3 and 5 with the high transcript levels of intestinal *Abca1*. To further investigate how our exchange profiles correlated with other biophysical results, we mapped our HDX MS results on to the X-ray crystal structures and then labeled the binding affinities of the rexinoids to RXR (Fig. 11). A trend identified was that if a peptide in helix 3, A_{271}ADKQLFTL$_{279}$, had a reduction of dynamics, then as the exchange of helix 5 decreased, the binding affinity of a rexinoid to RXR increased. What we also revealed was that the level of decreased dynamics in the LBP correlated with toxicity. Rexinoids that induced the darkest shades of blue (decrease dynamics) seemed to be in an over

activated state and increased toxicities. This information is helpful when working within a drug discovery team when generating the next class of rexinoids.

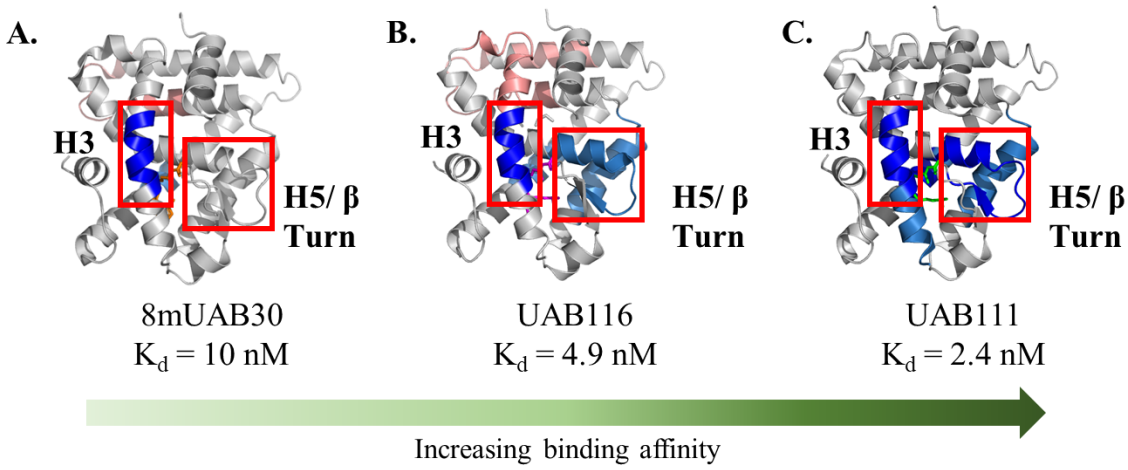

Figure 11. Connecting binding affinity to HDX MS results. (A) RXR in complex with 8mUAB30 (B) RXR: UAB116 and (C) RXR bound to UAB111. If there was a reduction of dynamics in a peptide of helix 3, A_{271}ADKQLFTL$_{279}$, then as there was a decrease in dynamics in helix 5 there was an increase in binding affinity.

The second response of binding is the increase in deuterium incorporation (increased dynamics) of the C-terminal end of helix 3, helix 8, and helix 9. An exciting future direction of work would be to perform molecular dynamic simulations on the rexinoids bound to RXR. I have two predictions as to what might be occurring upon rexinoids binding to RXR that have the second response of binding (increased dynamics). The first is that rexinoids like UAB110 are binding tightly in helix 3, which creates more dynamics at the C-terminal end of the helix that is away from the LBP. I envision a dog wagging its tail, with the core end of the tail anchored to the dog's body showing minimal movement (decreased dynamics) and the other end being very dynamic and flexible (increased dynamics). The increased dynamics in the C-terminal end of helix 3 are then "pushing" into the neighboring regions which include, helix 8, helix 9, and the

loop between them. A potential reasoning for the increased dynamics in the C-terminal end of helix 3 could be that rexinoid binding is allowing for more flexibility in the coactivator binding site, allowing for an increase in the number of different coactivators that are able to bind.

Some rexinoids binding to RXR create increased dynamics in only helices 8 and 9 and the loop between them. Helices 5, 8, and 9 create what looks like an alpha helical sandwich with helices 5 and 9 as the "buns" of the sandwich and helix 8 the portion in between the buns. My hypothesis is that the rexinoid is interacting with helix 5, shifting residues of helix 5. These residues in turn cause a pushing effect on the neighboring helix 8, which in turn creates pushes on helix 9. Molecular dynamics would further allow us to understand both of these predictions.

The reason why I think there is destabilization (increased dynamics) in the dimerization interface of the RXR homodimer is because binding of these rexinoids could potentially induce RXR to want to dissociate to be able to bind other NRs (Fig. 12). To test this hypothesis I propose a reliable binding assay such as, fluorescence resonance energy transfer (FRET). The experimental set up could be to have RXR monomers conjugated with a donor fluorophore and RAR monomers with an acceptor fluorophore. In solution, our RXR would exist as a homodimer, giving off no excitation. The introduction of RAR bound to ATRA would now compete with the RXR homodimer, causing dissociation of the homodimer to create RXR-RAR heterodimers. In the case of FRET, the two fluorophores will be in proximity only in the heterodimer, where energy transfer between them would occur and be detected by an increase in fluorescence emission of the acceptor. In this case, if my hypothesis is correct, we would add rexinoid

to the reaction, which should further destabilize the RXR homodimer and lead to further heterodimer formation measurable by increased emission detection over the non-rexinoid treated reaction.

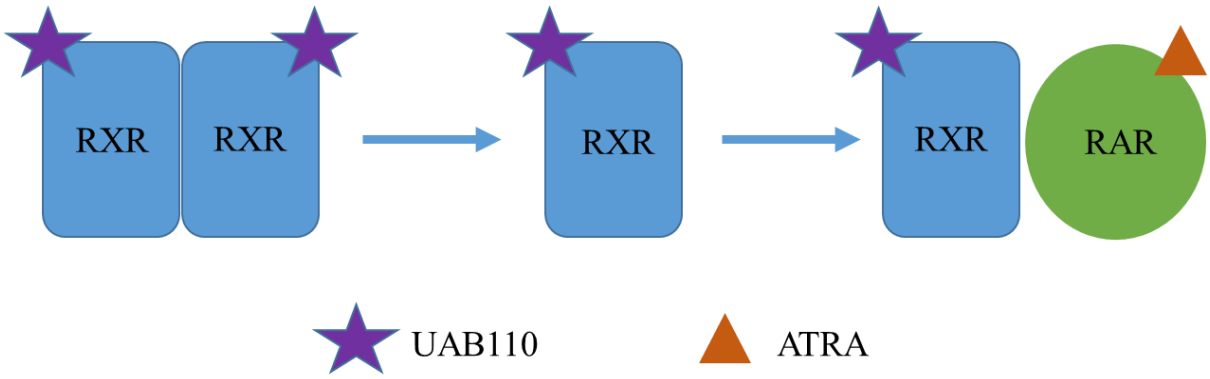

Figure 12. Hypothesized mechanism of action for rexinoids that induce an increase in dynamics in the dimerization interface.

Vivat-Hannah et al. have studied how dimerization interface residues effect the stability of RXR homodimers and RXR-RAR heterodimers [58]. In their work they used alanine scanning mutagenesis to mutate amino acids into alanine. Interestingly, introduction of single mutations in helices of the RXR homodimer prevented homodimer formation. Whereas, the same single mutations still allowed for RXR-RAR heterodimer formation. When comparing Table 1 and Table 2 from the introduction, there are significantly less contacts in the RXR homodimer interface than the RXR-RAR interface, indicating that the homodimer is less stable.

Interestingly, the increased dynamics in the regions associated with the dimerization interface has also been described for other nuclear receptors. Dai et al. analyzed HDX MS profiles of several selective estrogen receptor modulators (SERM) binding to estrogen receptor (ER). For their study, ER was homodimerized and their

results displayed increased dynamics for some of the SERMs in the loop between helices 9 and 10, and part of helix 10. These regions of ER span portions of the dimerization interface. Belorusova et al. investigated liver X receptor (LXR) binding to numerous ligands through the use of HDX MS. Two out of the seventeen rexinoids they analyzed destabilized the C-terminal end of helix 3, loop between helices 8 and 9, and the N-terminal end of helix 9. The two ligands were GW3965 and WAY-254011 and are both LXR agonists. One group was able to detect increased dynamics in helix 11 in PPAR which is part of the dimerization interface. Unlike our studies and those of ER and LXR, they determine that this ligand (Targretin) was an antagonist for PPAR. This goes to show that the second response of binding we are seeing within RXR can translate into other nuclear receptors.

In our previous studies, we analyzed the ligand binding pocket interactions of the X-ray crystal structures of UAB30 and Targretin bound to RXR. Targretin although larger than UAB30, makes fewer contacts with helix 11 residues but makes direct contacts with two helix 7 residues, Phe^{346} and Val^{349}. Two rexinoids that induced serum triglycerides 4mUAB30 and UAB111 both decreased dynamics in the helix 7 region. This supports that the methyl group on 4mUAB30 and the isopentyl group of UAB111 extend and interact with helix 7 residues. This decrease in dynamics in the helix 7 region was not seen for any other RXR-rexinoid complex. Toxicity however, is not one single mechanism and this is shown by the other triglyceride-enhancing rexinoids (Targretin, 7mUAB30, and UAB116) not displaying the same helix 7 dynamic profiles. Interestingly, this potential toxicity marker is only seen with ligand present and not when

coactivator present. This furthers the significance of having HDX MS studies with RXR-ligand alone.

RXR can also exist as homotetramers which are auto repressed. There is a gap in knowledge in understanding what stabilizes and dissociates the RXR homotetramer. The molecular mechanisms involving corepressor recruitment and antagonist-mediated repression of RXR are still elusive. I would hypothesize that corepressors such as, SMRT2 and rhein bind to the RXR homotetramer and have unique dynamics in helices 3, 11, and 12 that work to stabilize the homotetramer. Interestingly, the coactivator, corepressor, and AF-2 binding sites overlap, which leads to the question if repressed homotetramer dissociation has different dynamics than the auto repressed homotetramer. Using HDX MS on RXR bound to our structurally similar rexinoids, we would be able to analyze the differences of rexinoid binding on the dissociation of the repressed versus auto repressed homotetramer.

Nuclear receptors have been a focus within drug discovery due to their ability to induce physiological activation by low-molecular-mass ligands. RXR functions by heterodimerizing with several NRs, making it a crucial player within the regulation of numerous processes. However the focus of most NR literature has been on RXR's heterodimer partner. There is a gap in knowledge in understanding RXR's role within the structural mechanism of NR function. Throughout the course of my thesis work, I never viewed RXR as a "bound control". By deconstructing the NR system and focusing on RXR homodimer we have been able to demonstrate the complexity that this NR undergoes. We've shown that even when crystal structures of RXR look similar for different ligands bound to the protein, the dynamic profile has a larger story to tell.

GENERAL LIST OF REFERENCES

1. Porter, B.A., et al., *Structure and function of the nuclear receptor superfamily and current targeted therapies of prostate cancer.* Cancers, 2019. **11**(12): p. 1852.

2. Duvic, M., et al., *Bexarotene is effective and safe for treatment of refractory advanced-stage cutaneous T-cell lymphoma: multinational phase II-III trial results.* Journal of clinical oncology, 2001. **19**(9): p. 2456-2471.

3. Davey, R.A. and M. Grossmann, *Androgen receptor structure, function and biology: from bench to bedside.* The Clinical Biochemist Reviews, 2016. **37**(1): p. 3.

4. Tan, M.E., et al., *Androgen receptor: structure, role in prostate cancer and drug discovery.* Acta Pharmacologica Sinica, 2015. **36**(1): p. 3-23.

5. Hill, K.K., et al., *Structural and functional analysis of domains of the progesterone receptor.* Molecular and cellular endocrinology, 2012. **348**(2): p. 418-429.

6. Meijsing, S.H., et al., *DNA binding site sequence directs glucocorticoid receptor structure and activity.* Science, 2009. **324**(5925): p. 407-410.

7. Hopp, T.A., et al., *Breast cancer patients with progesterone receptor PR-A-rich tumors have poorer disease-free survival rates.* Clinical cancer research, 2004. **10**(8): p. 2751-2760.

8. Hall, J.M., D.P. McDonnell, and K.S. Korach, *Allosteric regulation of estrogen receptor structure, function, and coactivator recruitment by different estrogen response elements.* Molecular endocrinology, 2002. **16**(3): p. 469-486.

9. Leid, M., et al., *Purification, cloning, and RXR identity of the HeLa cell factor with which RAR or TR heterodimerizes to bind target sequences efficiently.* Cell, 1992. **68**(2): p. 377-395.

10. Glass, C.K., O.V. Devary, and M.G. Rosenfeld, *Multiple cell type-specific proteins differentially regulate target sequence recognition by the α retinoic acid receptor.* Cell, 1990. **63**(4): p. 729-738.

11. Lazar, M.A., T.J. Berrodin, and H.P. Harding, *Differential DNA binding by monomeric, homodimeric, and potentially heteromeric forms of the thyroid hormone receptor.* Molecular and cellular biology, 1991. **11**(10): p. 5005-5015.

12. Li, D., et al., *Functional evidence for retinoid X receptor (RXR) as a nonsilent partner in the thyroid hormone receptor/RXR heterodimer.* Molecular and cellular biology, 2002. **22**(16): p. 5782-5792.

13. Shulman, A.I., et al., *Structural determinants of allosteric ligand activation in RXR heterodimers.* Cell, 2004. **116**(3): p. 417-429.

14. Kojetin, D.J., et al., *Structural mechanism for signal transduction in RXR nuclear receptor heterodimers.* Nature communications, 2015. **6**(1): p. 1-14.

15. Mark, M., N.B. Ghyselinck, and P. Chambon, *Function of retinoid nuclear receptors: lessons from genetic and pharmacological dissections of the retinoic acid signaling pathway during mouse embryogenesis.* Annu. Rev. Pharmacol. Toxicol., 2006. **46**: p. 451-480.

16. Minucci, S., et al., *Retinoid X receptor (RXR) within the RXR-retinoic acid receptor heterodimer binds its ligand and enhances retinoid-dependent gene expression.* Molecular and Cellular Biology, 1997. **17**(2): p. 644-655.

17. Mangelsdorf, D.J., et al., *The nuclear receptor superfamily: the second decade.* Cell, 1995. **83**(6): p. 835.

18. Mangelsdorf, D.J. and R.M. Evans, *The RXR heterodimers and orphan receptors.* Cell, 1995. **83**(6): p. 841-850.

19. Harding, H.P. and M.A. Lazar, *The monomer-binding orphan receptor Rev-Erb represses transcription as a dimer on a novel direct repeat.* Molecular and cellular biology, 1995. **15**(9): p. 4791-4802.

20. Rossetti, S., et al., *Entrainment of breast (cancer) epithelial cells detects distinct circadian oscillation patterns for clock and hormone receptor genes.* Cell Cycle, 2012. **11**(2): p. 350-360.

21. Lala, D.S., D.A. Rice, and K.L. Parker, *Steroidogenic factor I, a key regulator of steroidogenic enzyme expression, is the mouse homolog of fushi tarazu-factor I.* Molecular endocrinology, 1992. **6**(8): p. 1249-1258.

22. Lin, L. and J. Achermann, *Steroidogenic factor-1 (SF-1, Ad4BP, NR5A1) and disorders of testis development.* Sexual Development, 2008. **2**(4-5): p. 200-209.

23. Degos, L., *All-trans retinoic acid (ATRA) therapeutical effect in acute promyelocytic leukemia.* Biomedicine & pharmacotherapy, 1992. **46**(5-7): p. 201-209.

24. Hansen, L.A., et al., *Retinoids in chemoprevention and differentiation therapy.* Carcinogenesis, 2000. **21**(7): p. 1271-1279.

25. Chronopoulos, A., et al., *ATRA mechanically reprograms pancreatic stellate cells to suppress matrix remodelling and inhibit cancer cell invasion.* Nature communications, 2016. **7**(1): p. 1-12.

26. Huang, T.Y., et al., *Combinational treatment of all-trans retinoic acid (ATRA) and bisdemethoxycurcumin (BDMC)-induced apoptosis in liver cancer Hep3B cells.* Journal of food biochemistry, 2020. **44**(2): p. e13122.

27. Lan, L., et al., *Inhibitory effects of retinoic acid on invasiveness of human thyroid carcinoma cell lines in vitro.* Journal of endocrinological investigation, 2009. **32**(9): p. 731-738.

28. Liu, H., et al., *PPARγ ligands and ATRA inhibit the invasion of human breast cancer cells in vitro.* Breast cancer research and treatment, 2003. **79**(1): p. 63-74.

29. Aboulafia, D.M., et al., *9-cis-retinoic acid capsules in the treatment of AIDS-related Kaposi sarcoma: results of a phase 2 multicenter clinical trial.* Archives of dermatology, 2003. **139**(2): p. 178-186.

30. Hofmann, W., et al., *Oral 9-cis retinoic acid (Alitretinoin) in the treatment of myelodysplastic syndromes: results from a pilot study.* Leukemia, 2000. **14**(9): p. 1583-1588.

31. Aul, C., V. Runde, and N. Gattermann, *All-trans retinoic acid in patients with myelodysplastic syndromes: results of a pilot study.* 1993.

32. Boehm, M.F., et al., *Synthesis and structure-activity relationships of novel retinoid X receptor-selective retinoids.* Journal of medicinal chemistry, 1994. **37**(18): p. 2930-2941.

33. Siegel, R.S., et al., *Primary cutaneous T-cell lymphoma: review and current concepts.* Journal of Clinical Oncology, 2000. **18**(15): p. 2908-2925.

34. Dawson, M., *Synthetic retinoids and their nuclear receptors.* Current Medicinal Chemistry-Anti-Cancer Agents, 2004. **4**(3): p. 199-230.

35. Dawson, M.I., et al., *Conformational effects on retinoid receptor selectivity. 2. Effects of retinoid bridging group on retinoid X receptor activity and selectivity.* Journal of medicinal chemistry, 1995. **38**(17): p. 3368-3383.

36. Lehmann, J.M., et al., *Retinoids selective for retinoid X receptor response pathways.* Science, 1992. **258**(5090): p. 1944-1946.

37. Cesario, R.M., et al., *Differentiation and growth inhibition mediated via the RXR: PPARγ heterodimer in colon cancer.* Cancer letters, 2006. **240**(2): p. 225-233.

38. Yen, W.-c., R.Y. Prudente, and W.W. Lamph, *Synergistic effect of a retinoid X receptor-selective ligand bexarotene (LGD1069, Targretin) and paclitaxel (Taxol) in mammary carcinoma.* Breast cancer research and treatment, 2004. **88**(2): p. 141-148.

39. Zhang, D., et al., *Testing novel pyrimidinyl rexinoids: a new paradigm for evaluating rexinoids for cancer prevention.* Cancer Prevention Research, 2019. **12**(4): p. 211-224.

40. Yen, W.-C., et al., *A Selective retinoid X receptor agonist bexarotene (targretin) prevents and overcomes acquired paclitaxel (Taxol) resistance in human non–small cell lung cancer.* Clinical cancer research, 2004. **10**(24): p. 8656-8664.

41. Dragnev, K.H., et al., *A proof-of-principle clinical trial of bexarotene in patients with non–small cell lung cancer.* Clinical Cancer Research, 2007. **13**(6): p. 1794-1800.

42. Lalloyer, F., et al., *Rexinoid bexarotene modulates triglyceride but not cholesterol metabolism via gene-specific permissivity of the RXR/LXR heterodimer in the liver.* Arteriosclerosis, thrombosis, and vascular biology, 2009. **29**(10): p. 1488-1495.

43. Jurutka, P.W., et al., *Modeling, Synthesis and Biological Evaluation of Potential Retinoid-X-Receptor (RXR) Selective Agonists: Analogs of 4-[1-(3, 5, 5, 8, 8-Pentamethyl-5, 6, 7, 8-tetrahyro-2-naphthyl) ethynyl] benzoic Acid (Bexarotene) and 6-(Ethyl (4-isobutoxy-3-isopropylphenyl) amino) nicotinic Acid (NEt-4IB).* International journal of molecular sciences, 2021. **22**(22): p. 12371.

44. Mangelsdorf, D.J., et al., *Nuclear receptor that identifies a novel retinoic acid response pathway.* Nature, 1990. **345**(6272): p. 224-229.

45. Kastner, P., et al., *Genetic analysis of RXRα developmental function: convergence of RXR and RAR signaling pathways in heart and eye morphogenesis.* Cell, 1994. **78**(6): p. 987-1003.

46. Kastner, P., et al., *Vitamin A deficiency and mutations of RXRalpha, RXRbeta and RARalpha lead to early differentiation of embryonic ventricular cardiomyocytes.* Development, 1997. **124**(23): p. 4749-4758.

47. Krezel, W., et al., *RXR gamma null mice are apparently normal and compound RXR alpha+/-/RXR beta-/-/RXR gamma-/-mutant mice are viable.* Proceedings of the National Academy of Sciences, 1996. **93**(17): p. 9010-9014.

48. Kersten, S., et al., *Retinoid X receptor alpha forms tetramers in solution.* Proceedings of the National Academy of Sciences, 1995. **92**(19): p. 8645-8649.

49. Kersten, S., et al., *Auto-silencing by the retinoid X receptor.* Journal of molecular biology, 1998. **284**(1): p. 21-32.

50. Kersten, S., L. Pan, and N. Noy, *On the role of ligand in retinoid signaling: positive cooperativity in the interactions of 9-cis retinoic acid with tetramers of the retinoid X receptor.* Biochemistry, 1995. **34**(43): p. 14263-14269.

51. Kersten, S., et al., *Role of ligand in retinoid signaling. 9-cis-retinoic acid modulates the oligomeric state of the retinoid X receptor.* Biochemistry, 1995. **34**(42): p. 13717-13721.

52. Gampe, R.T., et al., *Structural basis for autorepression of retinoid X receptor by tetramer formation and the AF-2 helix.* Genes & development, 2000. **14**(17): p. 2229-2241.

53. IJpenberg, A., et al., *In vivo activation of PPAR target genes by RXR homodimers.* The EMBO journal, 2004. **23**(10): p. 2083-2091.

54. Giguère, V., et al., *Functional domains of the human glucocorticoid receptor.* Cell, 1986. **46**(5): p. 645-652.

55. Bourguet, W., et al., *Crystal structure of the ligand-binding domain of the human nuclear receptor RXR-α.* Nature, 1995. **375**(6530): p. 377-382.

56. Uppenberg, J., et al., *Crystal structure of the ligand binding domain of the human nuclear receptor PPARγ.* Journal of Biological Chemistry, 1998. **273**(47): p. 31108-31112.

57. Szanto, A., et al., *Retinoid X receptors: X-ploring their (patho) physiological functions.* Cell Death & Differentiation, 2004. **11**(2): p. S126-S143.

58. Vivat-Hannah, V., et al., *Separation of retinoid X receptor homo-and heterodimerization functions.* Molecular and Cellular Biology, 2003. **23**(21): p. 7678-7688.

59. Heyman, R.A., et al., *9-cis retinoic acid is a high affinity ligand for the retinoid X receptor.* Cell, 1992. **68**(2): p. 397-406.

60. Levin, A.A., et al., *9-cis retinoic acid stereoisomer binds and activates the nuclear receptor RXRα.* Nature, 1992. **355**(6358): p. 359-361.

61. Costaridis, P., et al., *Endogenous retinoids in the zebrafish embryo and adult.* Developmental dynamics: an official publication of the American Association of Anatomists, 1996. **205**(1): p. 41-51.

62. Ulven, S.M., et al., *Quantitative axial profiles of retinoic acid in the embryonic mouse spinal cord: 9-cis retinoic acid only detected after all-trans-retinoic acid levels are super-elevated experimentally.* Developmental dynamics: an official publication of the American Association of Anatomists, 2001. **222**(3): p. 341-353.

63. Schmidt, C.K., A. Brouwer, and H. Nau, *Chromatographic analysis of endogenous retinoids in tissues and serum.* Analytical biochemistry, 2003. **315**(1): p. 36-48.

64. Belorusova, A.Y., et al., *Structural analysis identifies an escape route from the adverse lipogenic effects of liver X receptor ligands.* Communications biology, 2019. **2**(1): p. 1-13.

65. Grubbs, C.J., et al., *Efficacy of new retinoids in the prevention of mammary cancers and correlations with short-term biomarkers.* Carcinogenesis, 2006. **27**(6): p. 1232-1239.

66. Kolesar, J.M., et al., *A pilot, first-in-human, pharmacokinetic study of 9cUAB30 in healthy volunteers.* Cancer Prevention Research, 2010. **3**(12): p. 1565-1570.

67. Saladi, R.N. and A.N. Persaud, *The causes of skin cancer: a comprehensive review.* Drugs of Today, 2005. **41**(1): p. 37-54.

68. Fartasch, M., et al., *The relationship between occupational sun exposure and non-melanoma skin cancer: clinical basics, epidemiology, occupational disease evaluation, and prevention.* Deutsches Ärzteblatt International, 2012. **109**(43): p. 715.

69. Grossman, D. and D.C. Altieri, *Drug resistance in melanoma: mechanisms, apoptosis, and new potential therapeutic targets.* Cancer and Metastasis Reviews, 2001. **20**(1): p. 3-11.

70. Wong, C., R. Strange, and J. Lear, *Basal cell carcinoma.* Bmj, 2003. **327**(7418): p. 794-798.

71. Rudolph, R. and D.E. Zelac, *Squamous cell carcinoma of the skin.* Plastic and reconstructive surgery, 2004. **114**(6): p. 82e-94e.

72. Green, A., *Changing patterns in incidence of non-melanoma skin cancer.* Epithelial cell biology, 1992. **1**(1): p. 47-51.

73. Glass, A.G. and R.N. Hoover, *The emerging epidemic of melanoma and squamous cell skin cancer.* Jama, 1989. **262**(15): p. 2097-2100.

74. Madan, V., J.T. Lear, and R.-M. Szeimies, *Non-melanoma skin cancer.* The lancet, 2010. **375**(9715): p. 673-685.

75. Lucena, S.R., et al., *Combined treatments with photodynamic therapy for non-melanoma skin cancer.* International journal of molecular sciences, 2015. **16**(10): p. 25912-25933.

76. Miller, M.D. and G.N. Phillips, *Moving beyond static snapshots: Protein dynamics and the Protein Data Bank.* Journal of Biological Chemistry, 2021. **296**.

77. Karplus, M. and J. Kuriyan, *Molecular dynamics and protein function.* Proceedings of the National Academy of Sciences, 2005. **102**(19): p. 6679-6685.

78. SAKamenecka, B., *Partial agonists activate PPARgamma using a helix 12 independent mechanism.* Structure, 2007. **15**: p. 12581271.

79. Zheng, J., et al., *Chemical crosslinking mass spectrometry reveals the conformational landscape of the activation helix of PPARγ; a model for ligand-dependent antagonism.* Structure, 2018. **26**(11): p. 1431-1439. e6.

80. Hvidt, A. and K. Linderstrøm-Lang, *Exchange of hydrogen atoms in insulin with deuterium atoms in aqueous solutions.* Biochimica et biophysica acta, 1954. **14**(4): p. 574-575.

81. Englander, S., et al., *Hydrogen exchange: the modern legacy of Linderstrøm-Lang.* Protein science, 1997. **6**(5): p. 1101-1109.

82. Engen, J.R. and T.E. Wales, *Analytical aspects of hydrogen exchange mass spectrometry.* Annual review of analytical chemistry, 2015. **8**: p. 127-148.

83. Katta, V., B.T. Chait, and S. Carr, *Conformational changes in proteins probed by hydrogen-exchange electrospray-ionization mass spectrometry.* Rapid Communications in Mass Spectrometry, 1991. **5**(4): p. 214-217.

84. Masson, G.R., et al., *Recommendations for performing, interpreting and reporting hydrogen deuterium exchange mass spectrometry (HDX-MS) experiments.* Nature methods, 2019. **16**(7): p. 595-602.

85. Mayne, L., *Hydrogen exchange mass spectrometry*, in *Methods in enzymology*. 2016, Elsevier. p. 335-356.

86. Engen, J.R., *Analysis of protein conformation and dynamics by hydrogen/deuterium exchange MS*. 2009, ACS Publications.

87. Rosa, J.J. and F.M. Richards, *An experimental procedure for increasing the structural resolution of chemical hydrogen-exchange measurements on proteins: application to ribonuclease S peptide.* Journal of molecular biology, 1979. **133**(3): p. 399-416.

88. Molday, R., S. Englander, and R. Kallen, *Primary structure effects on peptide group hydrogen exchange.* Biochemistry, 1972. **11**(2): p. 150-158.

89. Bai, Y., et al., *Primary structure effects on peptide group hydrogen exchange.* Proteins: Structure, Function, and Bioinformatics, 1993. **17**(1): p. 75-86.

90. Sivaraman, T. and A.D. Robertson, *Kinetics of conformational fluctuations by EX1 hydrogen exchange in native proteins*, in *Protein Structure, Stability, and Folding*. 2001, Springer. p. 193-214.

91. Weis, D.D., et al., *Identification and characterization of EX1 kinetics in H/D exchange mass spectrometry by peak width analysis.* Journal of the American Society for Mass Spectrometry, 2006. **17**(11): p. 1498-1509.

92. Kirk, J., R.J. Mortishire-Smith, and M. Wrona, *A Novel Approach Using UPLC-Tof MS E and the UNIFI Scientific Information System to Facilitate Impurity Profiling of Pharmaceuticals.*

93. Desphande, A., et al., *Methyl-substituted conformationally constrained rexinoid agonists for the retinoid X receptors demonstrate improved efficacy for cancer therapy and prevention.* Bioorganic & medicinal chemistry, 2014. **22**(1): p. 178-185.

94. Boerma, L.J., et al., *Defining the communication between agonist and coactivator binding in the retinoid X receptor α ligand binding domain.* Journal of Biological Chemistry, 2014. **289**(2): p. 814-826.

95. Dasgupta, S., D.M. Lonard, and B.W. O'Malley, *Nuclear receptor coactivators: master regulators of human health and disease.* Annual review of medicine, 2014. **65**: p. 279-292.

96. Onate, S.A., et al., *Sequence and characterization of a coactivator for the steroid hormone receptor superfamily.* Science, 1995. **270**(5240): p. 1354-1357.

97. Xu, J., R.-C. Wu, and B.W. O'malley, *Normal and cancer-related functions of the p160 steroid receptor co-activator (SRC) family.* Nature Reviews Cancer, 2009. **9**(9): p. 615-630.

98. Beinsteiner, B., et al., *A structural signature motif enlightens the origin and diversification of nuclear receptors.* PLoS Genetics, 2021. **17**(4): p. e1009492.